

**I: Remote Spectroscopic Measurements of Atmospheric
HDO/H₂O and Column CO₂**

II: Interannual Variations of the Earth's Reflectance

Thesis by

Zhiming Kuang

In Partial Fulfillment of the Requirements for the Degree of

Doctor of Philosophy

CALIFORNIA INSTITUTE OF TECHNOLOGY

Pasadena, California

2003

Defended December 2, 2002

© 2003
Zhiming Kuang
All Rights Reserved

Dedicated to my parents and my wife

Acknowledgements

I came to Caltech six and a half years ago, with virtually no experience in research. From there to the completion of this thesis, so many people have helped in so many ways; a complete list would not be possible. I hope the following may express to some extent my gratitude to them.

First of all, I am indebted to my thesis advisor, Yuk Yung, who has been extraordinarily supportive and gave me a great deal of freedom to pursue my own research interests. With his support, along with those from Andy Ingersoll, Paul Wennberg, Dave Stevenson, and Bruce Murray, I also had the opportunity to attend the GFD summer school at Wood Hole in 2000 and the NCAR summer colloquium in 2001. Both were very beneficial.

I thank Bruce Murray and Dave Stevenson for serving as my academic advisors through the years. Dave also served as my research advisor for my first two years, and introduced me to my first research project the very first day I stepped into South Mudd. I am grateful to Peter Goldreich, Paul Wennberg, and Dave Stevenson for encouragement. Paul Wennberg participated in the work presented in this thesis, and provided much advice.

I was privileged to have worked with many scientists at JPL: Geoffrey Toon, Ross Salawitch, Dave Crisp, Jack Margolis, among many others. I am especially grateful to Geoffrey Toon, who is an invaluable resource for the analyses of FTIR spectra.

I must thank Mike Black for resolving my numerous computer problems. Shawn Ewald has also been a great help.

The support from the staff members, Key Campbell, Irma Black, Susan Leising, Tammie Henderson, Donna Sackett, Leticia Calderon, Nora Oshima, Loreta Young, is also gratefully acknowledged.

John Eiler gave me the opportunity to work in his lab. Nami Kitchen was a great help in the lab. While the experiment is not yet successful, it has been a great experience.

The senior graduate students/postdocs were a great help during my junior graduate years. James Cho, Yibo Jiang, Chunhua Qi, Frank Mills, Adam Showman, Sarah Stewart, Ashwin Vasavada, Albert Yen, Hui Zhang, thank you. Liz Moyer provided much advice for the work presented in Chapter 1. Mimi Gerstell commented on almost all my papers. I also thank my fellow graduate students, Lori Fenton, Ulyana Dyudina, my office mates, Shane Byrne, Anthony Lee, Dave Camp, Ben Weiss, Tanja Bosak, Damian Kraemer, and other members of the climate group, Xianglei Huang, David Noone for many enjoyable moments. I thank Dave Camp for many conversations about math and other, more practical, issues.

It is not possible to express my gratitude to my wife, Huiqun, for all the love and joy that she brings to my life. I must also thank my parents, in particular my mom, who devoted most of her life raising and educating her children. It is to them this thesis is dedicated to.

Table of Contents

Acknowledgements	iv
Overview	x
Part I Remote Spectroscopic Measurements of Atmospheric HDO/H ₂ O and Column CO ₂	1
Chapter 1: Measured HDO/H ₂ O Ratio across the Tropical Tropopause	2
1.1 Abstract	3
1.2 Introduction	4
1.3 Data and Spectral Retrieval	9
1.4 Results	12
1.5 Conclusions	19
1.6 Acknowledgements	19
1.7 Appendix	21
1.8 Reference	29
Chapter 2: Space-Borne Measurements of Atmospheric CO ₂ by High-Resolution NIR Spectrometry of Reflected Sunlight	35
2.1 Abstract	36
2.2 Introduction	37
2.3 Measurement Strategy	38
2.4 Retrieval Approach	41
2.5 Achievable Precisions	44
2.6 Systematic Errors and Potential Biases	48
2.7 Discussion	50
2.8 Summary and Conclusions	51
2.9 Acknowledgements	52
2.10 References	53
Part II Interannual Variations of the Earth's Reflectance	55
Chapter 3: Interannual Reflectance Variations of the Earth: An Overview	56
3.1 Introduction	57
3.2 Data	58
3.3 Globally Averaged Reflectance	62
3.4 Global Distributions of Interannual Reflectance Variability	64
3.5 Summary	67

3.6 Appendix	68
3.7 References	73
Chapter 4: Observed Effects of Interannual Summertime Sea Ice Variations on the Polar Reflectance	77
4.1 Abstract	78
4.2 Introduction	79
4.3 Data and Methods	80
4.4 Results	84
4.5 Discussion	88
4.6 Conclusion	91
4.7 Acknowledgements	92
4.8 References	93
Chapter 5: Interannual Reflectance Variations over the North Pacific and North Atlantic	95
5.1 Abstract	96
5.2 Introduction	97
5.3 Cloud Processes over the Midlatitude Oceans	100
5.4 Seasonal Reflectance Variations	107
5.5 Data and Methods	110
5.6 Results	113
a. DJF North Pacific	113
b. DJF N. Atlantic	120
c. JJA N. Atlantic	124
d. JJA N. Pacific	126
e. Relation between Summertime Reflectance and SST	128
5.7 Discussion	133
5.8 Concluding Remarks	137
5.9 Acknowledgements	139
5.10 References	140

Table of Figures

Figure 1.1 The locations of 11 tropical ATMOS atlas-3 sunset occultations (white symbols) that extended below the tropopause.....	10
Figure 1.2 The δD profiles from the 11 tropical occultations.....	13
Figure 1.3 The derived δD profiles from ATLAS-3 occultations #94 and #96.....	16
Figure 1.4 A representative spectral fit of HDO for filter 9 spectra.....	22
Figure 1.5 The same as Figure 1.4, except for a $H_2^{16}O$ window.....	23
Figure 1.6 The same as Figure 1.4 except for a filter 3 spectrum.....	23
Figure 1.7 The same as Figure 1.6 except for $H_2^{16}O$	24
Figure 1.8 The same as Figure 1.4 except for a filter 4 spectrum.....	24
Figure 1.9 The ratio between the HDO slant columns derived using filter 9 windows and filter 3 windows for the tangent altitude range of 11-25 km.....	28
Figure 1.10 Variations in the derived δD due to a 5% increase in the pressure broadening half width and a 3K increase in the tangent temperature.....	28
Figure 2.1 Simulated atmospheric transmission of the 0.76- μm O_2 A-band (a), 1.58- μm (b) and 2.06- μm (c) CO_2 bands.....	38
Figure 2.2 Band-averaged weighting function for CO_2 variations.....	44
Figure 2.3 Achievable X_{CO_2} precisions calculated from linear covariance analysis.....	45
Figure 2.4 Precisions of X_{CO_2} retrievals as a function of the number of soundings averaged.....	47
Figure 2.5 Deficits in X_{CO_2} due to a constant zero offset error.....	49
Figure 3.1 Climatological mean distribution of the TOMS reflectance.....	61
Figure 3.2 Interannual variations of the area-weighted averages of the TOMS reflectance.....	63
Figure 3.3 Interannual reflectance variability for DJF (a) and JJA (b).....	66
Figure 3.4 Comparison between the mean seasonal cycles in the TOMS reflectance and the ERBE_SC visible albedo over a N. Pacific (a) and a S. Pacific site (b).....	69
Figure 3.5 Correlation (a) and regress (b) coefficients between monthly ERBE visible albedo and TOMS UV reflectance anomalies.....	70
Figure 3.6 Comparison between monthly ERBE visible albedo and TOMS UV reflectance over a tropical (a) and a subtropical (b) site.....	72
Figure 4.1 The Arctic (a) and Antarctic (b) icy areas.....	83
Figure 4.2 Summertime interannual variations of the UV LER and the sea ice concentration for the Arctic (a) and the Antarctic (b) icy areas.....	86

Figure 4.3 Differences in the summertime UV LER changes and sea ice concentration changes between the polar icy regions where the interannual sea ice variability is greater than 7% and the icy regions where the variability is less than 7%.....	87
Figure 5.1 Visible (upper) and infrared (lower) images taken by the GEOS-10 geostationary meteorological satellite on November 2, 2001.....	101
Figure 5.2 The same as Figure 5.1 but for July 17, 2001.....	102
Figure 5.3 The TOMS daily reflectance maps taken at approximately the same time as Figure 5.1 (upper panel), and Figure 5.2 (lower panel).....	105
Figure 5.4 Climatological mean reflectance for January (a) and July (c). Contributions from grids with reflectance greater than 75RU are shown in (b) and (d) for January and July, respectively.....	106
Figure 5.5 Occurrence frequencies for different reflectance values over the N. Pacific 160°E-140°W, 35°N-60°N (a), N. Atlantic 80°W-10°W, 35°N-60°N (b) and the Southern Oceans 180°W-180°E, 65°S-40°S (c) in January (solid) and July (dashed).....	109
Figure 5.6 The leading EOF patterns of the following fields for the DJF N. Pacific.....	114
Figure 5.7 Leading EOF/SVD patterns over the DJF N. Atlantic.....	122
Figure 5.8 Top to bottom (a-d): the same as Figure 5.7a, b, c, f, except for JJA N. Atlantic.....	125
Figure 5.9 Leading EOF/SVD patterns over the JJA N. Pacific.....	127
Figure 5.10 The leading SVD patterns between reflectance and SST over the JJA N. Pacific (a) and N. Atlantic (b).....	131
Figure 5.11 The SVD patterns of surface heat flux when it is paired with the reflectance for JJA N. Pacific (a) and JJA N. Atlantic (b).....	132
Figure 5.12 The interannual local correlation coefficients between reflectance and stability anomalies for DJF (a), MAM (b), JJA (c) and SON (d), over the N. Pacific.....	134
Figure 5.13 The averaged TOMS reflectance for stability bins over the JJA N. Pacific (160°E-140°W, 35°N-60°N).....	136

Overview

The theme of this thesis is to apply remote sensing data on problems concerning the climate system. It is grouped into two parts. Part I (Chapters 1, 2) is devoted to spectroscopic measurements of HDO, H₂O, and column CO₂, and Part II (Chapters 3-5) is devoted to variations in the Earth's reflectance.

In Chapter 1, we derive the first simultaneous measurements of HDO and H₂O in the tropical upper troposphere and lower stratosphere. This is made possible by extending the retrievals of the Atlas-3 Atmospheric Trace Molecule Spectroscopy (ATMOS) data deeper into the troposphere. The derived HDO/H₂O ratio demonstrates that convection has a major influence on the moisture budget and the dehydration processes in this region.

The objective of Chapter 2 is to determine the precision to which column averaged CO₂ volume mixing ratio (VMR) can be measured by near-infrared (NIR) spectrometry of reflected sunlight. The key idea in this study is the simultaneous use of the CO₂ (1.58- μ m and 2.06- μ m) and O₂ (0.76- μ m) bands. This approach allows small changes in the spectrum arising from variations of column CO₂ VMR to be distinguished from those arising from variations of other atmospheric/surface parameters. Using prototype retrieval simulations based on a practical satellite instrument design, we show that the 3-band, high-resolution, spectrometric approach using NIR reflected sunlight has the potential for highly accurate column CO₂ VMR measurements.

In Part II, we examine the interannual variations in the earth's reflectance. The innovative part of this study is the use of the Nimbus-7 TOMS reflectance measurements. The TOMS reflectance dataset is a byproduct from an instrument that was designed to measure ozone, and has not been widely used by the climate change community. We recognize that its excellent calibration and its relatively long temporal coverage (14 years) make it a unique dataset suited for the study of interannual variations in the earth's reflectance.

Chapter 3 introduces the Nimbus-7 TOMS reflectance measurements and provides an overview on the interannual variability of the Earth's reflectance. Variations in the globally averaged reflectance are also used to examine a postulated cosmic ray – cloud – climate connection.

In Chapter 4, we relate interannual reflectance variations over the summertime polar icy areas to variations in the microwave-derived sea ice concentration. The results provide independent confirmation on sea ice variations observed by microwave instruments, and quantify the role of clouds in shielding the reflectance effect of sea ice variations. An interesting hemispheric asymmetry is found: a 1% change in the sea ice concentration is related to a significantly larger reflectance change in the Antarctic than in the Arctic icy areas.

Chapter 5 is devoted to interannual reflectance variations over the northern midlatitude oceans. We find that interannual reflectance variations in these regions are, to a large extent, related to variations in the large-scale circulation, mostly through variations in the

storms tracks. The findings in this chapter suggest that the response of clouds to climate change may be better viewed from a large-scale circulation perspective, other than a purely thermodynamic one (such as in the cloud – temperature relations), a stand many previous investigations have taken.

**Part I: Remote Spectroscopic Measurements
of Atmospheric HDO/H₂O and Column CO₂**

Chapter 1: Measured HDO/H₂O Ratio across the Tropical Tropopause

Zhiming Kuang¹, Geoffrey Toon², Paul Wennberg¹, Yuk Yung¹

¹ Division of Geological and Planetary Sciences,
California Institute of Technology.

² Jet Propulsion Laboratory, California Institute
of Technology

1.1 Abstract

We report the first simultaneous measurements of HDO and H₂O in the tropical upper troposphere and lower stratosphere. The HDO/H₂O ratio is remarkably constant in this region despite a factor of 5 variation in the water vapor mixing ratio. This observation unambiguously demonstrates that convection has a major influence on the moisture budget and the dehydration processes in this region.

1.2 Introduction

A recent assessment of stratospheric water observations obtained over the last 50 years concludes that there has been an approximate doubling in stratospheric humidity [Rosenlof *et al.*, 2001; SPARC, 2000]. Such a change is quite disturbing, because stratospheric water plays important roles in the Earth's climate through its influences on radiation and ozone chemistry [Forster and Shine, 1999; Kirk-Davidoff *et al.*, 1999]. Enhancement of stratospheric water impacts stratospheric ozone and may delay the recovery of the ozone column following its decades-long deterioration caused by halogen free radical catalysis [Kirk-Davidoff *et al.*, 1999; Shindell, 2001]. It may also significantly contribute to the greenhouse warming [Hartmann *et al.*, 2000; Shindell, 2001]. Because of these climatic impacts, it is important to understand how stratospheric water content is regulated and how it would respond to climate change. For this purpose, we shall distinguish the part of the stratosphere that is above 380 K isentropic surface, sometimes known as the “overworld,” from the part below, referred to as the “lowermost stratosphere” [Hoskins, 1991], as they are governed by distinct dynamical processes. In this work, we are mostly concerned with the “overworld” stratosphere, and the terms “stratosphere” and “overworld stratosphere” will be used interchangeably.

The amount (or volume mixing ratio — VMR) of water vapor in the overworld stratosphere is determined both by the water VMR of air entering the stratosphere from the troposphere and by *in situ* production from oxidation of methane [Hurst *et al.*, 1999]. While the *in situ* production of water by methane oxidation is relatively well understood

[*Hurst et al.*, 1999], important uncertainties exist in our knowledge of the processes that regulate the humidity of the air entering the stratosphere from the troposphere.

Following Brewer's classic work [*Brewer*, 1949], it is generally accepted that tropospheric air enters "overworld" mostly through the tropical tropopause. This Brewer-Dobson circulation has been confirmed by stratospheric tracer measurements, and is understood in terms of a "wave-driven" circulation [*Holton et al.*, 1995], although tropical diabatic heating may also play a role in driving the circulation [*Plumb and Eluszkiewicz*, 1999]. While the global mass transport may be estimated by calculating the extratropical wave-induced forcing [*Rosenlof and Holton*, 1993], the transport of water across the tropical tropopause is complicated because of water's phase transition, and requires considering small-scale processes.

The relative importance of large-scale circulation and small-scale processes in determining the stratospheric water content has been actively debated for decades but remains unclear [*Danielsen*, 1982; *Holton and Gettelman*, 2001; *Newell and Gouldstewart*, 1981; *Sherwood and Dessler*, 2001]. During this period, it is increasingly recognized that the tropical tropopause is not a sharp boundary [*Atticks and Robinson*, 1983; *Highwood and Hoskins*, 1998; *Newton and Persson*, 1962]. Observations of ozone, lapse rate, and convective mass flux profiles show a layer extending roughly from 14 to 19 km that marks the transition from the troposphere to the stratosphere [*Folkins et al.*, 1999], sometimes dubbed the tropical tropopause layer (TTL). Tropical troposphere-stratosphere water transport is, therefore, more appropriately examined in the context of the TTL, instead of a discrete tropopause boundary.

The long-standing debate is mainly on the relative importance of the two processes that desiccate the stratosphere — here labeled “gradual dehydration” and “convective dehydration.” Above ~13–14 km in the tropics (base of the TTL), the clear sky radiative heating is positive. Diabatic heating therefore causes air to ascend “gradually” towards the stratosphere. If at some point, this air becomes sufficiently supersaturated, ice crystals will form, grow and fall, leading to dehydration. In this “gradual dehydration” process, the humidity of the air entering the stratosphere is controlled by the coldest temperature, or more precisely the lowest saturation water VMR, that it has experienced, often at or near the tropopause. The cold episodes can be induced by, for example, horizontal advection through a cold trap [*Holton and Gettelman, 2001*] or wave perturbations [*Potter and Holton, 1995*]. In contrast, in “convective dehydration,” air detrained from deep convection in the TTL is already dehydrated to stratospheric abundances, and experiences little further freeze-drying during its subsequent gradual ascent towards the stratosphere [*Sherwood and Dessler, 2001*]. Deep convection here refers to convection that detrains above the base of the TTL. The moisture in the detrained air may include contributions from lofted cloud ice that later evaporates. The term “freeze-drying” refers to the process of condensation and precipitation of ice particles. It is important to distinguish between “gradual dehydration” and “convective dehydration” because each is likely to have changed differently over the last several decades, and is likely to change differently in the future as well. If gradual dehydration dominates, we should look to change in the temperature of the cold point as the primary forcing of stratospheric entry humidity. On the other hand, if convective processes

control stratospheric entry humidity, we should look to changes in convection and cloud microphysics.

The isotopic composition of water can be a useful tracer for studying the troposphere-stratosphere exchange of water [Moyer *et al.*, 1996]. The minor water isotopic species, such as HDO and H₂¹⁸O, have lower vapor pressures than H₂¹⁶O. As vapor condenses out of an air parcel, these minor isotopic species are preferentially removed and become progressively depleted in the residual vapor. The equilibrium fractionation factor is defined as $\alpha=R_{\text{vapor}}/R_{\text{condensate}}$, where R is the isotopic ratio (for instance [HDO]/[H₂¹⁶O]). We have used [X] for the VMR of gas X. The isotope ratios are also often expressed as deviations from those of the standard mean ocean water (SMOW), and are reported in the so-called δ notation: for example, the [HDO]/[H₂O] ratio of a sample is often expressed as

$$\delta D(\text{‰})=1000 \times \left[\frac{([HDO]/[H_2O])_{\text{sample}}}{([HDO]/[H_2O])_{\text{SMOW}}} - 1 \right] \quad (1.1)$$

The lowered vapor pressure of HDO is related to its larger moment of inertia. The equilibrium fractionation of H₂¹⁸O, on the other hand, is due to its larger molecular weight. Because the moment of inertia has a larger effect on the saturation vapor pressure than the molecular weight, the equilibrium fractionation factor of HDO is about 8 times that of H₂¹⁸O. In this work, we will focus on the fractionation of HDO from ice-vapor transition. The equilibrium fractionation factor for ice-vapor transition (α_1) is given by

$$\ln(\alpha_1)=16288/T^2-0.0934 \quad (1.2)$$

where T is expressed in Kelvin [Merlivat and Nief, 1967]. Under disequilibrium conditions, the slightly lower diffusivity of HDO reduces the fractionation factor to $\alpha = \alpha_1 S / (\alpha_1 (S-1) \beta + 1)$, where S is the supersaturation with respect to ice, and $\beta = 1.0251$ is the ratio of the diffusion coefficients between H_2O and HDO [Jouzel and Merlivat, 1984]. These phase transition related fractionations form the basis for inferring the condensation and evaporation history of the moisture from measurements of its isotopic composition.

Based on the measured isotopic composition of stratospheric water, an HDO abundance of $\delta\text{D} = \sim -670\text{‰}$ was inferred for the vapor that enters the stratosphere [Johnson *et al.*, 2001b; Moyer *et al.*, 1996]. In contrast, simple models, such as the Rayleigh distillation model, predict a $\delta\text{D} < -900\text{‰}$ at the tropopause [Keith, 2000; Moyer *et al.*, 1996]. The standard Rayleigh distillation model assumes that the condensates formed are in equilibrium with the vapor and are removed as soon as they form. The assumption of equilibration can be removed by replacing α_1 by α , which includes the kinetic fractionation effects associated with non-equilibration (Eq. 1.2). This model has been argued to be suitable for predicting the isotopic composition during gradual dehydration and in the protected core of convection [Keith, 2000]. Evaporation of lofted cloud ice was suggested in order to resolve this discrepancy between the observed δD and the model prediction [Johnson *et al.*, 2001a; Keith, 2000].

These stratospheric isotopic measurements, however, carry no information on the altitude at which ice lofting and evaporation occur. Convection could loft ice particles above the tropopause where they would evaporate, adding HDO-enriched moisture. On the other

hand, it is equally plausible that cloud lofting and evaporation occur well below the tropopause to provide a source of HDO-enriched moisture, which is then subject to further condensation and fractionation during the subsequent gradual ascent into the stratosphere. The stratospheric isotopic measurements therefore provide little constraint for discriminating between the two proposed dehydration scenarios [Keith, 2000; Moyer *et al.*, 1996]. Observations throughout the tropical tropopause region are needed.

In this work, we shall present measured HDO/H₂O ratio profiles in the TTL and discuss the implications to the water transport in this region.

1.3 Data and Spectral Retrieval

We derive HDO/H₂O profiles across the tropical tropopause from high spectral resolution ($\sim 0.01 \text{ cm}^{-1}$), infrared solar absorption spectra acquired by the Atmospheric Trace Molecule Spectroscopy (ATMOS) Fourier Transform Infra-Red (FTIR) spectrometer during the ATLAS-3 space shuttle mission in 1994 [Gunson *et al.*, 1996]. We shall present data from 11 tropical solar occultations taken between 5°N and 20°N from Nov. 12 to Nov. 14. Figure 1.1 shows the locations of these occultations (white symbols) together with the minimum 11- μm brightness temperature obtained by geostationary satellites. The tropical occultations that we chose in general reside in or near the inter-tropical convergence zone (ITCZ) region and are distributed over all longitudes. Since no ATMOS measurements were possible when the sun was blocked by optically thick clouds, our measurements are generally in the regions outside of deep convection. In

addition, our observations are limited in temporal coverage. More data are needed to examine possible seasonal behavior and interannual variability.

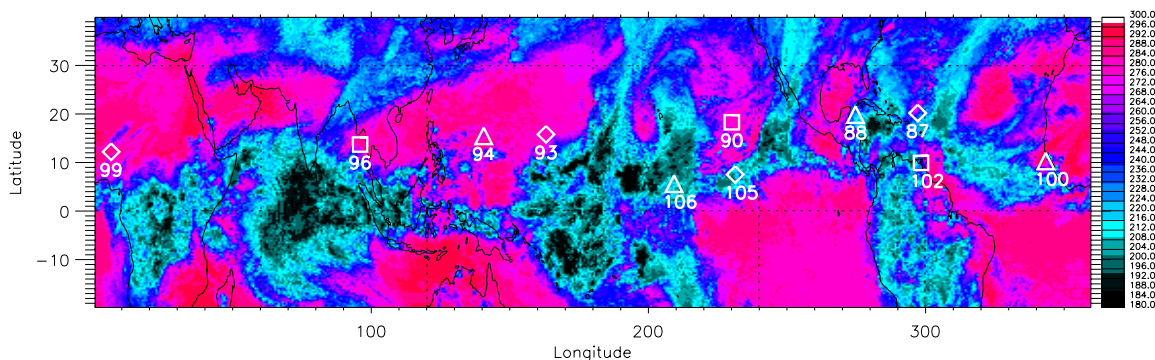


Figure 1.1 The locations of 11 tropical ATMOS altis-3 sunset occultations (white symbols) that extended below the tropopause. They were taken during Nov. 12-14, 1994. We also plot the minimum 11- μm brightness temperature over this period. The numbers refer to the occultation number in the ATMOS database. The minimum 11- μm brightness temperature was derived from 3-hourly geostationary satellite images averaged to a $0.3^\circ \times 0.7^\circ$ resolution. Deep convection is marked by the low brightness temperatures. The tropical occultations that we chose in general reside in or near the inter-tropical convergence zone (ITCZ) region and are distributed over all longitudes. Tracers such as CO in these occultations show tropospheric concentrations ($> \sim 80$ ppbv) up to near tropopause ($\sim 16.5\text{km}$) altitudes and quickly decrease to a stratospheric value (< 20 ppbv). In contrast, the CO concentrations in the subtropical occultations start to decrease well below the tropopause. Each occultation used one of the following three optical band pass filters: filter 3 (Δ), $1580\text{-}3340\text{ cm}^{-1}$, filter 4 (\diamond), $3150\text{-}4800\text{ cm}^{-1}$, and filter 9 (\square), $600\text{-}2450\text{ cm}^{-1}$.

The retrieval program that we use is the GFIT package provided by Geoffrey Toon at the Jet Propulsion Laboratory (JPL). The molecular parameters are taken from the ATMOS line list, which is an update of the High Resolution Transmission Molecular Absorption Database (HITRAN) [Brown *et al.*, 1996]. This program has been used extensively in the retrieval of spectra acquired by the JPL Mark IV FTIR [Sen *et al.*, 1996], an instrument similar to the ATMOS instrument.

The spectra used here are the same as in *Moyer et al.* [1996]. The analysis, however, has been improved in two ways. First, recent laboratory measurements have provided better spectroscopic parameters of H₂O and HDO [*Toth*, 1998; *Toth*, 1999a; *Toth*, 1999b; *Toth*, 2000; *Toth et al.*, 1998]. Second, the spectral retrieval has been extended deeper into the troposphere. In the previous analysis, narrow spectral intervals, mostly a fraction of a wavenumber (cm⁻¹) wide, were used to retrieve the abundance of HDO and H₂O [*Irion et al.*, 1996]. In contrast, in our analysis, wide windows (often tens of wavenumbers wide) are used. Given the much greater overlapping between gas absorption lines in the tropospheric spectra, the wide window approach is more suitable for tropospheric retrievals, and allows spectral parameters such as the continuum level and its tilt, to be better determined. As each occultation used one of the following three optical band pass filters: filter 3 (Δ), 1580-3340 cm⁻¹, filter 4 (\diamond), 3150-4800 cm⁻¹, and filter 9 (\square), 600-2450 cm⁻¹, appropriate spectral windows have been identified for each filter in order to retrieve the HDO and H₂O abundance. It is worth noting that in the previous analysis [*Irion et al.*, 1996], spectra acquired with filter 3 and filter 4 were not used. However, within the spectral range of filter 3, we have identified an excellent spectral window (around 2600 – 2800 cm⁻¹) for HDO. Usable windows for HDO retrievals have also been identified for filter 4 spectra. The consistency among the three filters is examined using spectra obtained from the Mark IV balloon flights [*Toon et al.*, 1999], which covered the spectral range of 650-5650 cm⁻¹. The results show that the filter 9 windows consistently give a HDO mixing ratio ~12% higher than the other two filters. After this bias is corrected, the three filters agree within the estimated errors. More detailed descriptions of

the spectral windows and the consistency among the filters are presented in the Appendix.

1.4 Results

The HDO/H₂O ratios, expressed as δD , show little further fractionation above ~ 12 km (Figure 1.2a). For the altitude range 11-19km, there is little systematic change in δD despite a fivefold decrease in the water mixing ratio [H₂O] (Figure 1.2b).

The HDO and H₂O abundances that we report are for the slant columns along the limb path as measured by the instrument, not VMR profiles retrieved from these slant columns. In this way, errors associated with this extra step of retrieval are avoided.

Effects due to errors in the tangent pressure (2%), the tangent temperature (3K), and the zero level offset (1%) have been folded into the error bars. The effect of methane oxidation has been removed [Irion *et al.*, 1996]. Unlike inferring the entry composition from the stratospheric measurements, our results are not sensitive to errors in this correction, as the effect of methane oxidation is small in the TTL.

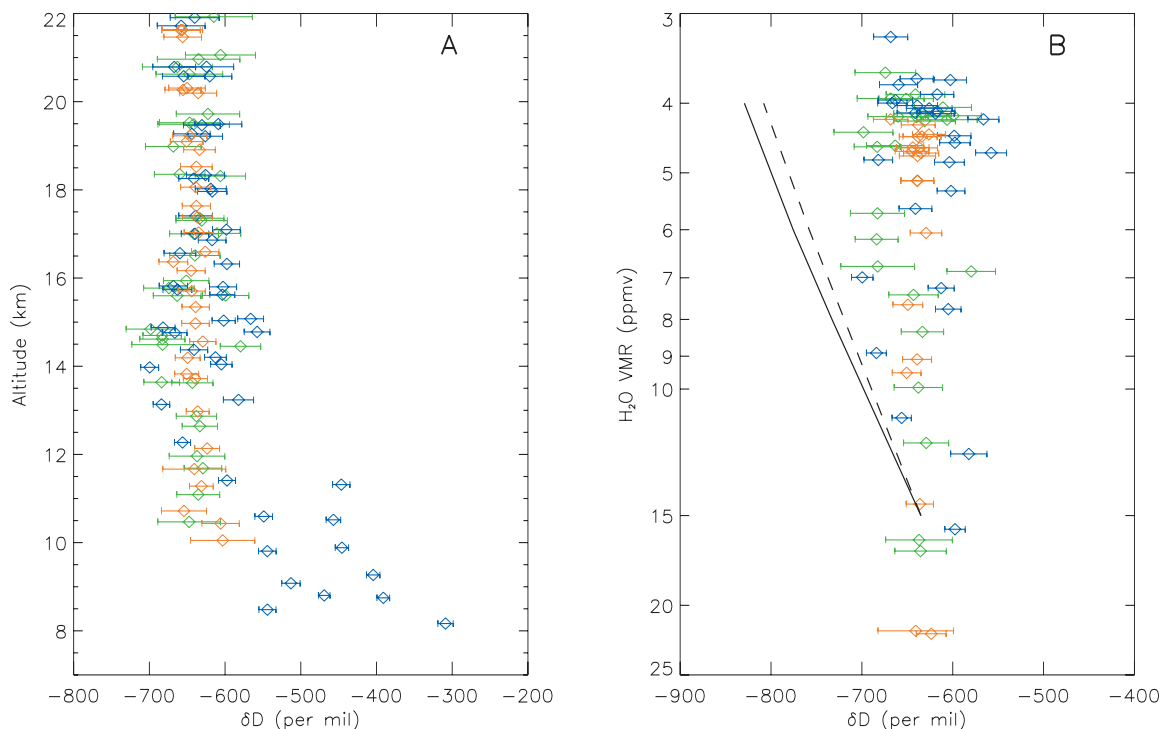


Figure 1.2 A) The δD profiles from the 11 tropical occultations. B) δD is plotted against the water mixing ratio [H_2O] for the altitude range of 11-19 km. The different filters are represented by different colors: f3, blue, f4, green, and f9, red. The effect of methane oxidation has been removed [Irion *et al.*, 1996]. The δD vs. [H_2O] relationship predicted by the Rayleigh distillation model, appropriate for the “gradual dehydration,” is over-plotted (solid). The fractionation factors are extrapolations from the data by Merlivat and Nief [1967]. The kinetic isotopic fractionation effect from a 10% supersaturation was included in calculating the dashed curve. The effect of the finite resolution of the ATMOS measurements has been included in both curves. The expected $\sim 200\%$ additional fractionation from the “gradual dehydration” process is completely absent in the data. This result thus shows “gradual dehydration” cannot be mainly responsible for the dehydration in the TTL, and that convective influence on the moisture must extend well above ~ 13 -14km.

The constancy of the observed δD unambiguously demonstrates the major influence of convection on the moisture budget in the TTL. Because most convection does not extend above ~ 14 km [Folkins *et al.*, 1999; Highwood and Hoskins, 1998], it is commonly assumed that convection does not have major effects on the characteristics of the bulk of the TTL [Holton and Gettelman, 2001]. If this were indeed the case, freeze-drying during the gradual ascent would have to be mainly responsible for the decrease of $[H_2O]$ in this layer. During the gradual ascent, the air is in general stably stratified, and the time for ice particles to precipitate is short compared to the advective cooling timescale. Under these conditions, the simple Rayleigh distillation model can be used to describe the evolution of the isotopic composition of the moisture. This has been demonstrated in the lower and middle troposphere when stably stratified conditions prevail [Gedzelman, 1988]. In Figure 1.2b, we show the δD vs. $[H_2O]$ relationship predicted by the Rayleigh model with a starting composition of $\delta D = -635\text{‰}$ and $[H_2O] = 15$ ppmv, appropriate for the base of the TTL (solid curve). The predicted additional 200‰ depletion in δD as $[H_2O]$ decreases from 15 ppmv to 4 ppmv is completely absent in the observations. Possible supersaturation during the gradual ascent [Jensen *et al.*, 2001; Jensen *et al.*, 1996] may reduce the fractionation, however, is insufficient to explain the difference. For instance, a 10% supersaturation reduces the fractionation by only $\sim 20\text{‰}$ (dashed line). We therefore conclude that the gradual freeze-drying scenario cannot be mainly responsible for the dehydration in the TTL, and that convective influence on the moisture must extend well above ~ 13 -14 km. This result is consistent with a recent study on the O_3 and CO distributions in the TTL [Dessler, 2002].

There is a potential uncertainty regarding the interpretation of the isotopic data. The fractionation factors between the vapor and solid phases for the HDO-H₂O system have been measured only between 0 and -40°C. Within this temperature range, the fractionation factor increases with a decreasing temperature, as described by Equation 1.2 [Merlivat and Nief, 1967]. It remains an assumption that this result can be extrapolated to the temperature range relevant to the TTL. This assumption is supported by recent laboratory measurements of desorption rates of H₂O ice in the temperature range of 175 K to 190 K [J. A. Smith, personal communications].

Evaporation of lofted cloud ice that is enriched in HDO appears to have contributed to the uniformity of the isotopic composition in the TTL. The ice-to-vapor ratio can exceed 100 at the top of convective towers [Knollenberg *et al.*, 1993]. Therefore, only a small fraction of this ice needs to remain in the air and later evaporate to make a significant contribution to the total moisture. Isotopic evidence of ice lofting and evaporation has been documented near the midlatitude tropopause [Smith, 1992], and it is likely that the same process operates in the tropics as well. In fact, simple models predict that the evaporation of lofted cloud ice would cause δD to increase with altitude, as contributions from evaporation of lofted ice become increasingly more important in the total moisture [Keith, 2000]. Interestingly, some of our profiles do exhibit such a reversal (Figure 1.3, blue).

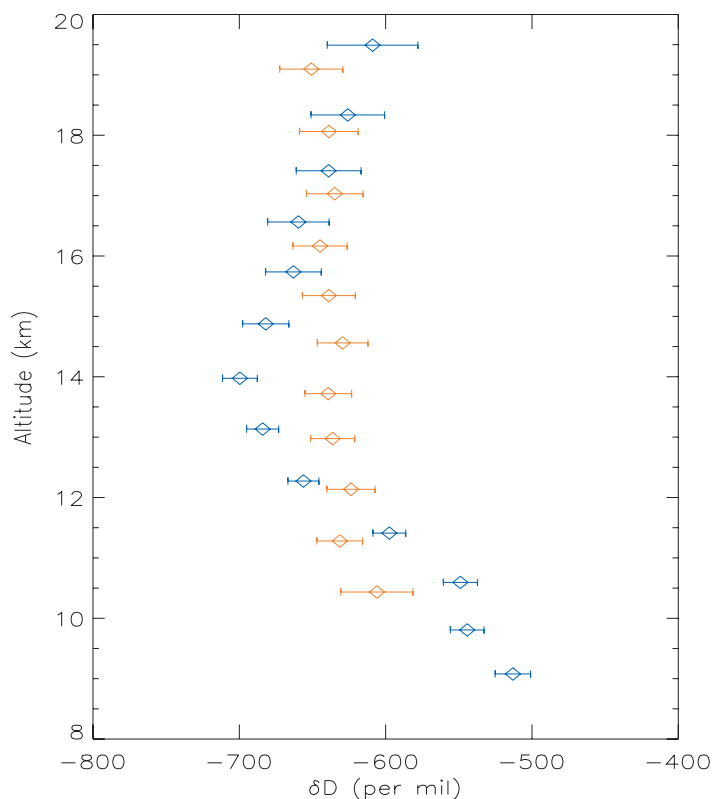


Figure 1.3 The derived δD profiles from ATLAS-3 occultations #94 (blue) and #96 (red). The reversal of the δD gradient seen in #94 is likely a consequence of ice lofting and evaporation, while the constancy of δD in #96 suggests that dehydration is accomplished by mixing with dry air instead of freeze-drying.

The “convective dehydration” mechanism proposed by Sherwood and Dessler [2001] may also help to explain the lack of δD gradient in the TTL. In their model, for the region outside of deep convection, less energetic convection supplies moisture to the base of the TTL. As the air gradually ascends by radiative heating, its $[H_2O]$ decreases since the moist air is progressively diluted through mixing with much drier air detrained from the more energetic convective events that penetrate into the TTL. In this scenario, the decrease in $[H_2O]$ in the upper troposphere is not directly related to condensation, thus does not involve further isotopic fractionation. As an extreme example, consider the case

when the air detrained from the more energetic convections has a negligible amount of moisture compared to the air that is gradually rising from the base of the TTL. In this case, the δD would be constant all the way across the TTL. The constant δD shown in Figure 1.3 (red) is perhaps a consequence of this “mix-drying” mechanism. The air detrained from the more energetic convective events, of course, also carries a finite amount of moisture. However, since evaporated cloud ice constitutes a significant portion of this moisture, its isotopic composition would not be significantly different from that of the moisture that gradually ascends from the base of the TTL. Evaporation of lofted ice and the “mix-drying” mechanism can therefore combine to explain the lack of vertical δD gradient in the TTL. It is interesting to note that a recent modeling effort that includes cloud lofting/evaporation and this “mix-drying” mechanism was able to produce a δD vs. $[H_2O]$ relationship similar to the observations that we have presented here [S. Sherwood, personal communication]. The TTL water isotopic data thus support “convective dehydration” as the control of stratospheric humidity [Sherwood and Dessler, 2001], and question the necessity of additional “gradual dehydration”.

The averaged δD is -640‰ between 13 km and the tropopause (~16.5 km) with a standard deviation of 39‰ and -631‰ between the tropopause and 19 km, with a standard deviation of 15‰. There are 36 samples between 13 km and the tropopause and 24 samples between the tropopause and 19 km. The samples are weighted by their individual uncertainties when we calculate the mean and the standard deviation. The estimated measurement uncertainty of individual samples in each region is about 22‰ and 25‰, respectively. The scatter in the upper troposphere thus exceeds what one

expects from measurement errors by a factor of 2. The larger scatter in the upper troposphere may be a consequence of convection. More consistent values are found in the lower stratosphere where the convective influence diminishes. The difference in the δD between the two regions may be used to place an upper bound to the dehydration by gradual freeze-drying. For instance, a 20% decrease in water VMR (from 5 ppmv to 4 ppmv) by gradual freeze-drying would produce additional depletion of $\sim 50\%$ in δD . There is no evidence for such depletion. We note, however, that the coarse resolution (~ 2 km vertical, ~ 200 km horizontal) of the ATMOS measurements may hide localized depletions of this magnitude, if ice lofting and evaporation produce a thin layer (< 1 km) of HDO-enriched moisture beneath the tropopause. In situ data are needed to resolve these fine scale structures. For the discussions in this paragraph, it is important that there is no significant altitude-dependent bias in the derived δD . We have examined the effects of systematic errors such as errors in the pressure broadening coefficients or the tangent temperature. They do not cause significant altitude-dependent biases in the TTL region (Appendix).

Our observations also show that the cessation of further fractionation starts at ~ 12 km, somewhat below the base of the TTL. This suggests evaporation of lofted ice as an important source of moisture at these altitudes as well. These altitudes roughly correspond to the region of maximum convective outflow [Folkins, 2002]. The air in this region does not ascend into the stratosphere. Instead, it joins the Hadley cell as it descends by radiative cooling and is advected towards the subtropics. As the dryness of the subtropical upper troposphere allows much of the Earth's surface radiation to escape

to the space, its behavior plays an important role in the water vapor feedback. Our results suggest that the amount of condensates that can be lofted and evaporated in the convective outflow may play a role in modulating the strength of this important feedback, a view that has not yet been generally accepted [*Held and Soden, 2000*].

1.5 Conclusions

The results presented here suggest that the widely held view that tropopause temperature acts as the only control on stratospheric humidity is too simplistic. This view has led researchers to point to specific regions as the “door” to the stratosphere, simply because the tropopause temperature there is sufficiently cold to produce the measured stratospheric water abundance [*Highwood and Hoskins, 1998; Newell and Gouldstewart, 1981*]. Others have suggested, based solely on inferred warmer tropical tropopause temperature, that during the Eocene (55 to 38 Ma), stratospheric water was much higher and therefore optically-thick polar stratospheric clouds could explain the warmth of the high latitudes [*Kirk-Davidoff et al., 2002*]. The results presented here question the validity of such a simplistic view. Changes in convection and cloud microphysics need to be included in understanding past and future stratospheric humidity changes [*Sherwood, 2002*].

1.6 Acknowledgements

We thank M. Salby for providing the 3-hourly 11- μm brightness temperature data, M. R. Gunson and the ATMOS science team for the acquisition and processing of the ATLAS-

3 spectra, and F.W. Irion and B. Sen for help with accessing them. We thank E. J. Moyer, S. C. Sherwood, and A. E. Dessler for helpful discussions.

1.7 Appendix

The purpose of this Appendix is to provide some details on the analysis of the ATMOS spectra. We shall describe the spectral intervals (or windows) used to retrieval HDO and H_2^{16}O with some representative spectra. We shall also evaluate the consistency among the different filters and the effect of some potential systematic errors.

Measurable HDO lines (~ 25 lines) for filter 9 spectra in the TTL mostly lie between 1300 and 1500 cm^{-1} . In this spectral range, the H_2O absorption is quite strong. Because of the strong increase in H_2O absorption with decreasing height, this spectral interval becomes saturated below ~ 10 km. Therefore, HDO abundance, in general, cannot be reliably retrieved from tropical filter 9 spectra below this altitude. Figure 1.4 displays a representative spectrum for HDO retrieval within the spectral range of filter 9. The spectra range from 1800 to 2000 cm^{-1} is suitable for the retrieval of H_2^{16}O . A representative spectrum is shown in Figure 1.5. The large residues are caused by unremoved solar absorption features [*Farmer and Norton, 1989*].

The main window used to retrieve the HDO abundance in the spectral region of filter 3 spans from 2675 cm^{-1} to 2795 cm^{-1} . It contains about 30 measurable HDO lines for the TTL occultations. Figure 1.6 shows a 4 cm^{-1} wide subset of this window at a tangent altitude of 10.6 km. The other absorption features in this sub-window are due to methane. With no H_2O absorption, this window remains unsaturated and HDO abundance can be retrieved at altitudes as low as 6 km.

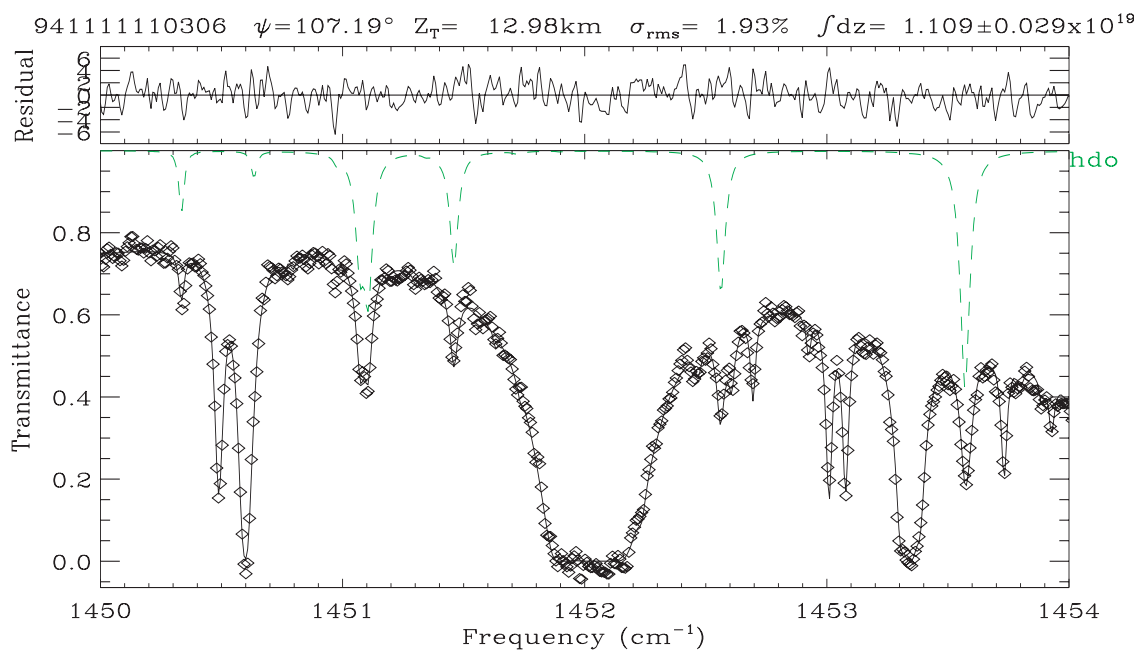


Figure 1.4 A representative spectral fit of HDO for filter 9 spectra. The diamonds are the measured spectrum, and the solid line is the calculated spectrum, and the dashed line is the absorption due to HDO. At the top of the figure, we list the spectrum name, the zenith angle ψ , tangent altitude, root-mean-square of the residual, and the number of gas molecules (in this case HDO) per cm^2 for the vertical column above the tangent altitude. The slant column in this case is ~ 163 times that of the vertical column. The error quoted is from fitting the window 1425-1455 cm^{-1} . Only a subset of that window is shown here.

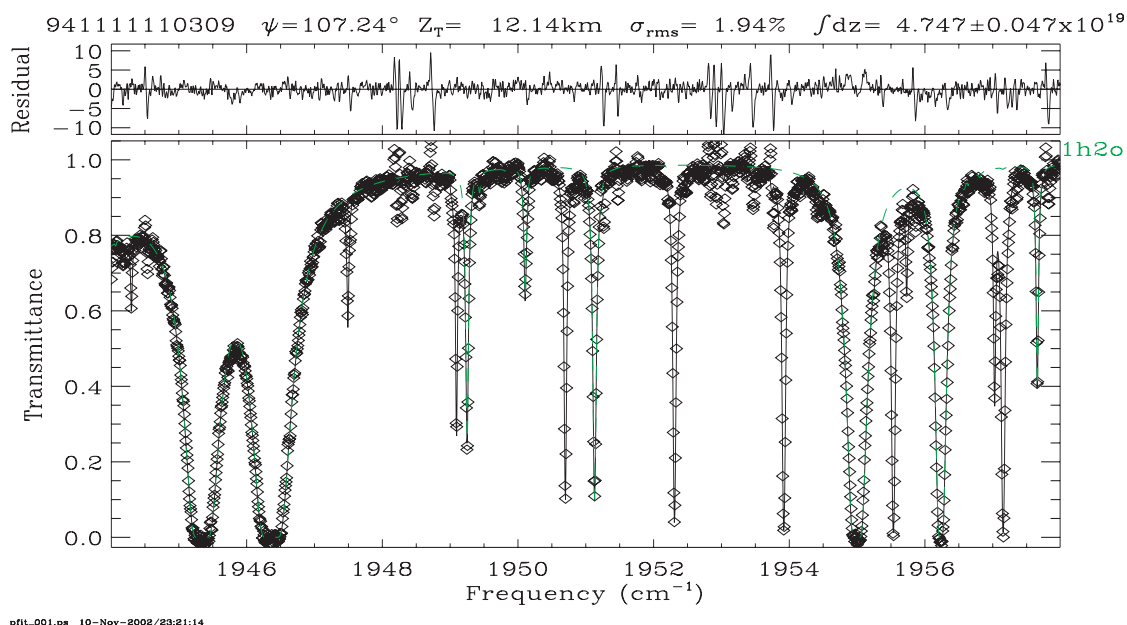


Figure 1.5 The same as Figure 1.4, except for a H_2^{16}O window (1h2o). The error quoted is from fitting the window 1944 -1958 cm^{-1} .

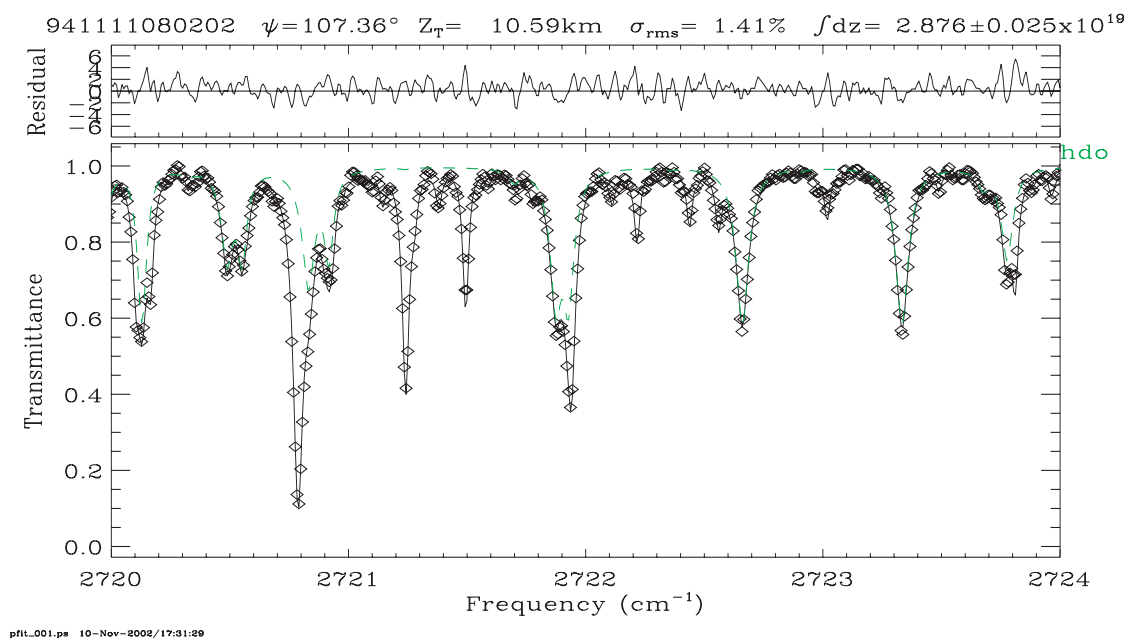


Figure 1.6 The same as Figure 1.4 except for a filter 3 spectrum. The error quoted is from fitting the window from 2675-2795 cm^{-1} .

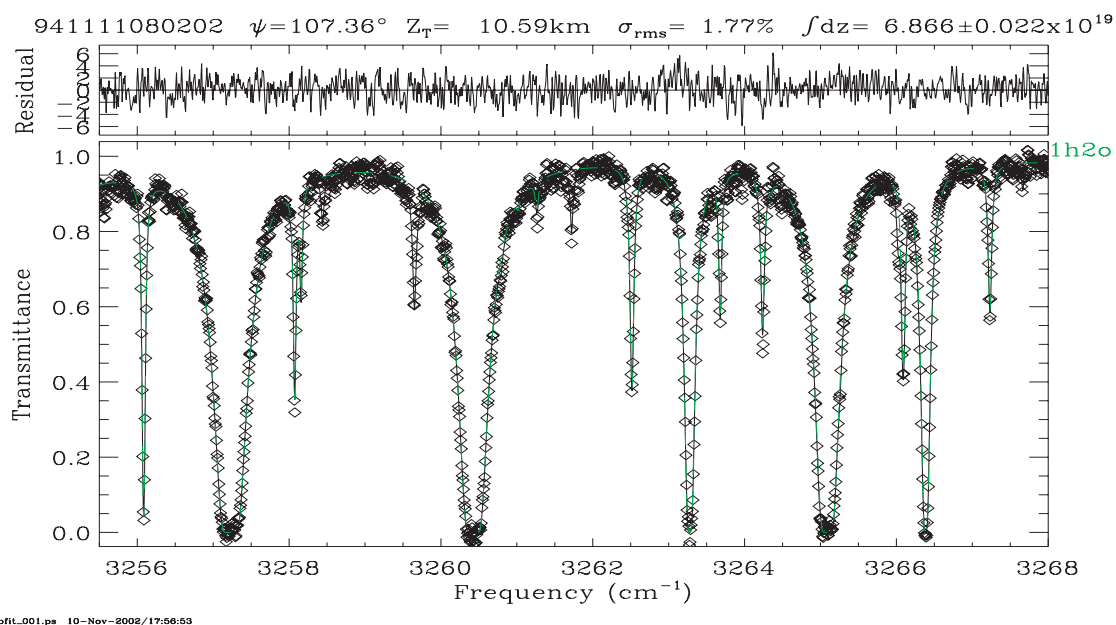


Figure 1.7 The same as Figure 1.6 except for H_2^{16}O . The error quoted is from fitting the window 3250-3301 cm^{-1} .

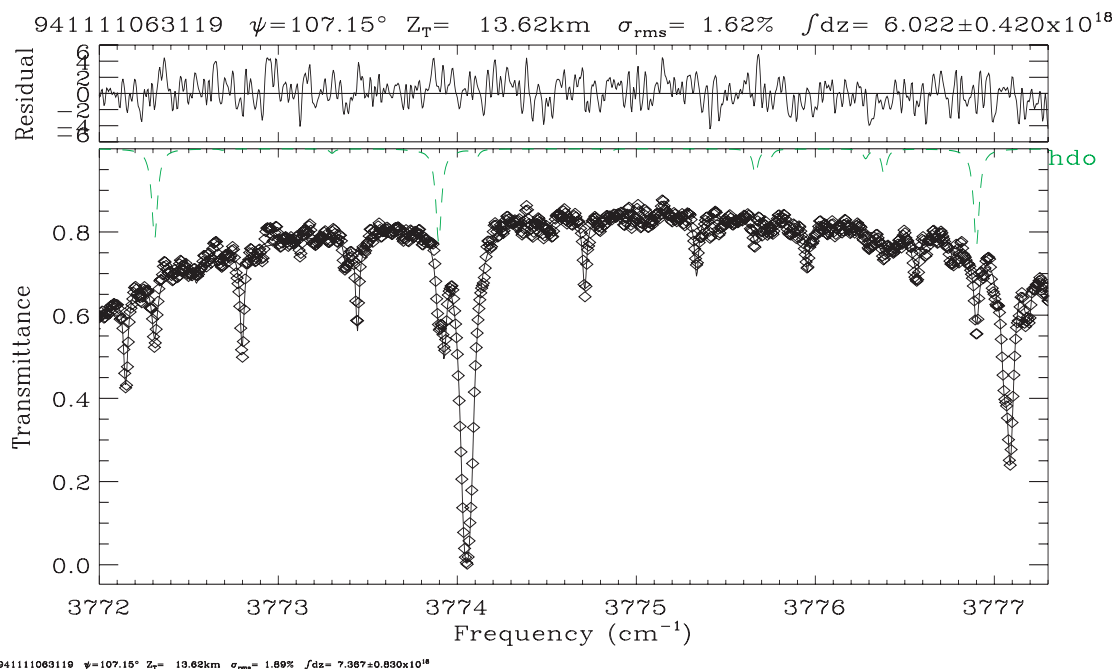


Figure 1.8 The same as Figure 1.4 except for a filter 4 spectrum. The error quoted is from fitting the window 3761-3378 cm^{-1} .

The window from 3205 to 3301 cm^{-1} is used to retrieve H_2^{16}O from the filter 3 and filter 4 spectra. A subset of this window is shown in Figure 1.7. This window is well suited for tropospheric H_2^{16}O retrievals. In fact, the continuum level in this window remains evident at 8-9 km.

There are fewer usable HDO lines (~ 10) for filter 4 spectra. These lines reside in the spectral range of 3760-3800 cm^{-1} . H_2O absorption is quite strong in this range. The continuum level is obscured by H_2O absorption at an altitude of 13 km (Figure 1.8). The absorption by H_2O limits the retrieval of HDO/ H_2O ratio from filter 4 spectra to altitudes above 10 km.

The consistency among the filters is examined using the Mark IV spectra, which covers the spectral range of 650-5650 cm^{-1} [Toon *et al.*, 1999]. The Mark IV FTIR is similar to the ATMOS instrument, although there are also some important differences. Each Mark IV spectrum is taken over a period of 210 seconds, while each ATMOS spectrum is taken within 2 seconds. The Mark IV spectra have very high signal-to-noise ratio ($\text{SNR} > 600$). The typical value for an Atlas-3 ATMOS spectrum is ~ 100 . The long scan time for the Mark IV instrument contributes to the high SNR. On the other hand, the solar intensity is more likely to vary during the measurement of a Mark IV spectrum. This may introduce additional non-random noise to the spectrum. Other factors, such as water trapped inside the instrument, pressure changes during the balloon ascents, also introduce errors that are specific to the Mark IV balloon spectra. Consequently, the residuals from fitting the Mark IV spectra tend to be dominated by systematic errors, while for the ATMOS spectra, the residuals are more randomly (Gaussian) distributed.

Despite these differences, the Mark IV spectra can still be used to examine systematic differences in the retrieved HDO from the different spectral windows. Five recent balloon flights (3 in 1997, 1 in 1999, and 1 in 2000) are used. As each Mark IV spectrum simultaneously covers the spectral range of 650 - 5650 cm^{-1} , HDO abundance can be retrieved using our identified spectral windows for each filter. The retrieved abundances are then compared among the filters.

We find that the spectral windows for filter 9 appear to yield HDO abundances 12% higher than those for filter 3 (Figure 1.9). There are 86 measurements in Figure 1.9, and the standard deviation is $\sim 2\%$. In the processing of the ATMOS data, we have reduced the HDO abundance retrieved from filter 9 by 12%. Filter 4 windows are found to agree with filter 3 windows within $\sim 2\%$ and no correction is made in processing the ATMOS filter 4 data. The choice of filter 3 as the standard is completely arbitrary, as we have no reason to suspect the HDO line intensity measurements in the 2700 cm^{-1} region to be more accurate than those in the 1400 cm^{-1} region. Correspondingly, the absolute values of δD are subject to a $\sim 50\%$ uncertainty, until the cause for the systematic difference between the spectral regions is understood. It is, therefore, important to realize that the results presented in this work are based on the relative variations in δD and not its absolute accuracy.

A more important issue is whether there are significant altitude dependent biases in the derived δD . Figure 1.10 shows the effects of systematic errors in the pressure broadening coefficients (5%) and the tangent temperature (3K). These are estimated by perturbing the parameters and repeating the δD retrievals. The difference between the results of the

perturbed run and the unperturbed run is shown in Figure 1.10. The effects of a pressure broadening coefficient error have considerably more scattering than those of a temperature error. This is perhaps because changes in the pressure broadening coefficients affect the shape of the absorption lines and have greater impacts on the spectral fits. A temperature change, on the other hand, can be more consistently compensated by a change in the gas slant column abundance. Effect of a 5% error in the pressure broadening coefficient on the derived δD is quite large (more than 20%). A 3 K error in the temperature can also induce a 10% error in the filter 9 spectra¹. Systematic biases with altitude, on the other hand, are found to be small (5% across the TTL).

¹ Low altitude (<11 km) filter 9 spectra (red) are more susceptible to systematic errors as the spectral windows tend to be saturated by H₂O absorption. This is not discussed here as we are mostly interested in higher altitudes.

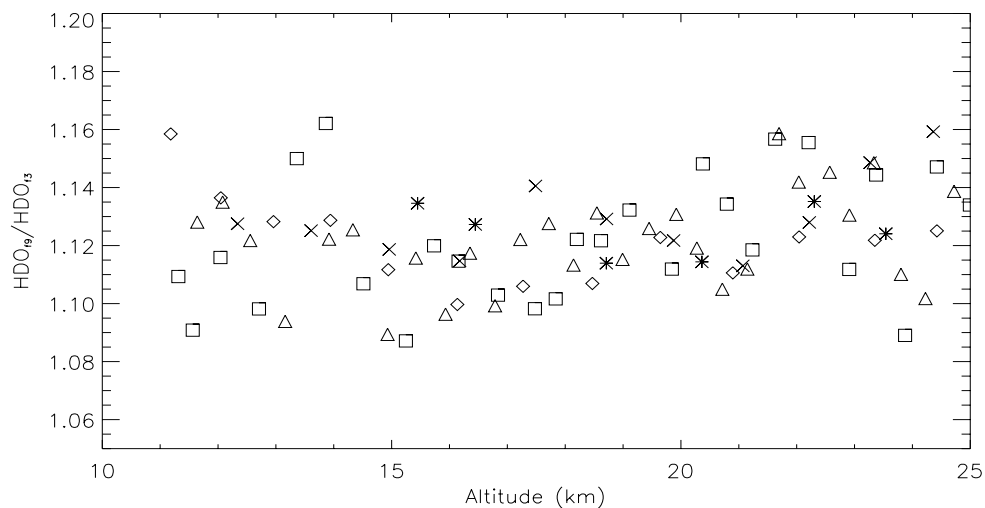


Figure 1.9 The ratio between the HDO slant columns derived using filter 9 windows and filter 3 windows for the tangent altitude range of 11-25 km. Spectra from five recent Mark IV balloon flights are used. The different flights are represented by different symbols.

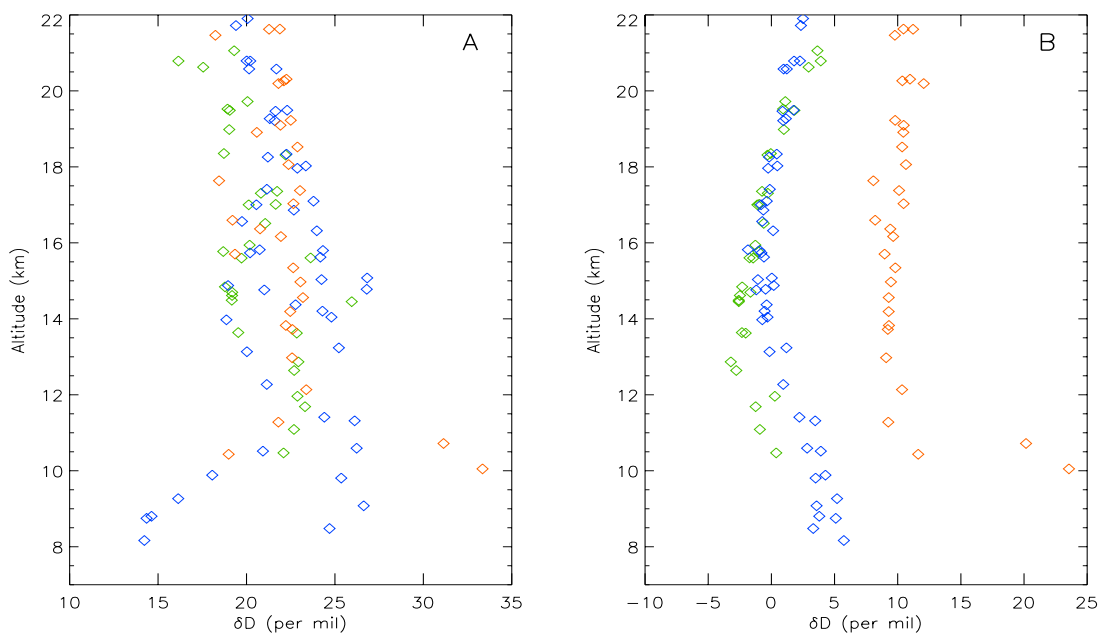


Figure 1.10 Variations in the derived δD due to a 5% increase in the pressure broadening half width (A) and a 3K increase in the tangent temperature (B), for the 11 tropical occultations. Filter 3 is shown in blue, f4, green, and f9, red.

1.8 Reference

- Atticks, M. G., and G. D. Robinson, Some features of the structure of the tropical tropopause, *Quarterly Journal of the Royal Meteorological Society*, 109 (460), 295-308, 1983.
- Brewer, A. W., Evidence for a world circulation provided by the measurements of Helium and water vapour distribution in the stratosphere, *Quarterly Journal of the Royal Meteorological Society*, 75 (326), 351-363, 1949.
- Brown, L. R., M. R. Gunson, R. A. Toth, F. W. Irion, C. P. Rinsland, and A. Goldman, 1995 Atmospheric Trace Molecule Spectroscopy (ATMOS) linelist, *Applied Optics*, 35 (16), 2828-2848, 1996.
- Danielsen, E. F., A dehydration mechanism for the stratosphere, *Geophysical Research Letters*, 9 (6), 605-608, 1982.
- Dessler, A. E., The effect of deep, tropical convection on the tropical tropopause layer, *Journal of Geophysical Research*, 107 (D3), 6-1, 2002.
- Farmer, C. B., and R. H. Norton, *A high-resolution atlas of the infrared spectrum of the sun and the earth atmosphere from space: a compilation of ATMOS spectra of the region from 650 to 4800 cm⁻¹ (2.3 to 16 μm)*, 2 v., National Aeronautics and Space Administration Office of Management Scientific and Technical Information Service, Washington, DC, 1989.
- Folkens, I., Origin of lapse rate changes in the upper tropical troposphere, *Journal of the Atmospheric Sciences*, 59 (5), 992-1005, 2002.
- Folkens, I., M. Loewenstein, J. Podolske, S. J. Oltmans, and M. Proffitt, A barrier to vertical mixing at 14 km in the tropics: Evidence from ozonesondes and aircraft

measurements, *Journal of Geophysical Research-Atmospheres*, 104 (D18), 22095-22102, 1999.

Forster, P. M. D., and K. P. Shine, Stratospheric water vapour changes as a possible contributor to observed stratospheric cooling, *Geophysical Research Letters*, 26 (21), 3309-3312, 1999.

Gedzelman, S. D., Deuterium in water vapor above the atmospheric boundary layer, *Tellus*, 40B (2), 134-147, 1988.

Gunson, M. R., M. M. Abbas, M. C. Abrams, M. Allen, L. R. Brown, T. L. Brown, A. Y. Chang, A. Goldman, F. W. Irion, L. L. Lowes, E. Mahieu, G.L. Manney, H.A. Michelsen, M.J. Newchurch, C.P. Rinsland, R.J. Salawitch, G.P. Stiller, G.C. Toon, Y.L. Yung, and R. Zander, The Atmospheric Trace Molecule Spectroscopy (ATMOS) experiment: Deployment on the ATLAS Space Shuttle missions, *Geophysical Research Letters*, 23 (17), 2333-2336, 1996.

Hartmann, D. L., J. M. Wallace, V. Limpasuvan, D. W. J. Thompson, and J. R. Holton, Can ozone depletion and global warming interact to produce rapid climate change? *Proceedings of the National Academy of Sciences of the United States of America*, 97 (4), 1412-1417, 2000.

Held, I. M., and B. J. Soden, Water vapor feedback and global warming, *Annual Review of Energy and the Environment*, 25, 441-475, 2000.

Highwood, E. J., and B. J. Hoskins, The tropical tropopause, *Quarterly Journal of the Royal Meteorological Society*, 124 (549), 1579-1604, 1998.

Holton, J. R., and A. Gettelman, Horizontal transport and the dehydration of the stratosphere, *Geophysical Research Letters*, 28 (14), 2799-2802, 2001.

-
- Holton, J. R., P. H. Haynes, M. E. McIntyre, A. R. Douglass, R. B. Rood, and L. Pfister, Stratosphere-Troposphere Exchange, *Reviews of Geophysics*, 33 (4), 403-439, 1995.
- Hoskins, B. J., Towards a PV-Theta view of the General-Circulation, *Tellus Series a-Dynamic Meteorology and Oceanography*, 43 (4), 27-35, 1991.
- Hurst, D. F., G. S. Dutton, P. A. Romashkin, P. R. Wamsley, F. L. Moore, J. W. Elkins, E.J. Hints, E.M. Weinstock, R.L. Herman, E.J. Moyer, D.C. Scott, R.D. May, and C.R. Webster, Closure of the total hydrogen budget of the northern extratropical lower stratosphere, *Journal of Geophysical Research-Atmospheres*, 104 (D7), 8191-8200, 1999.
- Irion, F. W., E. J. Moyer, M. R. Gunson, C. P. Rinsland, Y.L. Yung, H.A. Michelsen, R.J. Salawitch, A.Y. Chang, M.J. Newchurch, M.M. Abbas, M.C. Abrams, and R. Zanders, Stratospheric observations of CH₃D and HDO from ATMOS infrared solar spectra: Enrichments of deuterium in methane and implications for HD, *Geophysical Research Letters*, 23 (17), 2381-2384, 1996.
- Jensen, E. J., L. Pfister, A. S. Ackerman, A. Tabazadeh, and O.B. Toon, A conceptual model of the dehydration of air due to freeze-drying by optically thin, laminar cirrus rising slowly across the tropical tropopause, *Journal of Geophysical Research-Atmospheres*, 106 (D15), 17237-17252, 2001.
- Jensen, E. J., O. B. Toon, H. B. Selkirk, J. D. Spinhirne, and M. R. Schoeberl, On the formation and persistence of subvisible cirrus clouds near the tropical tropopause, *Journal of Geophysical Research-Atmospheres*, 101 (D16), 21361-21375, 1996.
- Johnson, D. G., K. W. Jucks, W. A. Traub, and K. V. Chance, Isotopic composition of stratospheric water vapor: Implications for transport, *Journal of Geophysical Research-Atmospheres*, 106 (D11), 12219-12226, 2001a.

-
- Johnson, D.G., K.W. Jucks, W.A. Traub, and K.V. Chance, Isotopic composition of stratospheric water vapor: Measurements and photochemistry, *Journal of Geophysical Research-Atmospheres*, 106 (D11), 12211-12217, 2001b.
- Jouzel, J., and L. Merlivat, Deuterium and O-18 in Precipitation - Modeling of the Isotopic Effects During Snow Formation, *Journal of Geophysical Research-Atmospheres*, 89 (ND7), 11749-11757, 1984.
- Keith, D.W., Stratosphere-troposphere exchange: Inferences from the isotopic composition of water vapor, *Journal of Geophysical Research-Atmospheres*, 105 (D12), 15167-15173, 2000.
- Kirk-Davidoff, D.B., E.J. Hints, J.G. Anderson, and D.W. Keith, The effect of climate change on ozone depletion through changes in stratospheric water vapour, *Nature*, 402 (6760), 399-401, 1999.
- Kirk-Davidoff, D.B., D.P. Schrag, and J. G. Anderson, On the feedback of stratospheric clouds on polar climate, *Geophysical Research Letters*, 29 (11), 1556-1559, 2002.
- Knollenberg, R.G., K. Kelly, and J.C. Wilson, Measurements of High Number Densities of Ice Crystals in the Tops of Tropical Cumulonimbus, *Journal of Geophysical Research-Atmospheres*, 98 (D5), 8639-8664, 1993.
- Merlivat, L., and G. Nief, Fractionnement Isotopique Lors Des Changements Etat Solide-Vapeur Et Liquide-Vapeur De Leau a Des Temperatures Inferieures a 0 Degrees C, *Tellus*, 19 (1), 122-&, 1967.
- Moyer, E.J., F.W. Irion, Y.L. Yung, and M.R. Gunson, ATMOS stratospheric deuterated water and implications for troposphere-stratosphere transport, *Geophysical Research Letters*, 23 (17), 2385-2388, 1996.
- Newell, R.E., and S. Gouldstewart, A Stratospheric Fountain, *Journal of the Atmospheric Sciences*, 38 (12), 2789-2796, 1981.

-
- Newton, C.W., and A.V. Persson, Structural Characteristics of the Subtropical Jet Stream and Certain Lower-Stratospheric Wind Systems, *Tellus*, 14 (2), 221-241, 1962.
- Plumb, R.A., and J. Eluszkiewicz, The Brewer-Dobson circulation: Dynamics of the tropical upwelling, *Journal of the Atmospheric Sciences*, 56 (6), 868-890, 1999.
- Potter, B.E., and J.R. Holton, The Role of Monsoon Convection in the Dehydration of the Lower Tropical Stratosphere, *Journal of the Atmospheric Sciences*, 52 (8), 1034-1050, 1995.
- Rosenlof, K.H., and J.R. Holton, Estimates of the Stratospheric Residual Circulation Using the Downward Control Principle, *Journal of Geophysical Research-Atmospheres*, 98 (D6), 10465-10479, 1993.
- Rosenlof, K.H., S.J. Oltmans, D. Kley, J.M. Russell, E.W. Chiou, W.P. Chu, D.G. Johnson, K.K. Kelly, H.A. Michelsen, G.E. Nedoluha, E.E. Remsberg, G.C. Toon, and M.P. McCormick, Stratospheric water vapor increases over the past half-century, *Geophysical Research Letters*, 28 (7), 1195-1198, 2001.
- Sen, B., G.C. Toon, J.F. Blavier, E.L. Fleming, and C.H. Jackman, Balloon-borne observations of midlatitude fluorine abundance, *Journal of Geophysical Research-Atmospheres*, 101 (D4), 9045-9054, 1996.
- Sherwood, S., A microphysical connection among biomass burning, cumulus clouds, and stratospheric moisture, *Science*, 295 (5558), 1272-1275, 2002.
- Sherwood, S.C., and A.E. Dessler, A model for transport across the tropical tropopause, *Journal of the Atmospheric Sciences*, 58 (7), 765-779, 2001.
- Shindell, D.T., Climate and ozone response to increased stratospheric water vapor, *Geophysical Research Letters*, 28 (8), 1551-1554, 2001.
- Smith, R.B., Deuterium in North-Atlantic Storm Tops, *Journal of the Atmospheric Sciences*, 49 (22), 2041-2057, 1992.

SPARC, Assessment of Upper Tropospheric and Stratospheric Water Vapour, WMO/TD-No. 1043, 2000.

Toon, G.C., J.F. Blavier, B. Sen, J.J. Margitan, C.R. Webster, R.D. May, D. Fahey, R. Gao, L. Del Negro, M. Proffitt, J. Elkins, P.A. Romashkin, D.F. Hurst, S. Oltmans, E. Atlas, S. Schauffler, F. Flocke, T.P. Bui, R.M. Stimpfle, G.P. Bonne, P.B. Voss, and R.C. Cohen, Comparison of MkIV balloon and ER-2 aircraft measurements of atmospheric trace gases, *Journal of Geophysical Research-Atmospheres*, 104 (D21), 26779-26790, 1999.

Toth, R.A., Water vapor measurements between 590 and 2582 cm^{-1} : Line positions and strengths, *Journal of Molecular Spectroscopy*, 190 (2), 379-396, 1998.

Toth, R.A., Air- and N-2-broadening parameters of HDO and D2O, 709 to 1936 cm^{-1} , *Journal of Molecular Spectroscopy*, 198 (2), 358-370, 1999a.

Toth, R.A., HDO and D2O low pressure, long path spectra in the 600-3100 cm^{-1} region I. HDO line positions and strengths, *Journal of Molecular Spectroscopy*, 195 (1), 73-97, 1999b.

Toth, R.A., Air- and N-2-Broadening parameters of water vapor: 604 to 2271 cm^{-1} , *Journal of Molecular Spectroscopy*, 201 (2), 218-243, 2000.

Toth, R.A., L.R. Brown, and C. Plymate, Self-broadened widths and frequency shifts of water vapor lines between 590 and 2400 cm^{-1} , *Journal of Quantitative Spectroscopy and Radiative Transfer*, 59 (6), 529-562, 1998.

Chapter 2: Space-borne Measurements of Atmospheric CO₂ by High-Resolution NIR Spectrometry of Reflected Sunlight

Zhiming Kuang¹, Jack Margolis², Geoffrey Toon², David Crisp², Yuk Yung¹

¹ Division of Geological and Planetary Sciences,
California Institute of Technology.

² Jet Propulsion Laboratory, California Institute
of Technology

Published in modified form in Geophysical Research
Letters, **29**, 1716-1719, 2002

2.1 Abstract

We introduce and explore a strategy for measuring the column-averaged CO₂ dry air volume mixing ratio X_{CO_2} from a satellite. It employs high-resolution spectra of reflected sunlight taken simultaneously in near-infrared (NIR) CO₂ (1.58- μm and 2.06- μm) and O₂ (0.76- μm) bands. Simulation experiments, performed to quantify the likely performance of such measurements, show that precisions of $\sim 0.3\text{-}2.5$ ppmv for X_{CO_2} can be achieved from individual clear sky soundings for a range of atmospheric/surface conditions when the scattering optical depth τ_s is less than ~ 0.3 . When averaged over many clear-sky soundings, random errors become negligible. This high precision facilitates the identification and correction of systematic errors, which are recognized as the most serious impediment for the satellite X_{CO_2} measurements. We briefly discuss potential sources of systematic errors, and show that some of them may result in geographically varying biases in the measured X_{CO_2} . This highlights the importance of careful calibration and validation measurements, designed to identify and eliminate sources of these biases. We conclude that the 3-band, spectrometric approach using NIR reflected sunlight has the potential for highly accurate X_{CO_2} measurements.

2.2 Introduction

Reliable predictions of future levels of atmospheric CO₂ require a quantitative understanding of both CO₂ emissions and the specific processes and reservoirs responsible for sequestering CO₂ [IPCC, 1995]. Measurements from a surface network are currently used to monitor atmospheric CO₂. Although these measurements are highly accurate, the network is too sparse to adequately characterize the geographic distribution of the CO₂ sinks and the processes controlling their variability [Sarmiento and Wofsy, 1999]. As a result, space-borne techniques are being sought to measure the column averaged CO₂ with more complete global coverage.

To surpass the performance of the existing surface network for inferring sources and sinks of atmospheric CO₂, inversion studies suggest that a precision of better than 2.5 ppmv is needed for global measurements of monthly mean column-averaged CO₂ dry air volume mixing ratio or vmr (X_{CO_2})² on a 8°×10° grid [Rayner and O'Brien, 2001]. In addition, because sources and sinks are inferred from spatial and temporal gradients in X_{CO_2} , these measurements must have no significant geographically varying biases. Here, we introduce a method to measure X_{CO_2} from space, and use simulated spectra to demonstrate that high precisions can be achieved. We briefly review effects of systematic errors and biases, but defer a more comprehensive investigation to later publications.

² We can formally define $X_{\text{CO}_2} = 0.2095 \times (\text{column CO}_2 / (\text{column O}_2))$. The term vmr is used for dry air volume mixing ratio throughout this paper.

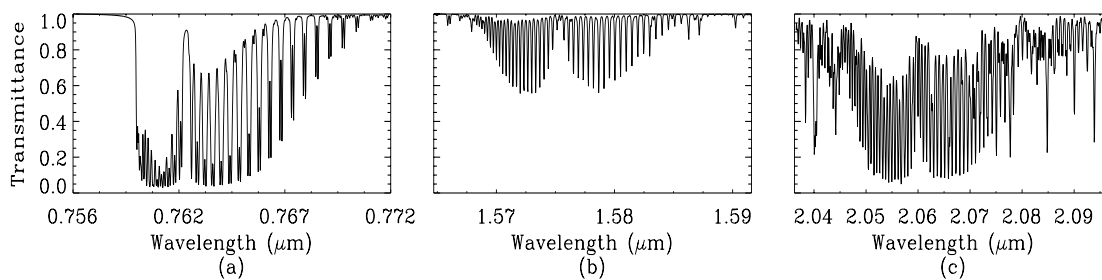


Figure 2.1 Simulated atmospheric transmission of the 0.76- μm O₂ A-band (a), 1.58- μm (b) and 2.06- μm (c) CO₂ bands for standard midlatitude summer atmosphere, assuming a solar zenith angle (SZA) of 35° and a nadir viewing geometry.

2.3 Measurement Strategy

To produce self-consistent estimates of retrieval precision, all results presented here are based on simulations of a practical satellite instrument design, which employs three spectrometers that simultaneously take high-resolution spectra of reflected sunlight in near-infrared (NIR) CO₂ and O₂ bands (Figure 2.1).

The 1.58- μm CO₂ band is well suited for retrieving column CO₂ because it is virtually free of interfering atmospheric absorbances, and is also sufficiently weak that the continuum level can be ascertained between the CO₂ lines even at high solar zenith angles (SZAs). A resolving power ($R=\lambda/\Delta\lambda$) of about 21,000 (i.e., the spectral resolution is about 0.075 nm), is sufficient to separate CO₂ lines from the underlying continuum. This facilitates the detection of wavelength-dependent variations of the surface albedo or airborne cloud and aerosol particles.

Spectra of the 1.58- μm CO_2 band alone, however, cannot yield X_{CO_2} with sufficient precision, because space-borne measurements of the absorption in this band are influenced by a number of factors besides the CO_2 vmr. Uncertainties in the surface pressure and the atmospheric path traversed by the reflected radiation can contribute errors in X_{CO_2} . Both topographic variations over land and local weather contribute uncertainties in surface pressure and total atmospheric mass in a CO_2 sounding. Scattering by clouds/aerosols further contributes to uncertainties in the atmospheric pathlength. Undetected water vapor variations introduce uncertainties in X_{CO_2} both by altering the dry-air fraction of the total atmospheric pressure, and by broadening the CO_2 lines more efficiently than O_2 and N_2 . All these factors must be explicitly constrained to retrieve X_{CO_2} to the required high precision (better than 2.5 ppmv).

As shown in previous studies [*O'Brien et al.*, 1998; *Stephens and Heidinger*, 2000], spectra of the O_2 A-band (0.76- μm) provide constraints on both the surface pressure and optical path-length variations associated with the scattering by clouds/aerosols. The fact that the O_2 A-band contains both weak and strong lines provides the additional information on the altitude distribution of cloud/aerosols. We will limit our discussion to relatively clear sky conditions (scattering optical depth $\tau_s < \sim 0.3$, as determined from the O_2 band).

The 0.76- μm O_2 band spectra alone, however, are not adequate for characterizing the scattering by clouds/aerosols in the 1.58- μm CO_2 band as cloud/aerosol optical properties (optical depth, single scattering albedo, and phase function) can vary substantially with

wavelength between the two bands. Although there is an O₂ band at 1.27 μm, closer to the 1.58-μm CO₂ band, it cannot be used for space-based O₂ observations as it produces intense, variable dayglow emission [Noxon, 1982].

We therefore use the CO₂ band at 2.06 μm in conjunction with the O₂ A-band to constrain the wavelength dependence of atmospheric scattering. This CO₂ band is sufficiently strong to be sensitive to scattering by cloud/aerosols. It also includes weak water vapor lines that can be used to provide direct constraints on the humidity. On the other hand, since lines in the 2.06-μm band are strongly saturated, this band is more susceptible to systematic errors and must not be used with the O₂ band alone for CO₂ measurements.

The spectral range of each spectrometer is chosen to cover the entire absorption band as well as some continuum at both ends of the band (Figure 2.1). The use of the entire band provides explicit constraints on the atmospheric temperature profile, because temperature affects strengths of the lines differently across the band in a well-known manner. The continuum at edges of the bands provides additional information about the wavelength dependent optical properties of the surface and airborne particles. For our analysis, we assume the resolving power ($R=\lambda/\Delta\lambda$) to be ~21,000 for the CO₂ bands and ~17,500 for the O₂ band. A small footprint (< 5 km²) was assumed to increase the chance of observing the entire atmospheric column in the presence of patchy clouds. It also helps to minimize spatial inhomogeneities (clouds, surface topography, shorelines, *etc.*) within individual samples that could introduce errors in the retrievals. We consider only

measurements with nadir viewing geometry in this study. Given the assumed resolving power and footprint size, we assume that the continuum signal-to-noise ratio (SNR), the SNR in spectral regions without significant gaseous absorption, is ~ 400 for the CO₂ bands and ~ 600 for the O₂ band in each spectral sample and in each footprint when SZA is 35° and the surface albedo is $\sim 6\%$. This performance can be achieved with photon-noise limited detectors and current spectrometer technologies.

2.4 Retrieval Approach

The X_{CO_2} retrieval algorithm involves three major components. The first is a spectrum-resolving (line-by-line), multi-stream multiple scattering model for producing synthetic radiance spectra in scattering, absorbing atmospheres [Crisp, 1997]. Here, the same model was used to generate the “observed” spectrum and the “retrieved” spectrum. For both applications, the atmosphere was divided into 11 layers with 8 levels in the troposphere. The second component simulates the instrument's spectral resolution, spectral range, sampling, wavelength-dependent line shape function, and throughput, as well as several instrument noise sources. The third component is an inverse method based on optimal estimation theory [Rodgers, 2000] for retrieving X_{CO_2} from the observed spectra. This model simultaneously retrieves several properties of the atmospheric and surface state \mathbf{x} , e.g. cloud, aerosol, temperature, humidity and surface pressure, albedo, as well as the CO₂ vmr.

The function $f(\mathbf{x})$ is used to denote the forward model, which includes the radiative transfer and the instrumental response components. The resulting synthetic spectra at the

three selected bands simulate the measurements obtained from a single sounding, denoted as \mathbf{y} . The measurement process can thus be written as $\mathbf{y}=\mathbf{f}(\mathbf{x})+\boldsymbol{\varepsilon}$, where $\boldsymbol{\varepsilon}$ denotes the measurement error.

We fit the three synthetic spectra simultaneously for the atmospheric/surface state using the optimal retrieval theory, which seeks to minimize the cost function

$$\chi^2=[\mathbf{y}-\mathbf{f}(\mathbf{x})]^T\mathbf{S}_\varepsilon^{-1}[\mathbf{y}-\mathbf{f}(\mathbf{x})]+(\mathbf{x}-\mathbf{x}_a)^T\mathbf{S}_a^{-1}(\mathbf{x}-\mathbf{x}_a) \quad (1)$$

where \mathbf{x}_a is the *a priori* state, \mathbf{S}_a is the *a priori* covariance, and \mathbf{S}_ε is the measurement error covariance. We assume the measurement errors to be Gaussian. We also assume that they are independent between pixels so that \mathbf{S}_ε is diagonal.

A principal feature of the optimal retrieval theory is the use of *a priori* constraints, which represent the *a priori* distribution of expected values for each parameter in the atmospheric state vector and the expected joint distribution between the parameters. For some variables, the *a priori* constraints can be estimated from existing climatological data (temperature, humidity profiles, and surface pressure) and model outputs (CO₂ profiles). For other properties, such as cloud and aerosol profiles, *ad hoc* constraints were constructed based on a Markov description of the profiles [Rodgers, 2000]. For the retrieval experiments presented here, we assumed that cloud/aerosols vary on a vertical scale height of about 200 mb, 500 mb and 300 mb in the planetary boundary layer (PBL), the free troposphere, and the stratosphere, respectively. The standard deviation in the scattering optical depth of each of the 11 layers is assumed to be ~50%, and to vary

independently in the 2.06- μm and 0.76- μm bands. Scattering at 1.58 μm is interpolated from those of the other two bands. This approach will introduce little error if the wavelength dependence of the scattering is known or if it varies smoothly between 0.76 and 2.06 μm . For the experiments presented here, we included in the *a priori* constraints an interpolation error of $\sim 3\%$. The validity of these assumptions is discussed in the Discussion section. The band averaged albedos are considered to vary by $\sim 30\%$ and are independent among the three bands. We assume no covariance between different quantities (*e.g.*, between CO_2 and temperature).

In our retrieval experiments, the forward model is linearized around each atmospheric/surface state, giving a weighting function matrix $[K_{ij}] = \partial f_i / \partial x_j$. Figure 2.2 shows the band averaged weighting function (*i.e.*, $\overline{K_j} = \left[\sum_i K_{i,j}^2 / \varepsilon_i^2 \right]^{1/2}$) for CO_2 variations versus pressure levels, for cases with (solid line) and without (dashed line) atmospheric scattering. These weighting functions include contributions from both the 1.58- μm and 2.06- μm CO_2 bands. The sensitivity to CO_2 is maximum near the surface, where most CO_2 sources and sinks are located. In contrast, thermal IR techniques have poor sensitivity at low altitudes because the thermal contrast between the surface and the near-surface atmosphere is usually small [Engelen *et al.*, 2001]. When atmospheric scattering is present, the sensitivity to low altitude CO_2 vmr decreases (dashed line in Figure 2.2).

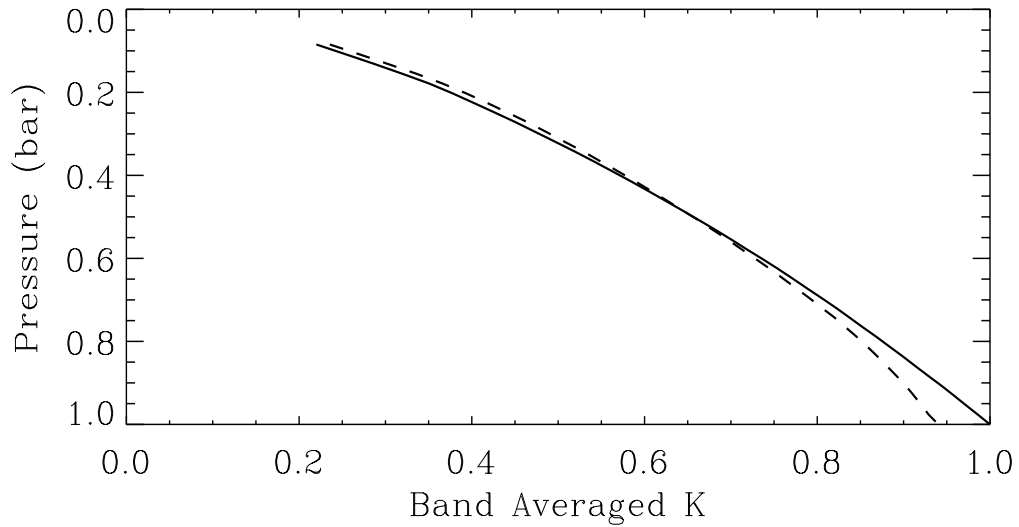


Figure 2.2 Band-averaged weighting function for CO₂ variations at different pressure levels with no atmospheric scattering (solid) and with $\tau_s=0.1$ (dashed). The weighting functions were scaled by the weighting at 1 bar level when $\tau_s=0$.

2.5 Achievable Precisions

A linear covariance analysis was conducted to study the achievable precisions. The posterior covariance for the state variables is

$$\mathbf{S}=(\mathbf{K}^T\mathbf{S}_\varepsilon^{-1}\mathbf{K}+\mathbf{S}_a^{-1})^{-1} \quad (2)$$

The quantity X_{CO_2} , can be obtained by averaging the CO₂ profile, *i.e.*, $X_{\text{CO}_2}=\mathbf{h}^T\mathbf{x}$, where \mathbf{h} is a vector that represents the vertical pressure-weighted averaging. The formal error variance in the retrieved X_{CO_2} is thus $\mathbf{h}^T\mathbf{S}\mathbf{h}$.

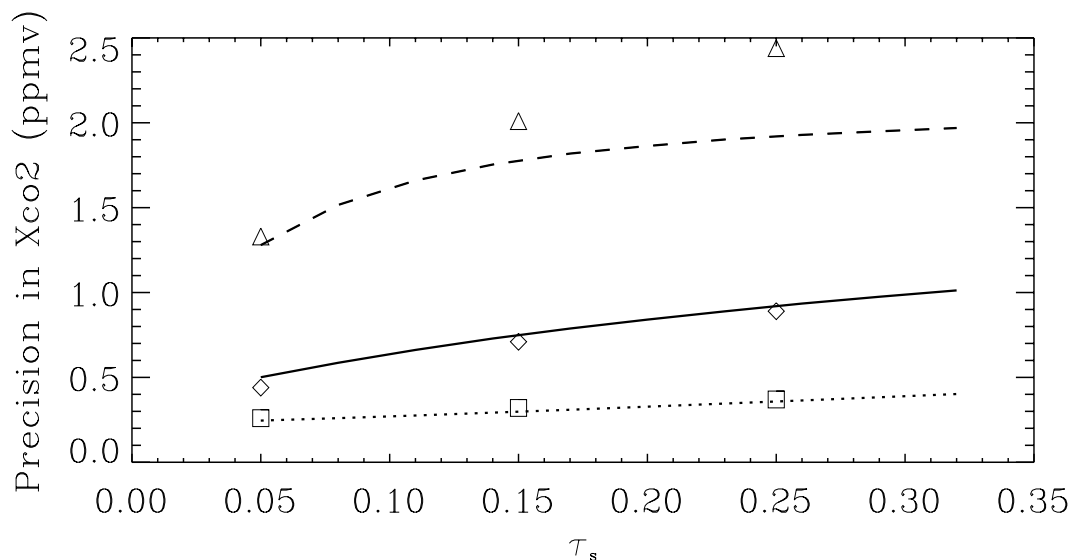


Figure 2.3 Achievable X_{CO_2} precisions calculated from linear covariance analysis versus the total scattering optical depth τ_s for SZA=35° over the ocean (solid), over the land (dotted), and SZA=75° over the ocean (dashed). The symbols (Δ , \diamond , \square) represent the single sounding precisions obtained from retrieval experiments for a few selected cases. We have assumed that scattering at 1.58 μm can be interpolated from the other two bands to $\sim 3\%$ accuracy.

Figure 2.3 shows the achievable precisions over the ocean (albedo is 0.06) for SZAs of 35° and 75° for a range of total scattering optical depth τ_s . The precision worsens with increasing τ_s and SZA. The former is due to the fact that most CO_2 variation is in the lower atmosphere, especially in the PBL. Increasing τ_s thus decreases the sunlight that passes through this region and reduces the sensitivity to CO_2 changes there. The poorer precisions at high SZAs are mainly due to the reduced SNR, since less sunlight is intercepted by a unit area. For τ_s between 0.05-0.30, the precision for a single sounding is ~ 0.4 to 0.9 ppmv for SZA=35° (solid), and ~ 1.3 to 2.5 ppmv for SZA=75° (dashed). The *a priori* error on X_{CO_2} is ~ 8 ppmv. If the 2.06- μm CO_2 band is not used, the achievable

precisions worsen by more than a factor of two (not shown). Similar estimates made for observations over land show better precisions, $\sim 0.3\text{-}0.4$ ppmv, (Figure 2.3, dotted line) as the higher albedo over land (a value of 0.2 was used) increases the SNR and reduces the relative contribution to the observed signal from light scattered by cloud/aerosols.

Results from linear covariance analysis were tested against retrieval experiments. About 300 of atmospheric/surface states were constructed consistent with the *a priori* constraints so that they cover the plausible climatological range. For each of the prescribed atmospheric/surface conditions, synthetic spectra were generated and subsequently retrieved for the atmospheric/surface state. Precisions were evaluated by comparing the retrieved quantities with the prescribed values. Results from a few such experiments are shown in Figure 2.3. The achieved precisions from these simulations agree well with the linear covariance estimates for low cloud/aerosol loadings or low SZAs. At high SZAs and with high cloud/aerosol loadings, the achieved precisions from the retrieval experiments become worse than the linear covariance estimates. This is presumably due to the increasingly nonlinear nature of the retrieval problem as scattering becomes more important.

For a space-borne CO₂ sensor in a high inclination orbit, thousands of soundings could be acquired on monthly to seasonal timescales on spatial scales of $8^\circ \times 10^\circ$. Therefore, averaging large numbers of clear sky soundings will be possible except for regions with persistent overcast conditions, rendering random error negligible (Figure 2.4). Note that the random errors decrease at a rate slower than the square root of the number of soundings, as the *a priori* errors tend to correlate with each other for nearby soundings. In

Figure 2.4, we have assumed the *a priori* errors to be perfectly correlated so that they do not improve through averaging.

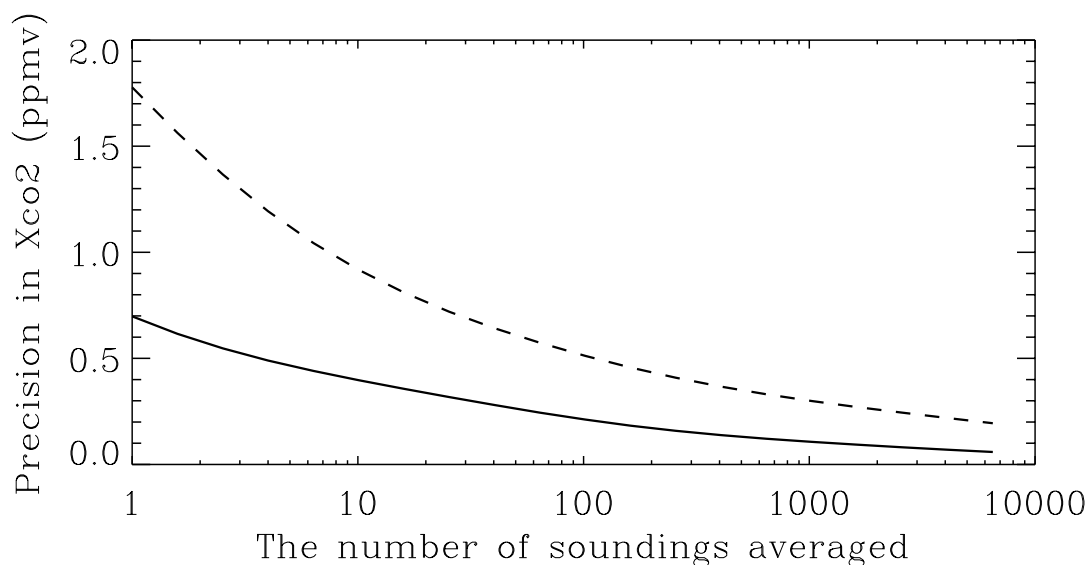


Figure 2.4 Precisions of X_{CO_2} retrievals as a function of the number of soundings averaged for $SZA=35^\circ$ (solid) and 75° (dashed). Both cases have a surface albedo of 0.06 and a τ_s of ~ 0.15 .

Effects of wavelength-dependent surface albedo due to mineral features, plankton, *etc.*, have been simulated by including in the state vector slow variations in the surface albedo of each band $\sim 30\%$ on the scale of ~ 3 nm. We find that they do not significantly affect the achievable precision. This is expected because the spectral scale of the surface colors is much broader than that of the gaseous CO_2 features, and can be resolved explicitly in the continuum between the lines throughout each band. The effect of water vapor broadening of CO_2 lines was not tested in the above calculations. But these effects are reasonably well understood [Rosenmann *et al.*, 1988], and will be described in subsequent work. This factor should not significantly reduce the accuracy of X_{CO_2}

retrievals because water vapor is well constrained by spectra acquired in the 2.06- μm band.

2.6 Systematic Errors and Potential Biases

The preceding analysis assumes that the forward model is perfect. In practice, there will inevitably be inadequacies in the representation of the characteristics of the instrument (*e.g.*, uncertainties in the instrument line shape, zero offset, detector nonlinearity, polarization *etc.*), and in the atmospheric radiative transfer (*e.g.*, errors in the gas absorption line database, oversimplifications in the treatment of radiative transfer). These inadequacies will introduce systematic errors in the X_{CO_2} measurements. For the purpose of characterizing the carbon sources and sinks, it is critical that the measurements are free of spatially and temporally coherent biases, *i.e.*, systematic errors that vary with geographic location, SZA, or surface type. As an example of such a systematic error, we consider the effect of an uncorrected zero offset error due to excess dark current in the detector of the 1.58- μm region. This error adds a constant radiance offset to each spectrum, decreasing the fractional depths of the CO_2 absorption lines. The magnitude of the induced systematic error depends on the absorption depth of the CO_2 lines and the continuum radiance level; the former varies with SZA and the latter varies with both surface albedo and SZA. For dark surfaces or high SZAs, the signal gets weaker, and the error induced in X_{CO_2} gets larger, as shown in Figure 2.5. Since surface albedo is typically much larger over land than ocean, a given zero level offset error would reduce the X_{CO_2} less over land than over ocean, resulting in a spurious oceanic sink of CO_2 .

Similarly, since the high latitude observations are generally made at higher solar zenith angles than the low latitude observations, the zero level offset error would reduce the X_{CO_2} less in the tropics than in the polar regions, leading to a spurious high latitude CO_2 sink.

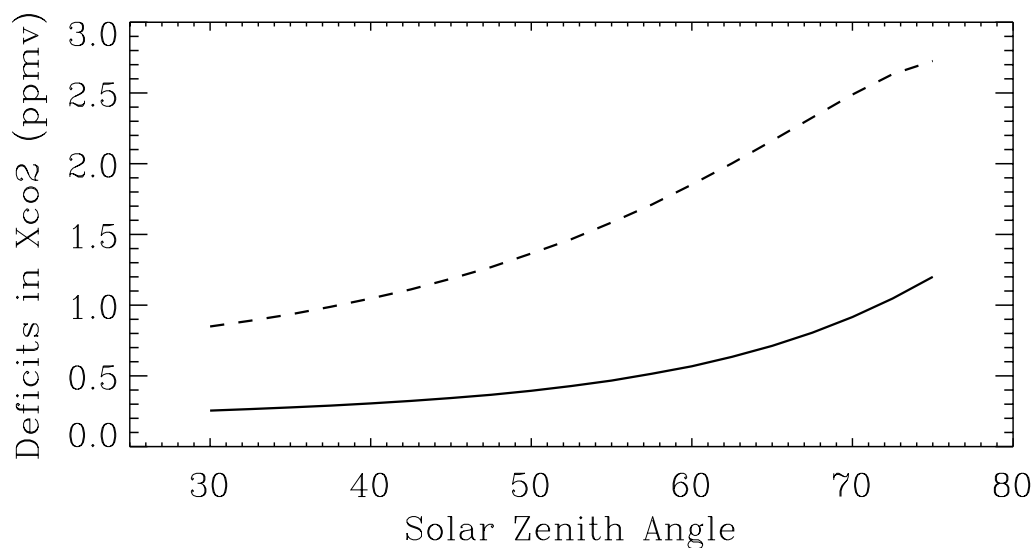


Figure 2.5 Deficits in X_{CO_2} due to a constant zero offset error over the ocean (surface albedo of 0.06, dashed line) and over the land (surface albedo of 0.2, solid line) as a function of SZA. The zero offset error is 0.2% of the continuum level for an albedo of 0.06 at 35° SZA. All cases have a τ_s of ~ 0.05 .

Fortunately, there are two factors that mitigate the impact of the systematic errors: 1) In the high-resolution, spectrometric approach, many types of systematic errors will produce distinctive spectral signatures. The high SNR that is attainable using reflected NIR sunlight facilitates the detection of these residuals, and provides the information needed to deduce their origin and test the efficacy of any corrections. 2) Validation experiments

that combine accurate ground-based and airborne CO₂ profiling capabilities provide an effective way for identifying and quantifying biases with large spatial scales. While the amplitude of systematic errors will vary with location, their sources will vary slowly in many cases (as in the zero offset example). Such errors can be corrected by careful calibration and validation measurements.

Sampling biases may also affect the inference of carbon sources and sinks, even if the X_{CO₂} retrievals are perfect. For instance, the solar NIR method only measures X_{CO₂} during the day under clear-sky conditions. However, in many ecosystems, photosynthesis is stronger in these conditions such that the measured X_{CO₂} could be lower than average. To mitigate the impact of such sampling errors, the space based X_{CO₂} measurements must be combined with time-resolved *in situ* data, and analyzed with carbon chemical tracer transport models that properly account for the measurement time and observing conditions. Such models are being developed [Rayner *et al.*, 2002].

2.7 Discussion

Although the *a priori* constraints used here were somewhat crude, they were sufficiently loose so that they did not excessively constrain the retrieval of X_{CO₂}. In the analysis of real satellite observations, these constraints can be improved by both establishing a more reliable climatology and using the preceding adjacent retrievals along the satellite track, so that the retrieval precisions will be further improved.

The interpolation of scattering properties measured at 0.76 μm and 2.06 μm to 1.58 μm warrants more discussion. For aerosols whose optical properties change slowly over this range of wavelengths (*e.g.*, small sulfate particles, black carbon), interpolation by the simple Angstrom relation $\tau \propto \nu^n$ can be accurate to about a 1% level, even without *a priori* knowledge of the coefficient n or the actual aerosol type. Airborne particles whose optical properties do not change uniformly with wavelength, however, need to be typed in order to do an accurate interpolation. The high-resolution measurements provide additional constraints on the particle type. For example, the 2.06- μm band and the 1.58- μm band are on the edge of strong water ice absorption features. A thin cirrus ice cloud can thus be clearly identified since it produces a significant slope in the continuum and also changes the shapes of the cores of saturated lines. Ubiquitous airborne dust and long-lived soluble aerosols pose special problems as they have variable compositions and size distributions that can yield a range of spectral signatures at NIR wavelengths. The identification and characterization of these aerosols warrant further investigation. We have assumed that scattering at 1.58 μm can be interpolated from the other two bands with an accuracy of $\sim 3\%$. A different choice of the interpolation error, *e.g.*, 10% or 1%, worsens or improves the achievable precision by less than 20-30%.

2.8 Summary and Conclusions

We have introduced a method of measuring X_{CO_2} from the space using high-resolution NIR spectrometry of reflected sunlight. The simultaneous use of the CO_2 (1.58- μm and 2.05- μm) and O_2 (0.76- μm) bands allows small changes in the spectrum arising from

variations of X_{CO_2} to be distinguished from larger spectral changes arising from variations of other atmospheric/surface parameters (*e.g.*, water vapor, cloud, aerosol, temperature, surface pressure, surface albedo). Using prototype retrieval simulations based on a practical satellite instrument design, we show that it is possible to retrieve X_{CO_2} to precisions of $\sim 0.3\text{-}2.5$ ppmv from a single, clear-sky sounding ($\tau_s < \sim 0.3$) for a range of atmospheric and surface conditions. Thousands of such soundings are expected at regional scales on monthly intervals, and can be combined to reduce the effects of random measurement errors over all but the most persistently cloudy regions. The main challenge is therefore to avoid systematic measurement errors that can introduce geographically dependent biases. These factors highlight the need for a careful calibration and validation program, designed to identify and eliminate these biases. We conclude that the 3-band, high-resolution, spectrometric approach using NIR reflected sunlight has the potential for highly accurate X_{CO_2} measurements.

2.9 Acknowledgements

We thank two anonymous referees and members of the OCO Team for valuable comments. This research was supported in part by a NASA grant to the Jet Propulsion Laboratory and the Caltech President's Fund. ZMK and YLY were supported by NASA grants NAG5-7230, NAG1-1806 to Caltech.

2.10 References

Crisp, D., Absorption of sunlight by water vapor in cloudy conditions: A partial explanation for the cloud absorption anomaly, *Geophys. Res. Lett.*, **24**, 571-574, 1997.

Engelen, R. J., A. S. Denning, K. R. Gurney, and S. G. L., Global observations of the carbon budget. 1. Expected satellite capabilities for emission spectroscopy in the EOS and NPOESS eras, *J. Geophys. Res.*, **106**, 20055-20068, 2001.

IPCC, Intergovernmental Panel on Climate Change Second Assessment: Climate Change 1995, p. 73, 1996.

Noxon, J., A global study of O₂ 1-delta Airglow - Day and twilight, *Planet Space Sci*, **30**, 545-557, 1982.

O'Brien, D. M., R. M. Mitchell, S. A. English, and G. A. Da Costa, Airborne Measurements of air mass from O₂ A-band absorption spectra, *J. Atmos. Oceanic Technol.*, **15**, 1272-1286, 1998.

Rayner, P. J., and D. M. O'Brien, The utility of remotely sensed CO₂ concentration data in surface source inversions, *Geophys. Res. Lett.*, **28**, 175-178, 2001.

Rayner, P. J., R. N. Law, D. M. O'Brien, T. M. Butler, and M. Dilley, Global observations of the carbon budget: III Initial assessment of the impact of satellite orbit, scan geometry and cloud on measuring CO₂ from space, *J. Geophys. Res.*, in press, 2002.

Rodgers, C. D., Inverse methods for atmospheric sounding: Theory and practice, 238 pp., World Scientific, Inc., 2000.

Rosenmann, L., J. M. Hartmann, M. Y. Perrin, and J. Taine, Accurate calculated tabulations of IR and Raman CO₂ line broadening by CO₂, H₂O, N₂, O₂ in the 300-2400K temperature range, *Appl. Optics*, **27**, 3902-3907, 1988.

Sarmiento, J. L., and S. C. Wofsy, A U.S. Carbon Cycle Science Plan, 1999.

Stephens, G. L., and A. Heidinger, Molecular line absorption in a scattering atmosphere. Part I: Theory, *J. Atmos. Sci.*, **57**, 1599-1614, 2000.

Part II: Interannual Variations of the Earth's Reflectance

Chapter 3: Interannual Reflectance Variations of the Earth: An Overview

Part of the materials in this Chapter was presented in

Kuang, Z.M., Y.B. Jiang, and Y.L. Yung, Cloud optical thickness variations during 1983-1991: Solar cycle or ENSO? *Geophysical Research Letters*, 25 (9), 1415-1417, 1998.

3.1 Introduction

The earth's reflectance is an important aspect of the earth's climate. Simple assumption about its response to climate variations can lead to some interesting conclusions, such as the stability of a snowball Earth. Reflectance variations associated with changes in, for example, the sea ice, or the oceanic stratus, have been conjectured to play important roles in climate variability [*Budyko, 1969; Klein and Hartmann, 1993*].

Satellites have enabled global reflectance measurements from the space. The most comprehensive measurements of the earth's radiation budget were obtained from the Earth Radiation Budget Experiment (ERBE) [*Barkstrom, 1984*], and are distributed by the NASA Langley atmospheric sciences data center. The combination of scanner and non-scanner measurements from a suite of satellites provided a global coverage from November 1984 to February 1990. The wide field of view (WFOV) non-scanner on board of the Earth Radiation Budget Satellite (ERBS) continues to function to this date. The non-scanner data cover the latitude range from 60°S to 60°N, and is believed to maintain a good calibration up to September 1999 [*Wielicki et al., 2002*]. However, due to the orbital precession of the ERBS satellite, the monthly mean measurements can have large temporal sampling noises [*Bess et al., 1999*]. This problem is particularly severe for short wave measurements at higher latitudes. In the new edition of the ERBE non-scanner data, there is a significant amount of missing data in the midlatitude shortwave measurements due to excessive temporal sampling error.

The weather satellites have also been measuring the earth's reflectance. However, as they were designed for weather studies, their long-term stability and the inter-calibration among the satellites are insufficient for the study of interannual variations [Brest *et al.*, 1997]. As a consequence, a comprehensive study of the interannual variability of the Earth's reflectance has not yet been made. In this chapter, we shall argue that the ultraviolet (UV) reflectance measured by the Total Ozone Mapping Spectrometer (TOMS) on board of the Nimbus-7 satellite [Herman *et al.*, 2001a] can be used to fill this gap. In section 3.2, we shall describe the TOMS data, and why it is suitable for the study of interannual reflectance variations. A comparison with the ERBE data is presented in the Appendix. In section 3.3, we shall examine the variations of the globally averaged reflectance. Implications on the suggested influence by cosmic rays on the Earth's global cloud cover will be discussed [Svensmark, 1998; Svensmark and FriisChristensen, 1997]. We will then provide an overview on the global distribution of the interannual reflectance variability (Section 3.4). More detailed studies of reflectance variations over the polar sea ice covered regions and the northern midlatitude oceans are presented in later chapters.

3.2 Data

The TOMS reflectance is measured at an ozone non-absorbing ultraviolet (UV) wavelength (380nm) [Herman *et al.*, 2001a]. The Nimbus-7 satellite's local-noon orbit and the instrument's cross-track scanning feature allow a complete daily coverage except for regions in polar night. The reflectance R is essentially determined by removing the effect of Rayleigh scattering above an assumed Lambertian surface [Dave, 1978]. A

correction for the different pressures of the cloud layer and the ground was applied [Herman *et al.*, 2001a]. The Nimbus-7 version-7 TOMS reflectance data is available for over 14 year (November 1978-May 1993). The long-term stability of the derived R is estimated to be ~ 0.2 reflectance unit (RU)³ [Herman *et al.*, 2001b]. This relatively long temporal coverage and the high long-term stability make the Nimbus-7 TOMS reflectance an attractive dataset for examining interannual variations. The field of view (FOV) of the TOMS instrument is 50×50 km at nadir and 150×200 km at extreme off-nadir angles. The daily and monthly data that will be used have been aggregated into a 1.25° longitude \times 1° latitude grid. Monthly averages for a grid box were computed only for the months with at least 20 days of good daily data. We note that the local noon measurement time of TOMS may introduce a temporal sampling bias. However, as the local noon is when the solar radiation is the strongest, for monthly averages, severe temporal sampling bias problem is not expected except in regions with strong and persistent diurnal cloud variations. Additional discussion is provided in the Appendix.

The TOMS reflectance is believed to approximate the UV albedo of the scene [Herman *et al.*, 2001a]. As the TOMS instrument scans perpendicular to the principal plane of the reflection, the number of measurements in the direct forward scattering or back scattering directions is reduced. More importantly, the strong Rayleigh scattering of the atmosphere greatly reduces the anisotropy of the UV reflection. The large FOV of the TOMS instrument further averages out the anisotropic reflection of individual cloud/surface

³ The reflectance and albedo are expressed in reflectance unit (RU) instead of percent to avoid confusion, following Herman *et al.* 2001. 1 RU=1% reflectance.

features. A much reduced anisotropy in the TOMS reflectance measurements is supported by angular dependence models constructed for UV radiation [*Pubu and Li, 2001*].

Besides being relatively long and well calibrated, the TOMS UV measurements have some additional advantages over visible measurements for studying cloud variations.

Herman and Celarier [1997] noted that the surface reflectance in the UV is smaller and less variable than that in the visible for snow/ice free areas. Moreover, in the study of the visible albedo, it is often noted that the cloud albedo has a strong dependence on solar zenith angle (SZA): for the same cloud field, the albedo increases with the SZA. This dependence, while also exists in the UV, is greatly reduced because of the strong Rayleigh scattering. This point is further demonstrated by a comparison between the ERBE and the TOMS measurements in the Appendix.

The mean distributions of the TOMS reflectance have been documented [*Herman et al., 2001a*]. For reference, Figure 3.1 displays the mean reflectance for January (a) and July (b). Readers are referred to *Herman et al. [2001a]* for details.

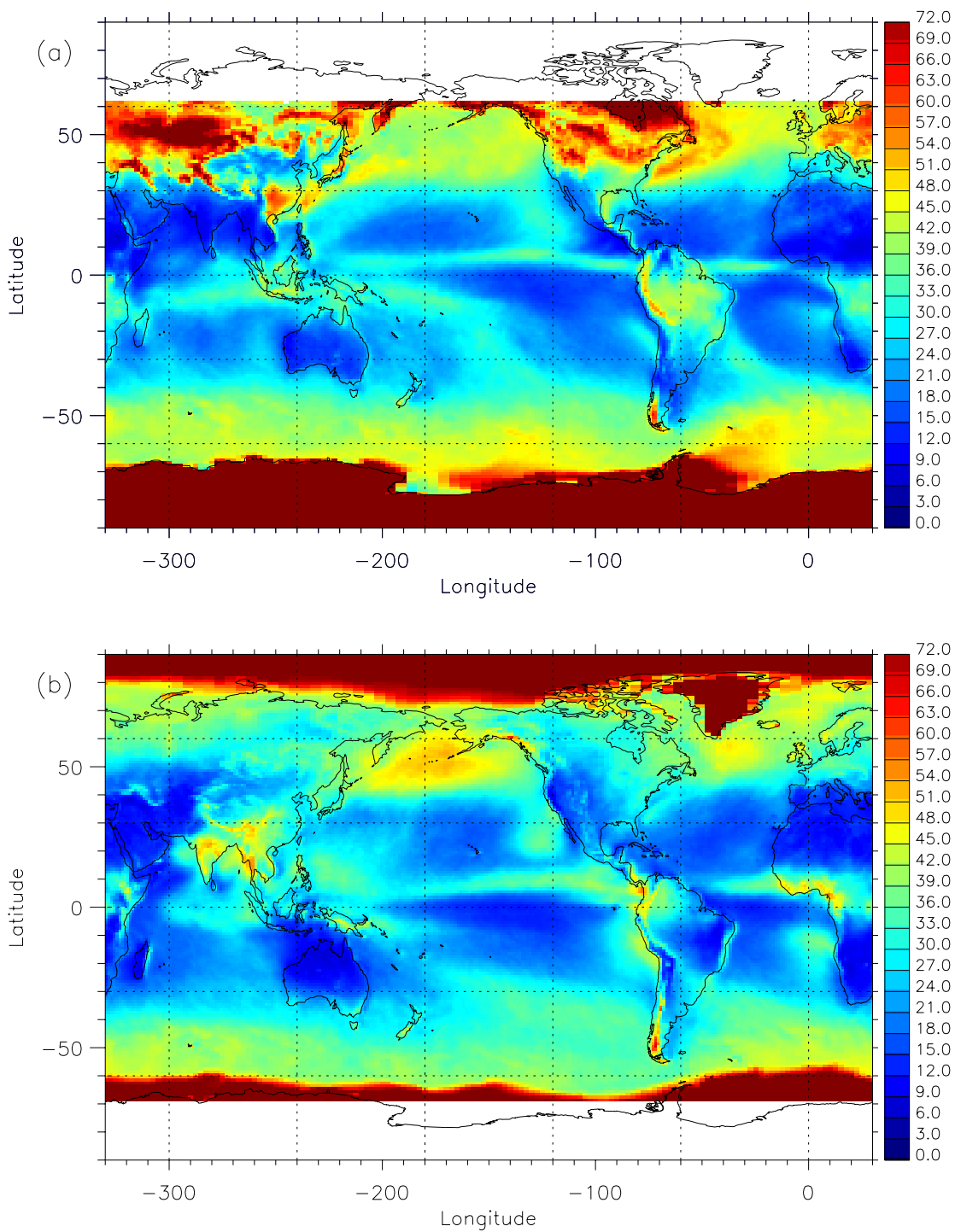


Figure 3.1 Climatological mean distribution of the TOMS reflectance for January (a) and July (b). The climatology is formed using data from 1979 to 1992.

3.3 Globally Averaged Reflectance

Suggestions of sunspot–climate correlations have a long history [*Herschel*, 1801]. In the last two decades there have been increasing numbers of reports on the possible links between solar variations and the climate [see reviews by *Wilcox*, 1975; *Tinsley and Deen*, 1991; *Tinsley*, 1997]. Recently, a large variation (3-4%) in the global cloud amount was found to highly correlate with the solar cycle [*Svensmark and Friis-Christensen* 1997]. This finding was used to imply a solar-terrestrial connection, where cosmic ray can vary the planetary albedo through its effect on global cloud cover [*Svensmark and Friis-Christensen*, 1997; *Tinsley*, 1997]. The 3-4% variation in the global cloud amount was suggested to alter the global albedo by more than 1% [*Svensmark and FriisChristensen*, 1997]. The dataset used in their work was the International Satellite Cloud Climatology Project (ISCCP) C2 cloudiness data [*Rossow and Schiffer*, 1991]. The re-calibrated ISCCP D2 data show a similar behavior [*Rossow and Schiffer*, 1999].

The interannual variations of the area-weighted averages of the TOMS reflectance between 60°S and 60°N are shown in Figure 3.2. We have formed the anomalies by removing the mean seasonal cycle (thin line), and a 12-month running mean was applied to highlight the low frequency variations (thick line). The domain 60°S - 60°N was used for a direct comparison with the previous work [*Svensmark and FriisChristensen*, 1997]. Global averages give essentially the same result. The effects from the 1982 El Chichon and 1991 Mount Pinatubo eruptions are clearly evident. On the other hand, there is no evidence of an increased reflectance at the 1986 cosmic ray maximum, where the global

cloud amount from the previous study peaks [Svensmark and FriisChristensen, 1997]. In fact, during the same period where the ISCCP global cloud amount was found to vary by 3-4%, in phase with the cosmic ray intensity (1984-1990), low frequency variations in the TOMS reflectance are remarkably small (< 0.2 RU).

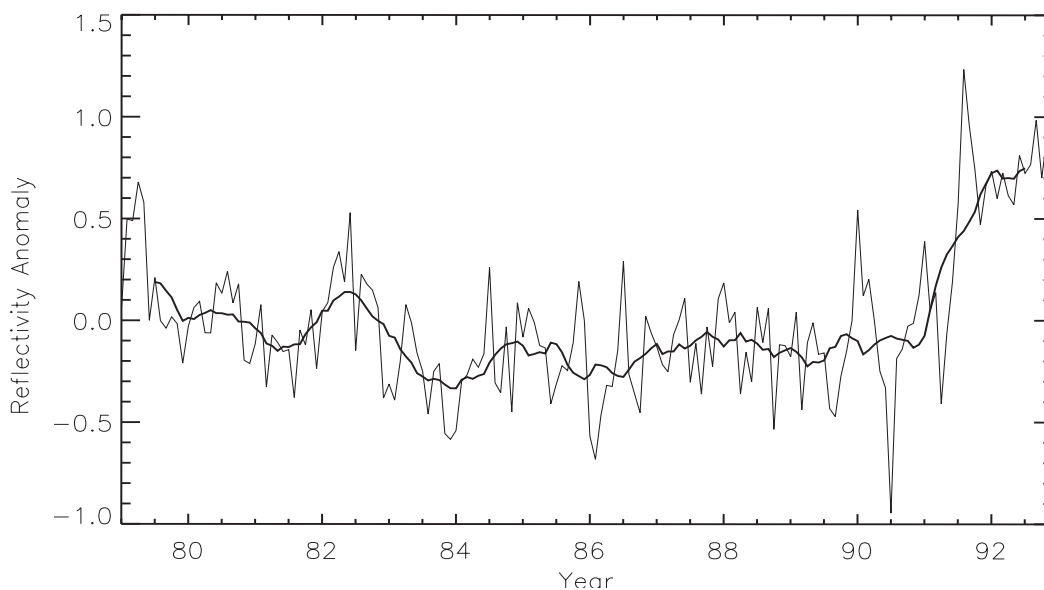


Figure 3.2 Interannual variations of the area-weighted averages of the TOMS reflectance between 60°S and 60°N. The unit is RU.

As discussed in section 3.2 and in Appendix, cloud variations in general have larger effects in the UV reflectance than in the visible. So, why the large variations in the ISCCP global cloudiness are not present in the reflectance measurements? *Kuang et al.* [1998] showed that variations in the globally averaged cloud optical depth in the ISCCP data is out of phase with those in the cloud amount. This appears to explain the small variation in the reflectance, while it is also possible that variations in both the cloud amount and the cloud optical depth result from imperfect calibration of the ISCCP data.

Our results add an interesting aspect to the debated cosmic ray - cloud – climate connection [*Jorgensen and Hansen, 2000*], *i.e.*, the originally suggested reflectance change from such a connection is absent [*Svensmark and FriisChristensen, 1997*], and the postulated connection must somehow account for the stability of the global reflectance. We note of course that from a statistical point of view, the postulated connection suffers from the shortness of the data records that were used as well.

3.4 Global Distributions of Interannual Reflectance

Variability

In this section, we shall present the global distributions of the interannual reflectance variability. The interannual variability in a grid box is defined as the standard deviation of the monthly anomalies. The interannual variability is shown for the December-February (DJF) (Figure 3.3 a) and June-August (JJA) (Figure 3.3 b).

The large variability over the DJF NH continents is mostly related to variations in the snow cover. The variations over the N. America can be related to the Pacific North Atlantic (PNA)–like teleconnection patterns [*Gutzler and Rosen, 1992; Serreze et al., 1998*]. As this circulation pattern is associated with the strength of the ridge over N. America, it affects the intrusion of cold air mass from the north, and modifies the snow cover and reflectance over the N. America. The snow cover over the Eurasia has been linked to the North Atlantic Oscillation (NAO) and other teleconnection patterns through the effects of these circulation patterns on the air temperature and/or precipitation [*Clark*

et al., 1999]. In the Southern Hemisphere (SH), effects of snow cover are limited to the Andes Mountain during SH winter.

The large reflectance variations over Spain are not related to snow cover. Instead, they are related to cloud variations due to storm track shift, also related to the NAO [*Hurrell and VanLoon*, 1997]. During the positive phase of the NAO, the N. Atlantic storm track shifts north, and reduces the cloud cover over the Mediterranean area. Southeast China also has substantial interannual reflectance variations during DJF. The wintertime Southeast China is characterized by mid-tropospheric subsidence forced by convection over Indonesian (the winter East Asian monsoon). This subsidence is unfavorable for cyclogenesis [*Chen et al.*, 1991], but leads to the common stratus clouds over wintertime Southeast China, which is mostly responsible for its relatively high mean reflectance (~55RU). The interannual reflectance variations in this region are presumably associated with variations in the winter East Asia monsoon. The monsoon is, in turn, strongly modulated by the El Nino Southern Oscillation (ENSO) — related variations in the strength of convection over Indonesia [*Wang et al.*, 2000].

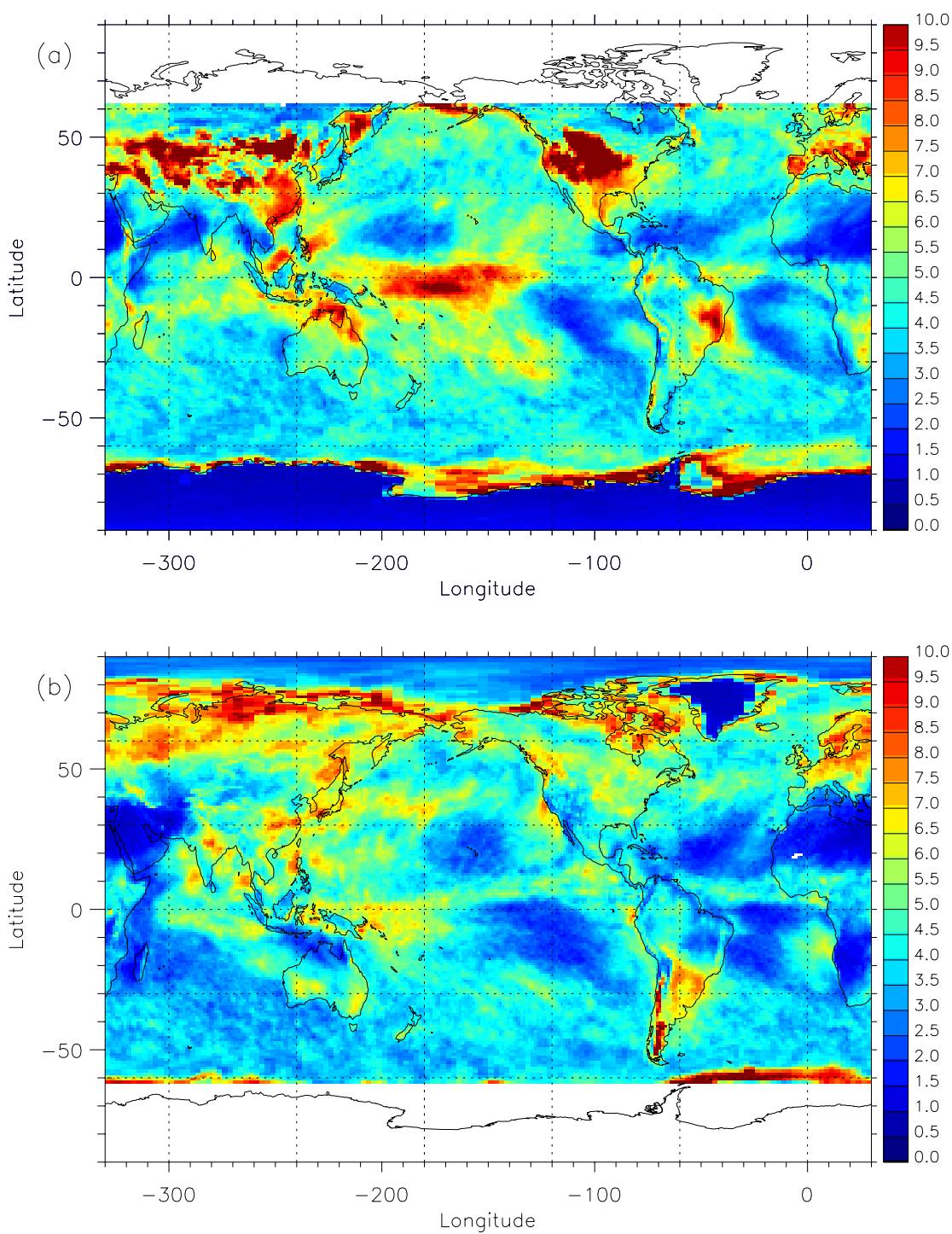


Figure 3.3 Interannual reflectance variability for DJF (a) and JJA (b).

Large reflectance variability over the ocean is associated with the rearrangement of convection by ENSO (low latitudes) and sea ice variations (high latitudes). The reflectance effect of sea ice variations will be discussed in more detail in Chapter 4. The effect of ENSO on the clouds and the reflectance is relatively well understood [Fu *et al.*, 1996]. During El Nino years, the tropical convection region that normally resides in the western equatorial pacific moves eastward, causing a corresponding shift in the reflectance.

Low variability is naturally found over the desert areas (both continental and maritime) and over the permanent ice shelves like the Greenland and the Antarctic continents. Quite low variability is also found over the midlatitude Southern Oceans, where the mean reflectance is 40-50 RU, owing to the storm track and the associated cloud fields. The variability over the midlatitude northern oceans is higher. In particular, the JJA variability has a banded maximum at about 40°N in N. Pacific. This coincides with the climatological mean sea surface temperature (SST) gradient. The reflectance variations over the midlatitude northern oceans will be examined in more detail in Chapter 5.

3.5 Summary

In this chapter, we have introduced the Nimbus-7 TOMS reflectance measurements as a useful dataset for interannual reflectance variation studies. We have also presented an overview of the interannual variability of the Earth's reflectance. In particular, variations in the globally averaged reflectance have been used to examine the postulated cosmic ray – cloud – climate connection.

3.6 Appendix

The purpose of this appendix is to compare the TOMS UV reflectance data and the ERBE visible albedo data. The ERBE data that we shall use include the combined data from scanner and non-scanner measurements (hereafter ERBE_SC), and the wide field of view (WFOV) non-scanner data (hereafter ERBE_NS).

The ERBE_SC data is available from November 1984 to February 1990, and is provided on a 2.5° longitude \times 2.5° latitude grid. This dataset combines the scanner and non-scanner measurements from a suite of satellites, and will be used as the “truth,” to which the other datasets will be compared. Both the TOMS reflectance and the ERBE_SC data are averaged into a $5^\circ \times 5^\circ$ grid. This grid size was chosen so that no interpolation was needed for either dataset. Figure 3.4 compares the observed mean seasonal cycles for a N. Pacific grid, 175° - 170° W, 50° - 55° N (a) and a S. Pacific 175° - 170° W, 45° - 50° S (b) grid. The mean seasonal cycles were formed using the data from February 1985 to January 1989. While there are significant year-to-year variations in both the visible albedo and the UV reflectance that are not captured in the mean seasonal cycles, the ratios between the two for the 4 years consistently show a seasonal variation that maximizes in the winter of each site (c). This seasonal variation is associated with the seasonally varying SZA, instead of real cloud changes. The TOMS reflectance, with a much weaker dependence on the SZA, therefore, can be used to better compare the cloud fields of the different seasons.

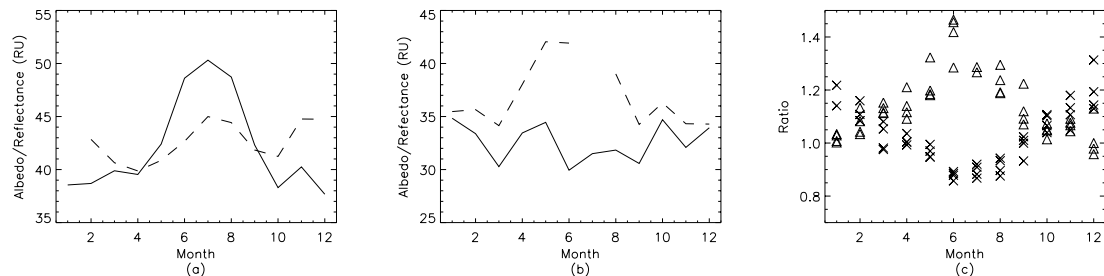


Figure 3.4 Comparison between the mean seasonal cycles in the TOMS reflectance (solid) and the ERBE_SC visible albedo (dashed) over a N. Pacific (a) and a S. Pacific site (b). The mean ERBE_SC albedo in January over the N. Pacific site and in July value the S. Pacific site are not reported as there are 2 years (out of 4) with missing data. The visible albedo to UV reflectance ratios for the individual months are shown in (c) for January (\times) and July (Δ).

Aside from this seasonal effect at mid-high latitudes, variations in the UV and visible reflectance are closely related. In particular, over open oceans without sea ice, cloud variations are by far the largest contributor to reflectance variations. As the cloud droplets/particles are Mie scatterers at UV and visible wavelengths, they have similar effects in the UV and visible. Figure 3.5 shows the correlation between the monthly anomalies of the TOMS reflectance and the ERBE_SC visible albedo (a) and the regression coefficients (b) for their coexisting 64 months (November 1984–February 1990). The mean seasonal cycles from February 1985–January 1989 are removed from the monthly data to form the monthly anomalies. For the ERBE data, we used only months with at least 20 days of good daily data.

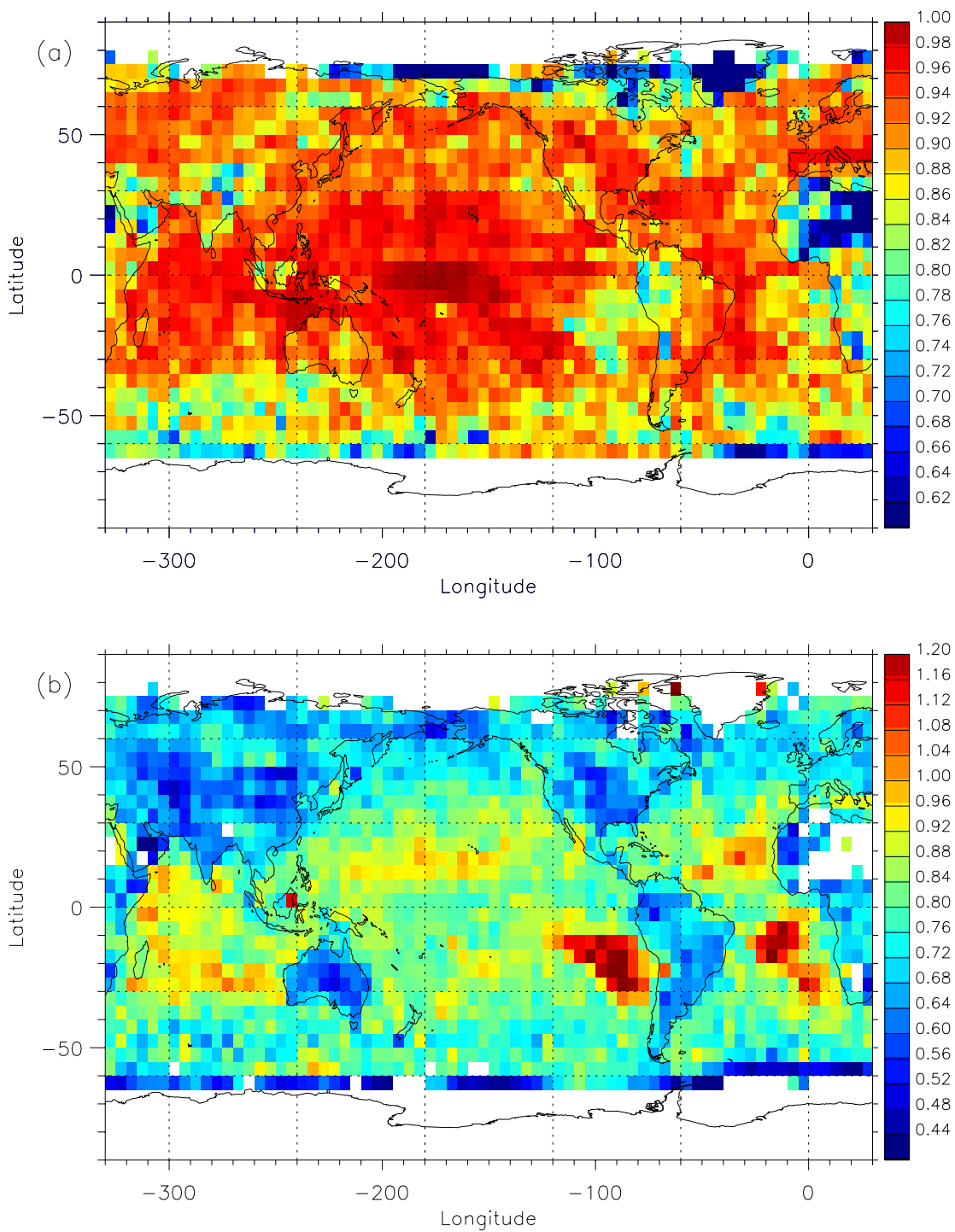


Figure 3.5 Correlation (a) and regress (b) coefficients between monthly ERBE visible albedo and TOMS UV reflectance anomalies.

The correlation between the two measurements is ~ 0.9 over most of the globe except where the variations are small. The regression coefficients are lower (*i.e.*, variations in the visible albedo is smaller) at higher latitudes and over land, associated with stronger attenuation by the atmosphere and the higher land albedo in the visible. The high regression coefficients off the Peruvian and Namibian coasts are likely a consequence of the pronounced year-round diurnal cycle observed in the dominant stratocumulus clouds in these regions [Rozendaal *et al.*, 1995]. These clouds tend to reach their maximum before sunrise and their minimum around noon due to the dissipation by in-cloud solar heating. The local noon TOMS measurements thus capture smaller variations than the ERBE measurements which precess through all local time over roughly a month. Weaker and less persistent diurnal cycles were observed over other eastern subtropical ocean regions [Rozendaal *et al.*, 1995], which may be responsible for the slightly higher regression coefficients there as well. The correlation over the southern oceans is relative low. This is presumably a combined effect of a smaller interannual variance and the seasonally varying TOMS reflectance to ERBE albedo ratio.

As we mentioned earlier, the ERBE non-scanner also provided a relatively long-term record of albedo measurements for low latitudes. Figure 3.6 compares the albedo in the ERBE_NS, ERBE_SC datasets and the TOMS reflectance for their overlapping 64 months for a tropical (175° - 170° W, 0° - 5° S) and a subtropical (85° - 90° W, 15° - 20° S) site. Over both sites, the TOMS reflectance is correlated to the ERBE_SC albedo variations better than the ERBE_NS albedo. The correlation coefficients between TOMS and ERBE_SC are 0.99, and 0.9 for the tropical and the subtropical sites, respectively. The

corresponding values between ERBE_NS and ERBE_SC are 0.9 and 0.81. This is true for almost all regions. We note that the subtropical site has a strong diurnal cloud cycle, and is where the sampling issue of TOMS is expected to be most severe. We therefore conclude that the TOMS reflectance is more suitable for interannual reflectance variations than the ERBE_NS data for low latitude studies as well.

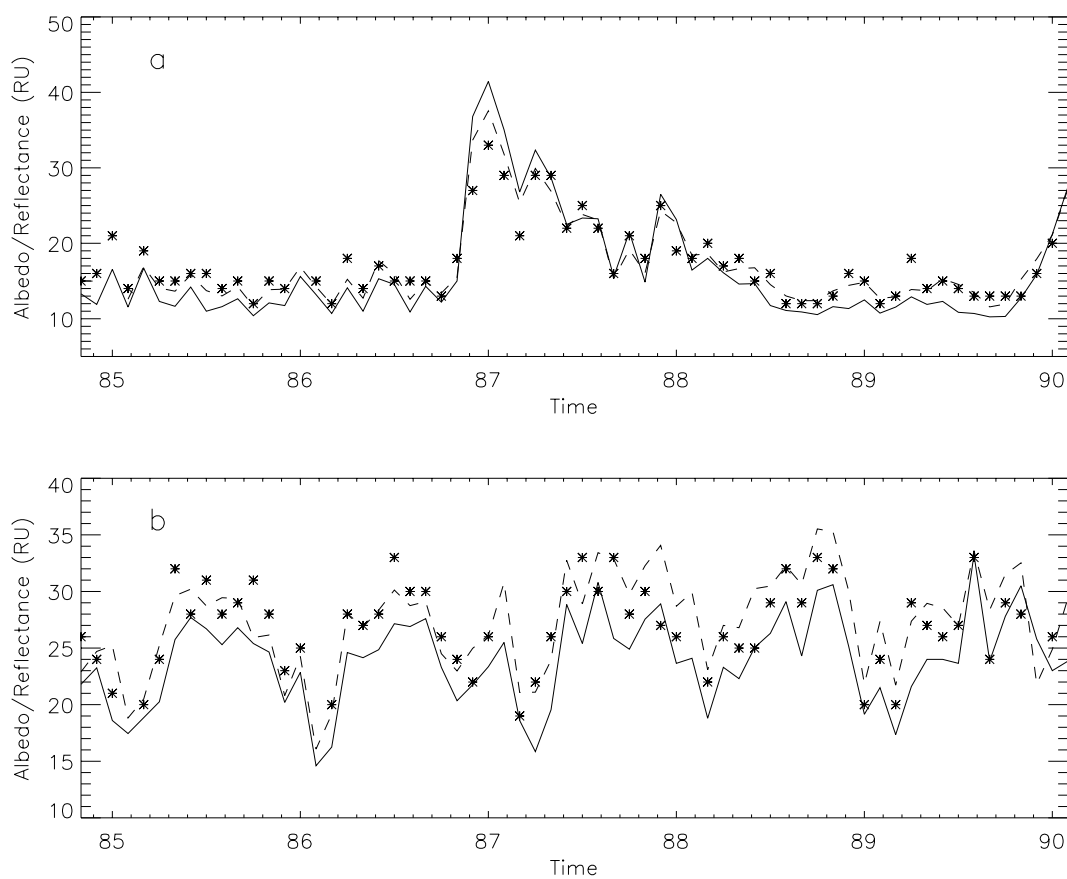


Figure 3.6 Comparison between monthly ERBE visible albedo and TOMS UV reflectance (dashed) over a tropical (a) and a subtropical (b) site. Data from ERBE_SC are shown by the solid line, and data from ERBE_NS are shown by the star symbol.

3.7 References

- Barkstrom, B.R., The Earth Radiation Budget Experiment (ERBE), *Bulletin of the American Meteorological Society*, 65 (11), 1170-1185, 1984.
- Bess, T. D., G. L. Smith, K. A. Bush, and D. A. Rutan, Intercomparison of ScaRab and ERBS monthly mean radiation fluxes. Preprints of the 10th Conference on atmospheric radiation, Madison, Wisconsin, American Meteorological Society, 60-63, 1999.
- Brest, C.L., W.B. Rossow, and M.D. Roiter, Update of radiance calibrations for ISCCP, *Journal of Atmospheric and Oceanic Technology*, 14 (5), 1091-1109, 1997.
- Budyko, M.I., The effect of solar radiation variations on the climate of the earth, *Tellus*, 21, 611 - 619, 1969.
- Chen, S.J., Y.H. Kuo, P.Z. Zhang, and Q.F. Bai, Synoptic climatology of cyclogenesis over East-Asia, 1958-1987, *Monthly Weather Review*, 119 (6), 1407-1418, 1991.
- Clark, M.P., M.C. Serreze, and D.A. Robinson, Atmospheric controls on Eurasian snow extent, *International Journal of Climatology*, 19 (1), 27-40, 1999.
- Dave, J.V., Effect of Aerosols on estimation of total ozone in an atmospheric column from measurements of its ultraviolet radiance, *Journal of the Atmospheric Sciences*, 35 (5), 809-911, 1978.
- Fu, R., W.T. Liu, and R.E. Dickinson, Response of tropical clouds to the interannual variation of sea surface temperature, *Journal of Climate*, 9 (3), 616-634, 1996.
- Gutzler, D.S., and R.D. Rosen, Interannual variability of wintertime snow cover across the Northern-Hemisphere, *Journal of Climate*, 5 (12), 1441-1447, 1992.

-
- Herman, J.R., E. Celarier, and D. Larko, UV 380 nm reflectance of the Earth's surface, clouds and aerosols, *Journal of Geophysical Research-Atmospheres*, 106 (D6), 5335-5351, 2001a.
- Herman, J.R., and E.A. Celarier, Earth surface reflectance climatology at 340-380 nm from TOMS data, *Journal of Geophysical Research-Atmospheres*, 102 (D23), 28003-28011, 1997.
- Herman, J.R., D. Larko, E. Celarier, and J. Ziemke, Changes in the Earth's UV reflectance from the surface, clouds, and aerosols, *Journal of Geophysical Research-Atmospheres*, 106 (D6), 5353-5368, 2001b.
- Herschel, W., Observation tending to investigate the nature of the sun, *Philos. Trans. R. Soc. (London)*, **Part 1**, 265-318, 1801.
- Hurrell, J.W., and H. VanLoon, Decadal variations in climate associated with the north Atlantic oscillation, *Climatic Change*, 36 (3-4), 301-326, 1997.
- Jorgensen, T.S., and A.W. Hansen, Comments on "Variation of cosmic ray flux and global cloud coverage - a missing link in solar-climate relationships" by Henrik Svensmark and Eigil Friis-Christensen *Journal of Atmospheric and Solar-Terrestrial Physics* 59 (1997) 1225-1232, *Journal of Atmospheric and Solar-Terrestrial Physics*, 62 (1), 73-77, 2000.
- Klein, S.A., and D.L. Hartmann, The Seasonal Cycle of Low Stratiform Clouds, *Journal of Climate*, 6 (8), 1587-1606, 1993.
- Kuang, Z.M., Y.B. Jiang, and Y.L. Yung, Cloud optical thickness variations during 1983-1991: Solar cycle or ENSO? *Geophysical Research Letters*, 25 (9), 1415-1417, 1998.

-
- Pubu, C., and Z.Q. Li, Anisotropic reflection of UV radiation at the top of the atmosphere: Characteristics and models obtained from Meteor 3/TOMS, *Journal of Geophysical Research-Atmospheres*, 106 (D5), 4741-4755, 2001.
- Rossow, W.B., and R.A. Schiffer, Isccp Cloud Data Products, *Bulletin of the American Meteorological Society*, 72 (1), 2-20, 1991.
- Rossow, W.B., and R.A. Schiffer, Advances in understanding clouds from ISCCP, *Bulletin of the American Meteorological Society*, 80 (11), 2261-2287, 1999.
- Rozendaal, M.A., C.B. Leovy, and S.A. Klein, An Observational Study of Diurnal-Variations of Marine Stratiform Cloud, *Journal of Climate*, 8 (7), 1795-1809, 1995.
- Serreze, M.C., M.P. Clark, D.L. McGinnis, and D.A. Robinson, Characteristics of snowfall over the eastern half of the United States and relationships with principal modes of low-frequency atmospheric variability, *Journal of Climate*, 11 (2), 234-250, 1998.
- Svensmark, H., Influence of cosmic rays on Earth's climate, *Physical Review Letters*, 81 (22), 5027-5030, 1998.
- Svensmark, H., and E. FriisChristensen, Variation of cosmic ray flux and global cloud coverage - A missing link in solar-climate relationships, *Journal of Atmospheric and Solar-Terrestrial Physics*, 59 (11), 1225-1232, 1997.
- Tinsley, B. A., Do effects of global atmospheric electricity on clouds causes climate changes? *EOS*, 78, 341, 1997.
- Tinsley, B.A., and G.W. Deen, Apparent Tropospheric Response to Mev-Gev Particle-Flux Variations - a Connection Via Electrofreezing of Supercooled Water in High-Level Clouds, *Journal of Geophysical Research-Atmospheres*, 96 (D12), 22283-22296, 1991.

Wang, B., R.G. Wu, and X.H. Fu, Pacific-East Asian teleconnection: how does ENSO affect East Asian climate? *Journal of Climate*, 13 (9), 1517-1536, 2000.

Wielicki, B.A., T.M. Wong, R.P. Allan, A. Slingo, J.T. Kiehl, B.J. Soden, C.T. Gordon, A.J. Miller, S.K. Yang, D.A. Randall, F. Robertson, J. Susskind, and H. Jacobowitz, Evidence for large decadal variability in the tropical mean radiative energy budget, *Science*, 295 (5556), 841-844, 2002.

Wilcox, J. M., Solar activity and the weather, *J. Atmos. Terr. Phys.*, **37**, 237-256, 1975.

Chapter 4: Observed Effects of Interannual Summertime Sea Ice Variations on the Polar Reflectance

Zhiming Kuang, Xianglei Huang, Yuk L. Yung

Division of Geological and Planetary Sciences, California Institute of
Technology, Pasadena, CA

4.1 Abstract

Using the Total Ozone Mapping Spectrometer (TOMS) measurements, we show that ultraviolet Lambertian equivalent reflectance (UV LER) variations of the polar icy areas are well correlated with the microwave-derived sea ice concentration variations on interannual timescales. The effect of interannual sea ice variations on the UV LER appears to have a hemispheric asymmetry: a 1% change in the sea ice concentration is related to a larger UV LER change in the Antarctic ($0.59 \pm 0.09\%$) than in the Arctic icy areas ($0.35 \pm 0.05\%$). This result is extended to the top of the atmosphere (TOA) broadband visible albedo by relating the UV LER to the TOA albedo. The observed asymmetry is absent in a general circulation model that we have examined.

4.2 Introduction

Monitoring of the polar regions is of considerable interest to the detection of global warming because of the expected sensitivity of these regions to climate change. Recent studies using satellite microwave data and submarine sonar sounding data revealed significant polar sea ice changes over the past few decades [Cavalieri *et al.*, 1997; Rothrock *et al.*, 1999]. The thinning and shrinking Arctic sea ice, in particular, has been suggested as an early signal of global warming [Vinnikov *et al.*, 1999].

The sea ice is also well known for its roles in various feedbacks in the climate system. The sea ice-albedo feedback, being perhaps the best known example, has long been recognized as an important mechanism that increases the climate sensitivity [Budyko, 1969]. The strength of this feedback strongly affects the modeled amplitude of the global warming [Rind *et al.*, 1995]. Besides the dependence on complex interactions in the ice pack [Curry *et al.*, 1995], strength of the sea ice-albedo feedback is also modulated by clouds, which can shield sea ice related surface albedo changes, thus reducing their effects. The magnitude of this shielding effect has, however, considerable uncertainties, owing to the inadequate cloud observations in the polar regions and the parameterization uncertainties of these clouds in the models [Ingram *et al.*, 1989].

In this paper, we examine the ultraviolet Lambertian equivalent reflectance (hereafter, UV LER) changes over the polar icy areas during the past two decades and quantify the effect of sea ice changes on the UV LER. The UV LER is essentially derived by removing the Rayleigh scattering contributions from the measured top of the atmosphere

(TOA) UV reflectance, thus including effects from both the surface and the clouds. We then extend the estimate to the TOA energy budget by relating the UV LER to the TOA broadband visible albedo. A brief comparison with general circulation model (GCM) results is presented.

4.3 Data and Methods

The UV LER changes are derived from the Total Ozone Mapping Spectrometer (TOMS) reflectance measurements at an ultraviolet (UV) ozone non-absorbing wavelengths (380 nm), as described in some details in Chapter 3. In short, the Nimbus-7 TOMS version-7 monthly reflectance that we use is available from November 1978 to April 1993, and is provided at a 1.25° longitude \times 1° latitude grid. The instrument calibration has been maintained within 0.2% (or RU) per decade [*Herman and Celarier, 1997; Herman et al., 1991*]. For discussions in this chapter, reflectance will be expressed in percent, as for the sea ice concentration, instead of RU, which is used in Chapters 3 and 5.

The sea ice concentration data that we use were derived from the Nimbus-7 Scanning Multichannel Microwave Radiometer (SMMR) and the Defense Meteorological Satellite Program's (DMSP) DMSP-F8, -F11 and -F13, Special Sensor Microwave/Imager (SSM/I) using a modified version of the Bootstrap Algorithm [*Comiso, 1999*]. Daily and monthly data from 1979 through 2000 were obtained from the National Snow and Ice Data Center Distributed Active Archive Center (NSIDC DAAC), University of Colorado at Boulder, in a 25 km resolution with a polar stereographic projection. To compare with the reflectance data, we have re-gridded the sea ice data into the TOMS grid.

We study the interannual variations in the area-averaged UV LER over the icy regions for the months when the sun is at least 10° above the horizon (April to August for the Arctic, and October to February for the Antarctic). The icy area is defined as the region where the maximum sea ice concentration over the past two decades is greater than 5% (gray area in Figure 4.1). It covers about 17×10^6 km² over the North Pole and about 25×10^6 km² in the south. This definition effectively excludes broad areas particularly in the northern oceans that make little contribution to the sea ice changes, and reduces variations unrelated to the sea ice changes. We then calculate the area-averaged mean summertime UV LER over the polar icy areas from 1979 to 1991. The interannual variability is defined as the standard deviation of the summertime mean UV LER. Data after 1991 were not used for this part of the analysis due to significant effects from the Mount Pinatubo eruption. Months with significant gaps in either dataset have been excluded from the analysis. This includes October 1978, June 1979, August 1984, December 1987 and January 1988.

The Nimbus-7 TOMS monthly record continues to April 1993, and is extended to the end of 1994 by the Meteor-3 TOMS. The TOMS team has normalized the Meteor-3 calibration to bring the two instruments into absolute agreement during their overlap period (about 20 months), yet residual inter-calibration errors as high as 1% may still exist for the northern high latitudes, as a consequence of the latitudinal dependence of the Meteor-3 and Nimbus-7 normalization [Seftor *et al.*, 1997]. The calibration problem, together with the Mount Pinatubo eruption, complicates the interpretation of a time series derived from a simple averaging. However, this difficulty can be mitigated by comparing the region where interannual sea ice variation is large with the region where there has

been relatively little sea ice change. We have divided the polar icy area into a large sea ice variation region (interannual variability $> 7\%$, marked by dark gray in Figure 4.1) and a small sea ice variation region (interannual variability $< 7\%$, marked by light gray in Figure 4.1). The 7% threshold was chosen so that the two regions constitute nearly equal areas. The two areas also have similar statistics in terms of latitude and mean reflectance. As the calibration error and the volcanic aerosol effect mainly depend on the latitude and the reflectance, their contributions are effectively removed by subtracting the UV LER variations over the small sea ice variation area from the variations over the large sea ice variation area. This method is also applied to the Earth Probe (EP) TOMS data to extend the analysis to the year 2000. Continuous coverage is unfortunately not available due to a 2-year gap between EP TOMS and the Meteor-3 TOMS (December 1994–July, 1996).

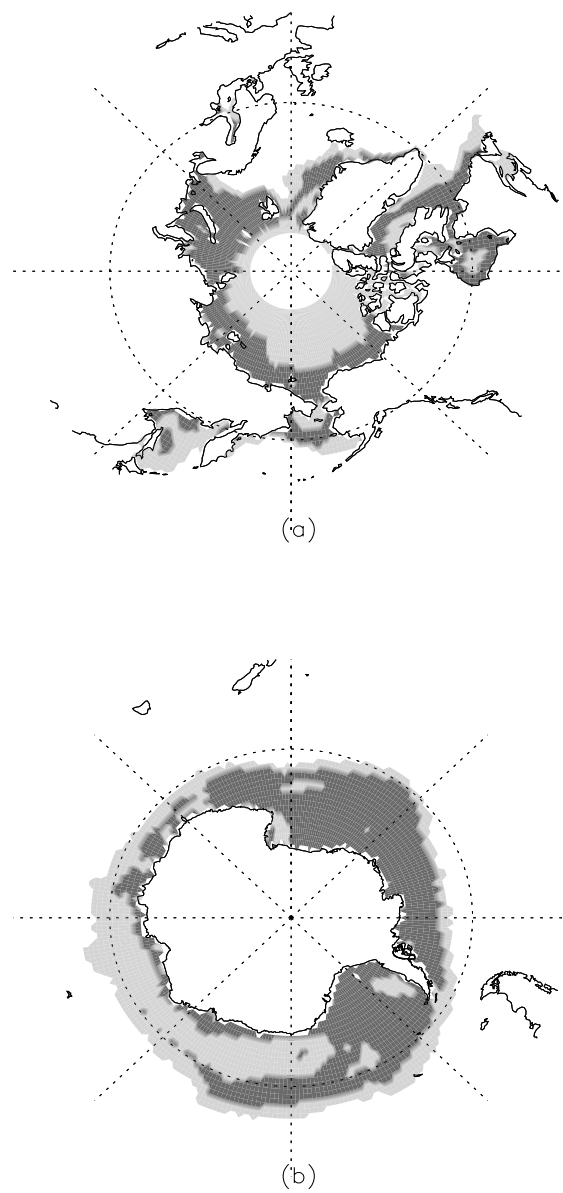


Figure 4.1 The Arctic (a) and Antarctic (b) icy areas are defined as the regions where the maximum sea ice concentration is greater than 5% over the 2 decades that we examine, and shown in grey (both light and dark). Dark grey shows the regions where interannual sea ice variability is greater than 7%.

4.4 Results

Figure 4.2 a shows the interannual variability in the Arctic summertime (April-August averages) UV LER (diamond) and the sea ice concentration (triangle). Comparison is made for the years 1979 to 1991, when the well-calibrated Nimbus-7 TOMS data were available and effects from Mount Pinatubo were absent. The effect of sea ice on the reflectance is clearly evident (correlation $r=0.81$). A change of 1% in the sea ice concentration is related to $0.39\pm 0.11\%$ change in the TOA UV LER by linear regression. The decreasing trend in the Arctic sea ice has been well documented [*Parkinson et al.*, 1999]. The independent TOMS data, showing a darkening Arctic, (the UV LER decreased by $1.1\pm 0.4\%$ per decade over the period 1979–1991), complement the microwave data in establishing the Arctic sea ice area decrease, especially as the microwave instruments change from the SMMR to the SSMI in 1987 [*Bjorgo et al.*, 1997]. Analysis using daily data of only the days that both measurements are available gives the same result.

The changes over the Antarctic icy area (Oct.-Feb. averages) are shown in Figure 4.2b. The data at year 1979 is the mean for the months from October 1978 – February 1979, and the same applies to other years. Although the Antarctic sea ice did not show significant secular trends, large interannual variations were clearly present and strongly changed the circumpolar reflectance. Using linear regression to derive the effect of sea ice on the UV LER is problematic given the lower correlation ($r=0.67$).

The effect of sea ice on the UV LER is further examined by subtracting the variations over the small sea ice variation area (marked by light gray in Figure 4.1) from the

variations over the large sea ice variation area (dark gray). This method effectively removed errors due to calibration and effects from variations that are rather uniform over the poles (*e.g.*, from the Mount Pinatubo eruption), and hence greatly improved the correlation between the sea ice and the UV LER variations (Figure 4.3). The correlation is 0.88 for both poles, as calculated from the years for which both types of data exist (20 years). Linear regression shows that 1% change in the sea ice concentration is related to a TOA UV reflectance change of $0.35 \pm 0.05\%$ and $0.59 \pm 0.09\%$ for the Arctic and the Antarctic, respectively. The values are consistent with those of Figure 4.2. The high correlations indicate that sea ice has the dominant effect on the interannual polar reflectance variations; cloud variations seem to have been averaged out on this timescale.

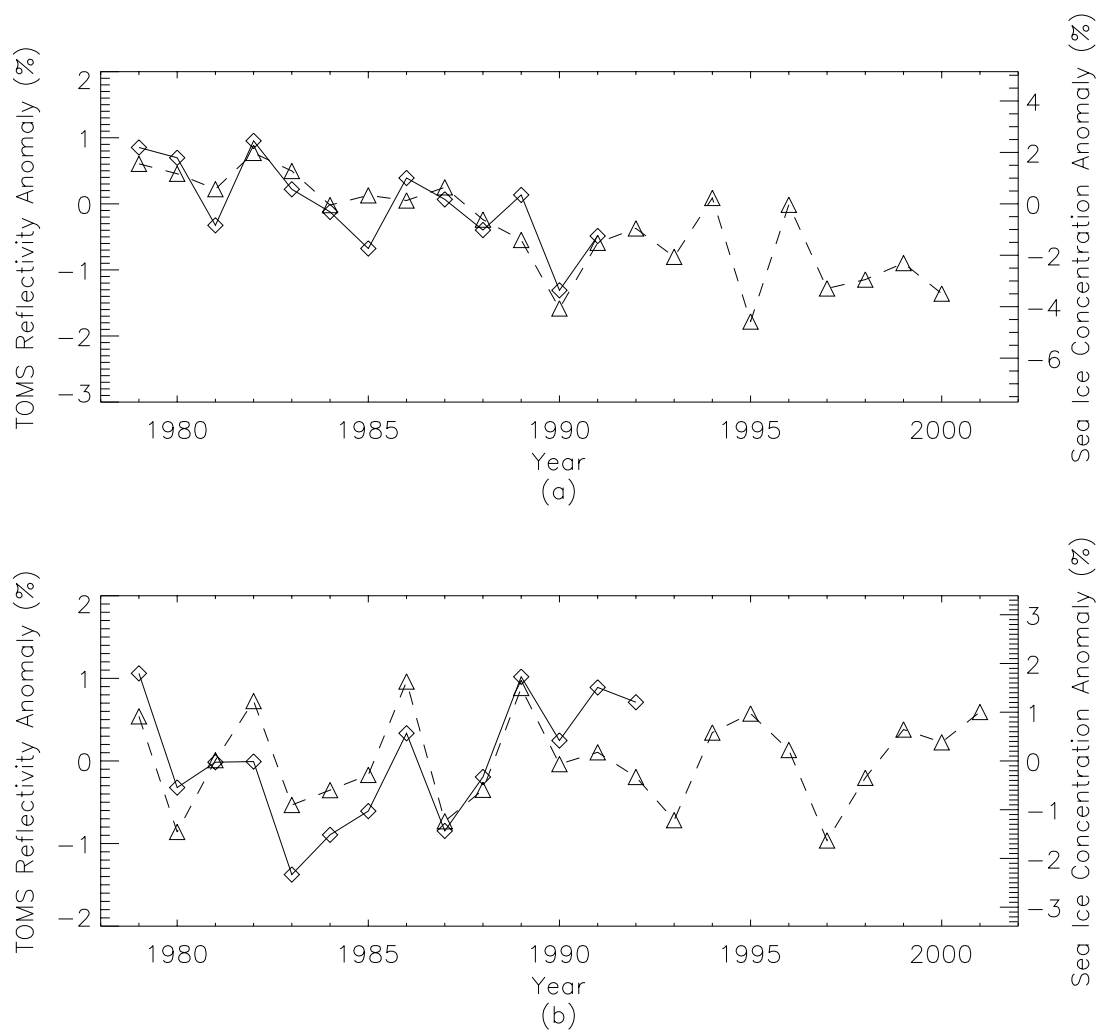


Figure 4.2 Summertime (April–August averages for the Arctic and October–February averages for the Antarctic) interannual variations of the UV LER (diamond) and the sea ice concentration (triangle) for the Arctic (a) and the Antarctic (b) icy areas.

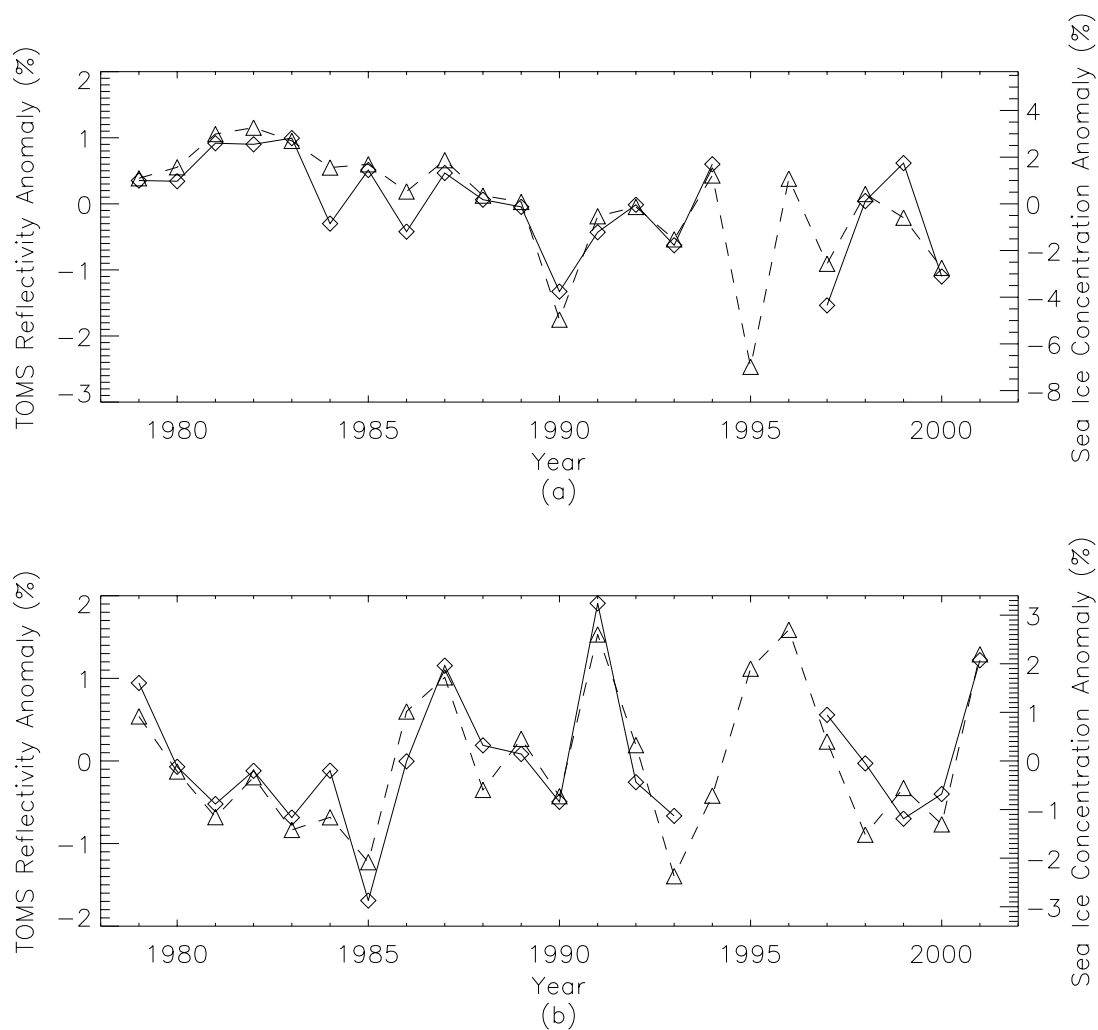


Figure 4.3 Differences in the summertime (April-August averages for the Arctic and October-February averages for the Antarctic) UV LER changes (diamond) and sea ice concentration changes (triangle) between the polar icy regions where the interannual sea ice variability is greater than 7% and the icy regions where the variability is less than 7%. The lines are formed by subtracting the changes in the low sea ice variability regions from the changes in the high sea ice variability regions. This approach effectively removes the interferences from the Mount Pinatubo eruption and the inter-calibration errors between the Nimbus-7 TOMS and the Meteor-3 TOMS, and is used to extend the regression study between sea ice changes and UV LER changes for additional years (1992-2000), as compared to Figure 4.2.

4.5 Discussion

Typical values of UV LER for optically thick cloud and for the open ocean are 0.90 and 0.05 for summertime ocean at mid-high latitudes [*Herman and Celarier, 1997*]. The value for sea ice is ~ 0.9 as seen in the TOMS daily maps of UV LER (this was estimated from the mean UV LER for the grids with sea ice concentrations greater than 95%). The effect of cloud shielding is evident for both poles. The averaged UV LER for the grids with little sea ice ($< 5\%$) is ~ 0.4 for the Arctic, and ~ 0.45 for the Antarctic icy area, as compared to the value of 0.05 for the clear sky open ocean.

The UV LER of sea ice in the Arctic, however, reaches a minimum for the months June and July. The value is ~ 0.75 when averaged over the entire Arctic icy area and can be as low as 0.65 when only the areas with large interannual variations (dark grey in Figure 4.1) are considered. This seasonal cycle is consistent with other sea ice surface albedo studies [*Curry et al., 2001*], and may be understood in terms of the extensive melt ponds over the summer Arctic. Such a large seasonal variation in the UV LER is absent for the Antarctic sea ice, as there are no melt ponds for the Antarctic sea ice. The generally darker Arctic sea ice in June and July may partially explain the smaller UV LER effect of sea ice changes over the Arctic. It is also possible that, on an interannual timescale, variations in the mean Arctic sea ice concentration may be influenced more by regions and months with less reflective sea ice or more prominent cloud shielding. More studies are needed to understand this asymmetry between the two poles.

We now try to extend our results on the UV LER to the TOA broadband visible albedo, using the following two approaches.

First, the relationship between UV LER change and broadband visible albedo change is investigated with an idealized situation, which is a superposition of (1) ice-free ocean under clear sky, (2) sea ice under clear sky, and (3) overcast cloud. Then the averaged visible albedo over this region is given by

$$R_{vis} = (1 - f_{ice} - f_{cld})r_{ocean} + f_{ice}r_{ice} + f_{cld}r_{cld} \quad (1)$$

where r_{ocean} , r_{ice} and r_{cld} are the TOA broadband visible albedo for three scenarios respectively and f_{ice} and f_{cld} are the fractional area of scenario (2) and (3), respectively. Using MODTRAN [Wang and Anderson, 1996] with sub-polar summer atmospheric profiles provided by the MODTRAN package, we calculate the TOA broadband (0.2-5 μ m) visible albedo for above scenarios at different solar zenith angles. For the scenario of overcast cloud, the calculated TOA broadband visible albedo is insensitive to the surface below cloud deck. We then average the albedo over 40-80° solar zenith angle, a range approximately appropriate to the summer time polar region at local noon time. In this way, we obtain $r_{ocean} \sim 0.10$, $r_{ice} \sim 0.59$, and $r_{cloud} \sim 0.70$ (to calculate r_{ice} , we have used the spectral albedo appropriate for the dry snow over sea ice scene [Schramm et al., 1997]). It follows that a 1% change in the cloud scene, keeping the fraction of the clear sky sea ice scene fixed, gives a 0.85% change in the UV LER and a 0.6% change in the TOA visible albedo. On the other hand, with a fixed fraction of cloud scene, a 1% change in the clear sky sea ice scene corresponds to a ~0.85% change in the UV LER and a 0.49% change in the TOA visible albedo. Thus, a 1% change in the UV LER corresponds to a larger change in the TOA visible albedo (0.7%) if the variation is caused by changes in the cloud scene than it does if the variation is due to changes in the sea ice scene (0.58%). Since the interannual variations in the UV LER is apparently due to sea ice

variations, the effect of 1% sea ice change on the TOA visible albedo (cloud shielding effect included) is estimated to be 0.20% for the Arctic and 0.34% for the Antarctic. On an interannual timescale, a unit change in the summertime sea ice concentration, therefore, has a greater impact on the TOA visible albedo over the Antarctic than the Arctic.

An empirical relation between the UV LER and the TOA visible albedo was also derived by comparing the TOMS data with the broadband Earth Radiation Budget Experiment (ERBE) TOA visible (0.2-5 μm) albedo data [Barkstrom, 1984]. The ERBE data are available from February 1985 to January 1989, and are provided at a 2.5° longitude \times 2.5° latitude grid. The data that we use have been modified by the National Center for Atmospheric Research (NCAR) [Hurrell and Campbell, 1992]. We obtained a linear relation of $\sim 0.7\%$, and $\sim 0.6\%$ visible albedo change per 1% UV LER change for the Arctic and the Antarctic icy regions, respectively (The ERBE albedo changes and the UV LER changes are linearly correlated with $r=0.89$ for the Arctic and 0.78 for the Antarctic.). Since these values are derived from reflectance and albedo variations associated with both sea ice and cloud variations, they should provide upper limits on how much TOA visible albedo variation is associated with a unit UV LER change when this change is mostly due to sea ice variations. The values are roughly consistent with our idealized calculations. We note that the estimate for the Antarctic is more uncertain due to the smaller linear correlation between the ERBE albedo and the UV LER over the Antarctic icy area.

The extension of our UV LER results to the visible is admittedly crude. Alternatively, one may use the AVHRR polar pathfinder data to directly examine the relation between

variations in the TOA visible albedo and those in the sea ice. A comprehensive analysis of the polar pathfinder data, however, is out of the scope of this work.

We have also examined the relation between sea ice changes and the TOA visible albedo in the outputs of a coarse resolution Geophysical Fluid Dynamics Laboratory coupled climate model simulation forced by increasing greenhouse gases and the direct effect of tropospheric sulfate aerosols [Dixon and Lanzante, 1999]. This model was used previously to project future sea ice changes [Vinnikov *et al.*, 1999]. We have examined the outputs for a 100 year period from their model epoch A, which corresponds to the years from 1966 to 2065. In the model results, the summertime TOA albedo is highly correlated with sea ice ($r=0.97$), with estimated sensitivity of $\sim 0.25\%$ and $\sim 0.27\%$ visible albedo change per 1% sea ice coverage change for the Arctic and the Antarctic, respectively. The asymmetry in the effect of sea ice changes between the two polar regions is absent in this model.

We note that values presented here are estimates for the current climatic conditions and should be used only to study moderate climate changes. Large climate changes may significantly affect, for example, the cloud field, and therefore change the strength of the albedo effects.

4.6 Conclusion

In this paper, we have examined UV LER changes over the polar icy areas during the past two decades. We show that the UV LER variations correlate well with those of the microwave-derived sea ice concentration on an interannual timescale. Since the

microwave data involved matching records from different instruments [Bjorgo *et al.*, 1997], our result provides independent confirmation on the record matching and should help alleviating concerns in this regard. The high correlations also indicate the dominant effect of sea ice on the interannual polar reflectance variations. We have quantified the effect of interannual sea ice changes on the UV LER, in which the shielding effect from clouds is apparent. Moreover, the effect of sea ice on the UV LER is significantly smaller in the Arctic than in the Antarctic. This result is extended to the TOA broadband visible albedo by relating the UV LER to the TOA albedo. The observed asymmetry is absent in a GCM. Determined from observations over the entire polar icy regions over a two decade period, these results should help the quantification of sea ice-albedo feedback under the current climatic conditions.

4.7 Acknowledgements

We thank K. Dixon for providing the GFDL model outputs, Y. Chao and M. Gerstell for useful comments. This research was supported by NASA grants NAG5-7230 and NAG5-7680

4.8 References

- Barkstrom, B. R., The earth radiation budget experiment (ERBE), *Bull. Amer. Meteor. Soc.*, 65, (11), 1170-1185, 1984.
- Bjorgo, E., O. M. Johannessen, and M. W. Miles, Analysis of merged SMMR-SSM/I time series of Arctic and Antarctic sea ice parameters 1978-1995, *Geophys. Res. Lett.*, 24, (4), 413-416, 1997.
- Budyko, M. I., The effect of solar radiation variations on the climate of the earth, *Tellus*, 21, 611-619, 1969.
- Cavalieri, D. J., P. Gloersen, C. L. Parkinson, J. C. Comiso, and H. J. Zwally, Observed hemispheric asymmetry in global sea ice changes, *Science*, 278, (5340), 1104-1106, 1997.
- Comiso, J. Bootstrap sea ice concentrations for NIMBUS-7 SMMR and DMSP SSM/I. Boulder, CO, USA: National Snow and Ice Data Center. Digital media, 1999, updated 2002, available at <http://nsidc.org/data/nsidc-0079.html>.
- Curry, J. A., J. L. Schramm, and E. E. Ebert, Sea-ice albedo climate feedback mechanism, *J. of Climate*, 8, (2), 240 -247, 1995.
- Dixon, K. W. and J. R. Lanzante, Global mean surface air temperature and North Atlantic overturning in a suite of coupled GCM climate change experiments, *Geophys. Res. Lett.*, 26, 1885-1888, 1999.
- Herman, J. R., and E. Celarier, Earth surface reflectance climatology at 340-380 nm from TOMS data, *J. Geophys. Res.-Atmosphere*, 102, (D23), 28003-28011, 1997.
- Herman, J. R., R. Hudson, R. McPeters, R. Stolarski, Z. Ahmad, X.Y. Gu, S. Taylor, and C. Wellemeyer, A new self-calibration method applied to TOMS and SBUV backscattering ultraviolet data to determine long-term global ozone change, *J. Geophys. Res.-Atmosphere*, 96, (D4), 7531-7545, 1991.

-
- Hurrell, J.W., and G.G. Campbell, Monthly mean global satellite data sets available in CCM history tape format, pp. 94, NCAR, Boulder, CO, 1992.
- Ingram, W.J., C.A. Wilson, and J.F.B. Mitchell, Modeling climate change-an assessment of sea ice and surface albedo feedbacks, *J. Geophys. Res.-Atmosphere*, 94, (D6), 8609-8622, 1989.
- Parkinson, C.L., D.J. Cavalieri, P. Gloersen, H.J. Zwally, and J.C. Comiso, Arctic sea ice extents, areas, and trends, 1978 -1996, *J. Geophys. Res.-Oceans*, 104, (C9), 20837-20856, 1999.
- Rind, D., R. Healy, and C.L. Parkinson, The role of sea-ice in $2\times\text{CO}_2$ climate model sensitivity. 1. The total influence of sea-ice thickness and extent, *J. of Climate*, 8, (3), 449-463, 1995.
- Rothrock, D.A., Y. Yu, and G.A. Maykut, Thinning of the Arctic sea-ice cover, *Geophys. Res. Lett.*, 26, (23), 3469-3472, 1999.
- Schramm, J. L., M. M. Holland, J. A. Curry, Modeling the thermodynamics of a sea ice thickness distribution, 1, Sensitivity to ice thickness resolution, *J. Geophys. Res.*, 102, 23079-23091, 1997.
- Seftor, C.J., G. Jaross, J.R. Herman, X. Gu, L. Moy, S.L. Taylor, and C.G. Wellemeyer, The Meteor 3 total ozone mapping spectrometer version 7 data set: Calibration and analysis, *J. Geophys. Res.-Atmosphere*, 102, (D15), 19247-19256, 1997.
- Vinnikov, K.Y., A. Robock, R.J. Stouffer, J.E. Walsh, C.L. Parkinson, D.J. Cavalieri, J.F.B. Mitchell, D. Garrett, and V.F. Zakharov, Global warming and Northern Hemisphere sea ice extent, *Science*, 286, (5446), 1934-1937, 1999.
- Wang, J., and G.P. Anderson, Validation of FASCOD3 and MODTRAN3: Comparison of Model Calculations with Interferometer Observations from SPECTRE and ITRA, *Applied Optics*, 35, 6028-6040, 1996.

Chapter 5: Interannual Reflectance Variations over the North Pacific and North Atlantic

5.1 Abstract

We investigate the interannual reflectance variations over the N. Pacific and the N. Atlantic using the Total Ozone Mapping Spectrometer (TOMS) reflectance data from 1979 to 1992. The leading patterns of the reflectance variations over the N. Atlantic and N. Pacific are related to variations in the storm tracks, and to the corresponding North Atlantic Oscillation (NAO) and Pacific North American (PNA) circulation patterns. Reflectance variations over the N. Pacific during the non-summer seasons, however, also have a substantial component that is linked to PNA related variations in the lower tropospheric stability, through the effect of stability on boundary layer clouds. The effect of stability variations on the reflectance, however, appears to saturate when the static stability becomes sufficiently large. This would limit the efficiency of the proposed summertime stability-boundary layer cloud feedback. We have also found a negative local correspondence between summertime reflectance and sea surface temperature (SST) anomalies. However, the reflectance anomalies are largely attributed to variations in the frontal clouds, instead of the marine boundary layer stratiform clouds (MSC). This result argues against the proposed feedback between summertime SST and MSCs.

5.2 Introduction

The importance of clouds in the Earth's weather and climate is universally recognized. While existing observational and theoretical studies have acquired a wealth of information on the different cloud processes and their interaction with the weather systems (for a summary, see, *e.g.*, *Houze* [1993]), incorporating this information into climate studies (*e.g.*, through parameterizations) proves difficult. Current general circulation models (GCMs), a major tool in climate research, are not yet capable of simulating cloud processes and cloud-related feedbacks correctly, as highlighted by the inconsistency among the GCMs [*Alekseev et al.*, 1996; *Cess et al.*, 1989]. It is therefore of interest to undertake observational studies on cloud variations and their relationships with meteorological conditions on spatial and temporal scales that are more closely related to climate processes.

The low stratiform clouds prevalent over midlatitude and eastern subtropical oceans, in particular, have received much attention. These clouds, being low and highly reflective, have a great impact on the Earth's radiation budget [*Hartmann et al.*, 1992]. Using surface cloud observations, significant relationships have been identified between the low stratiform cloudiness and variables such as the lower tropospheric static stability, the sea surface temperature (SST), among many others [*Hanson*, 1991; *Klein and Hartmann*, 1993; *Klein et al.*, 1995; *Norris and Leovy*, 1994; *Norris et al.*, 1998]. Because of the large radiative effect of these low stratiform clouds, various feedbacks have been suggested based on the observed relationships [*Klein and Hartmann*, 1993; *Miller*, 1997;

Norris and Leovy, 1994; Norris et al., 1998; Philander et al., 1996]. These feedbacks may have contributed to many important features of the climate system, such as the persistence of midlatitude SST anomalies [*Norris et al., 1998*], stability of the tropical climate [*Miller, 1997*], and the position of the inter-tropical convergence zone [*Philander et al., 1996*]. Some may also enhance the climate sensitivity to future changes. For instance, *Klein and Hartmann [1993]* found that the seasonal variations of the low stratiform clouds are linearly related to the lower troposphere static stability over a variety of geographic locations. Based on this result, they suggested that as global warming strengthens the summer time monsoon-like circulation between the midlatitude continents and oceans, the strengthened subsidence over the northern midlatitude oceans would increase the static stability, increase the low cloud amount, and cool the ocean. This would in turn increase the temperature contrast between the continents and the oceans, and strengthen the monsoon-like circulation.

A number of studies have used satellite albedo and radiative flux data over the extratropical oceans [*Oreopoulos and Davies, 1993; Weaver, 1999; Weaver and Ramanathan, 1996; Weaver and Ramanathan, 1997*]. *Oreopoulos and Davies [1993]* identified significant relationships between monthly albedo and SST over two subtropical regions where low stratiform clouds prevail. *Weaver and Ramanathan [1996, 1997]* and *Weaver [1999]* examined the impact of midlatitude cyclones on the radiative fluxes over the Northern Hemisphere extratropical oceans. Spatial variations in monthly cloud radiative forcings were linked to those of the lower troposphere static stability and the mid-tropospheric vertical velocity [*Weaver and Ramanathan, 1997*].

While the surface observations cover a longer time period and distinguish the different cloud morphological types, an important piece of information for understanding the underlying processes, the satellite data provide a top-down view, a better spatial coverage, and are not limited to the low stratiform cloudiness; variations in the cloud optical depth and other cloud types are also included. This is particularly important over the midlatitude oceans due to the presence of various cloud types [Norris, 1998a].

However, these previous studies are limited by the short temporal data coverage (5 years), the inferred relationships are mostly based on seasonal and spatial variations. Effects of different factors may not be separable in these variations. For instance, *Weaver and Ramanathan* [1997] noted that the January spatial distribution of the monthly cloud shortwave forcing in the North Pacific is independent of the lower troposphere static stability and the strength of the synoptic activity. This result, however, is apparently caused by the cancellation of those two effects: synoptic activity is strongest over the western N. Pacific where the lower troposphere stability is lowest in January.

While the interannual reflectance variability over the extratropical oceans is not particularly large (Chapter 3), the potential coupling between the reflectance and other aspects of the climate system in these regions warrants a closer investigation. Here, we extend these previous studies by using the TOMS reflectance data. The longer temporal coverage of the TOMS data provides more degrees of freedom and helps separating the effects of various processes. In section 5.3, we present a brief review of the various cloud processes over the extratropical oceans. The seasonal variations in the reflectance are discussed in Section 5.4. We then describe the additional datasets and the analysis

methods used in this study (section 5.5). The results are described in Section 5, followed by discussion and some concluding remarks.

5.3 Cloud Processes over the Midlatitude Oceans

A quick inspection of the midlatitude oceans reveals the prominent cloud features associated with the extratropical cyclones (Figure 5.1, Figure 5.2). There have been extensive surface observations of these clouds, which have played important roles in culminating the classical Norwegian cyclone model [*Bjerknes and Solberg, 1922*]. Satellite observations further enriched our understanding of these clouds and the associated cyclone systems [*e.g., Reed 1990*]. The basic cloud feature of extratropical cyclones is the comma-shaped cloud band associated with the ascending regions [*Houze, 1993*]. This comma cloud band has a large vertical extent and exerts strong cloud radiative forcing [*Weaver and Ramanathan, 1996*; evident in Figure 5.1, Figure 5.2 as well]. For a detailed discussion on the formation of the comma cloud, readers are referred to, *e.g., Carlson [1980]*.

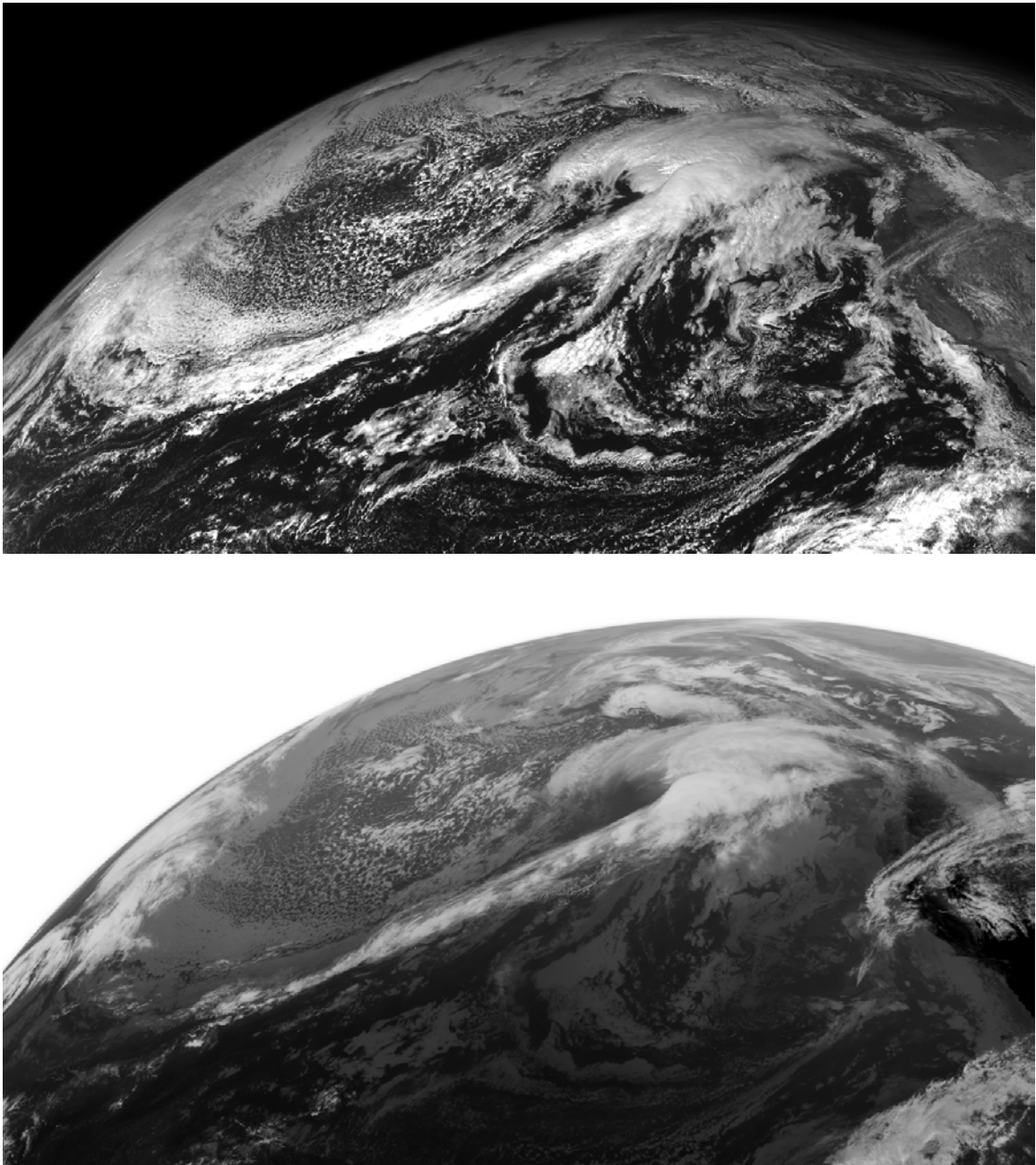


Figure 5.1 Visible (upper) and infrared (lower) images taken by the GEOS-10 geostationary meteorological satellite on November 2, 2001. North American continent is at the east part of the images.

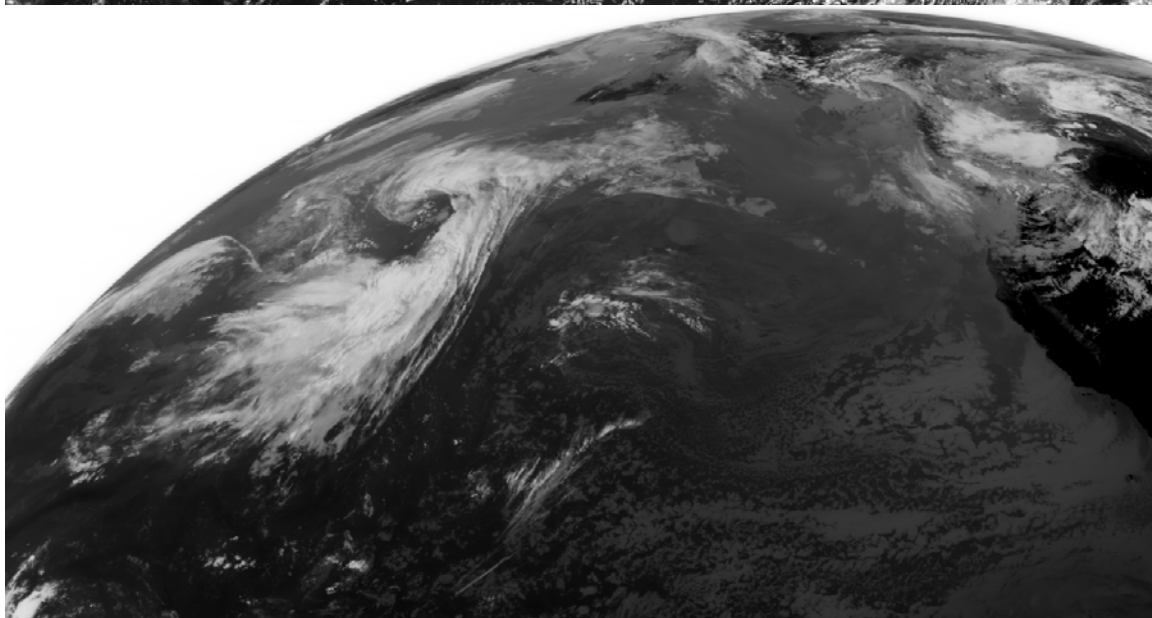
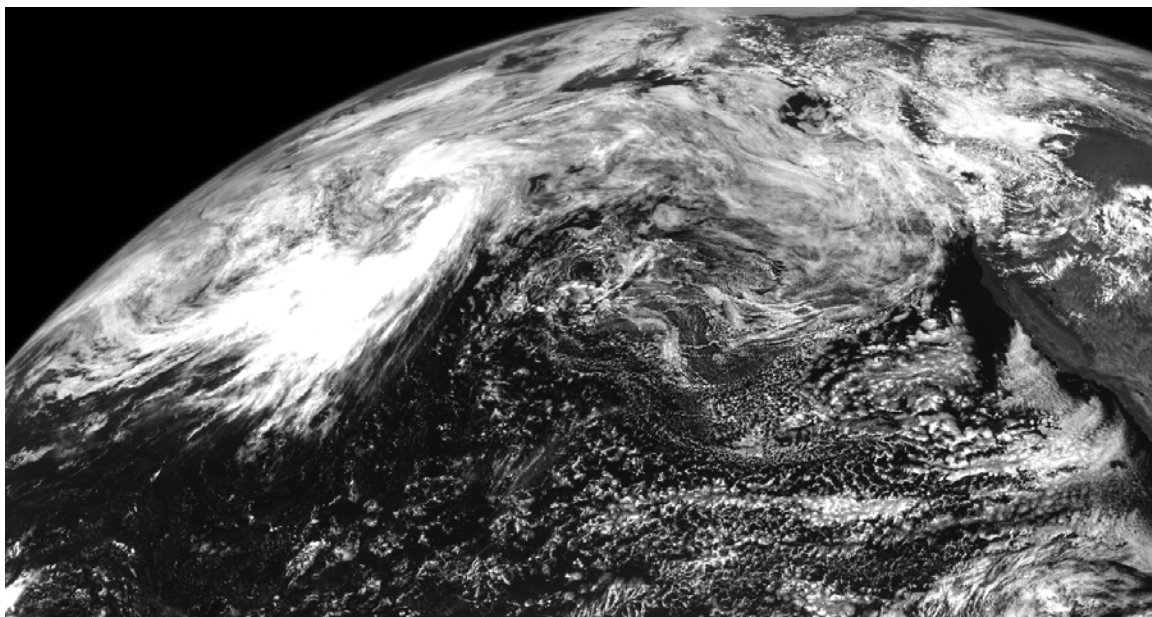


Figure 5.2 The same as Figure 5.1 but for July 17 2001.

Besides the comma clouds, the midlatitude and eastern subtropical oceans also have a large amount of boundary layer clouds. This has been well documented by surface observations [Warren, 1988]. These boundary layer clouds are also evident in the satellite imagery, as they appear bright in the visible image and dark in the infrared. For example, the clouds behind the cold front with a granular appearance in Figure 5.1a are identified as stratocumulus. On the other hand, the low clouds in Figure 5.2 have a more diffusive and smooth texture and are related to stratus clouds. This is also seen in the daily reflectance map taken by the Earth Probe (EP) TOMS instrument at roughly the same time (Figure 5.3). As the TOMS instrument makes measurements at approximately local noontime, the TOMS daily map is a composite map instead of an instantaneous image. The missing data are due to gaps between the EP TOMS orbital tracks. These gaps are absent in the Nimbus-7 TOMS data. In the TOMS data, the comma clouds are associated with very high reflectance (~80%). The stratocumulus behind the cold front in Figure 5.1 has a reflectance of ~20-30%, while the reflectance of the regions covered by the stratus in Figure 5.2 is ~40-50%.

The widespread boundary layer clouds seen over the extratropical oceans may form through two distinct mechanisms [Houze, 1993]. One includes advection of cold air over warm water. The resulting convective instability gives rise to an unstable boundary layer. The boundary layer deepens as it entrains air from above. Clouds form at the top of the boundary layer when the upward convective plumes reach above the condensation level. This mechanism is responsible for the extensive boundary layer cloud cover over the eastern subtropical oceans. Cold air outbreaks from the winter time continents and cold

advection associated with midlatitude cyclones also form extensive boundary layer clouds over the midlatitude oceans. These cloud-topped boundary layers are typically capped by temperature inversions. The clouds may take on different appearances depending on the strength of the mixing and the inversion. For instance, cumulus may form when there is strong mixing and a weak inversion, while stratus is more likely for weak mixing and a strong inversion. A tendency for a more stratiform appearance with an increasing lower tropospheric static stability has been illustrated by composite studies using surface ship observations [Norris, 1998a]. The lower tropospheric static stability may be defined as the potential temperature difference between the surface air and the air above the inversion, and can be used to represent the strength of the inversion.

Boundary layer clouds also form when warm air is advected over a cold surface under stable conditions. As the air is cooled from below, clouds may form first as fog. As the fog thickens and becomes opaque in the infrared, differential radiative heating destabilizes the top layer of the fog. With the enhanced mixing, the fog layer further deepens and sometimes becomes elevated stratus. These clouds are often associated with a deep, stratified cloud layer with little capped inversion [Norris, 1998a].

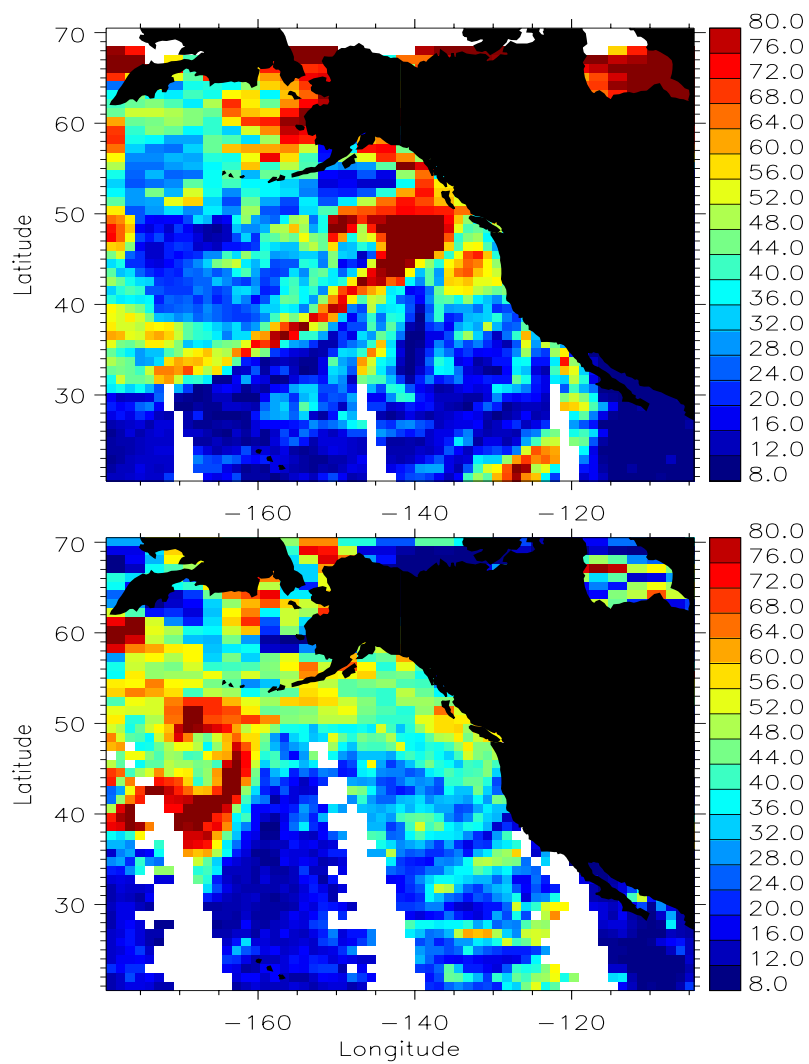


Figure 5.3 The TOMS daily reflectance maps taken at approximately the same time as Figure 5.1 (upper panel), and Figure 5.2 (lower panel).

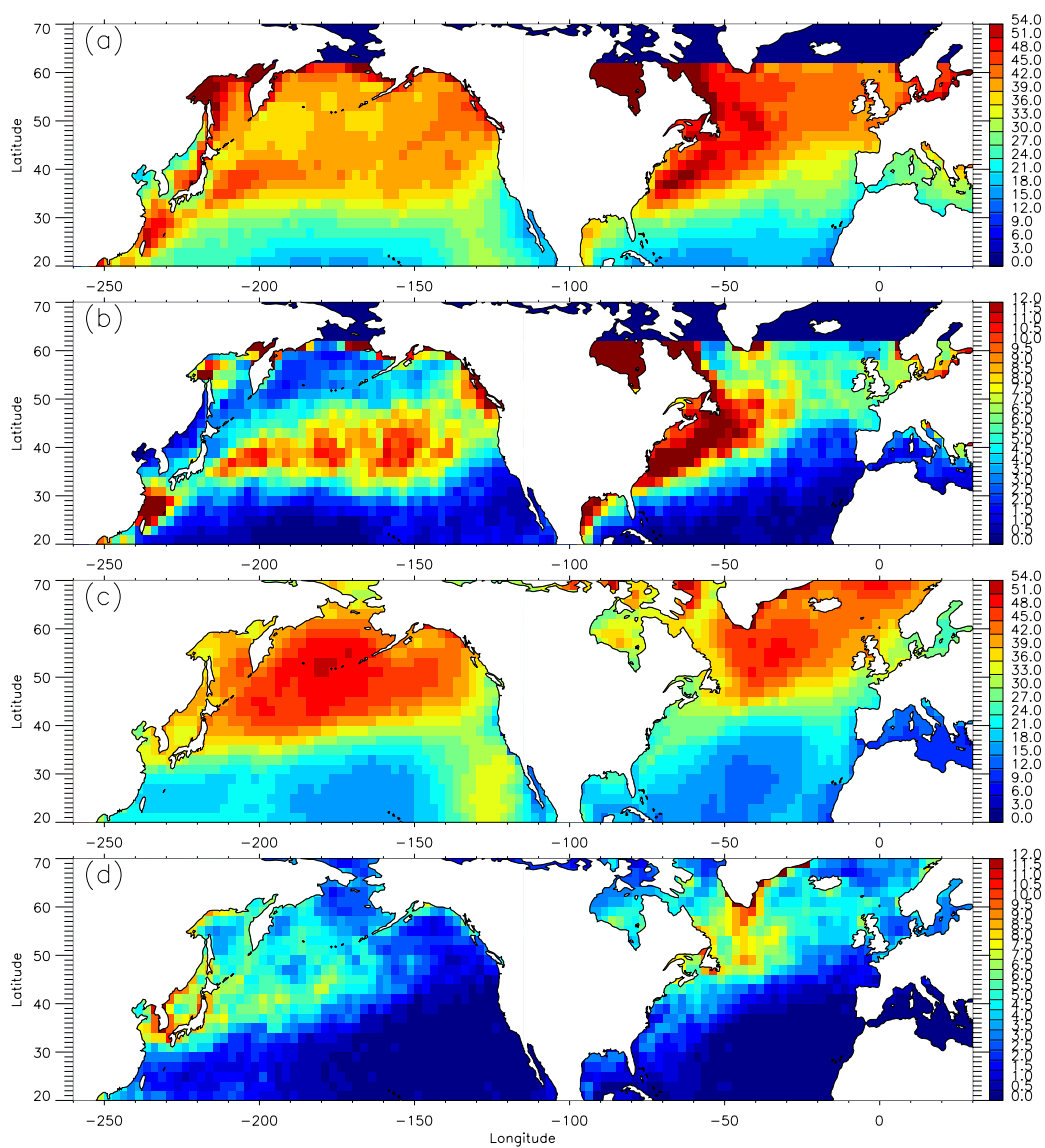


Figure 5.4 Climatological mean reflectance for January (a) and July (c). Contributions from grids with reflectance greater than 75 RU are shown in (b) and (d) for January and July, respectively. The units are RU. There is no data poleward of 62°N in January.

5.4 Seasonal Reflectance Variations

The seasonal cycles of the reflectance are necessarily related to those of the underlying cloud formation processes. The seasonal variations of the storm tracks have been well documented [Chang *et al.*, 2002]. The North Pacific and North Atlantic storm tracks are strongest in the winter season⁴. In summer, following the movement of the jet stream, the storm tracks migrate poleward and become weaker. The lower tropospheric static stability over the ocean, on the other hand, is greater in the summer. The seasonal variation of stability is particularly pronounced over the western North Pacific. The western sides of the northern oceans are characterized by strong cold advection and weak static stability in winter and by warm advection and strong static stability in summer. This seasonal behavior is associated with the seasonal varying temperature difference between the continents and the oceans [Klein and Hartmann, 1993].

The seasonal variations of these meteorological conditions are captured in the TOMS reflectance. The mean TOMS reflectance for January and July (averaged over the period 1979-1992) are shown in Figure 5.4 (a and c). In Figure 5.4 (b and d), we also show the contributions to the January/July mean reflectance from points with TOMS reflectance greater than 75 RU (hereafter this quantity will be referred to as R_{high}). As discussed in the last section, high values (~ 80 RU) in the TOMS reflectance are associated with frontal clouds. We shall use R_{high} as an indicator of contributions from frontal clouds to

⁴ The N. Pacific storm track is known to have a curious midwinter minimum. This behavior, however, will not be discussed here. Interested readers are referred to Nakamura, H., Midwinter Suppression of Baroclinic Wave Activity in the Pacific, *Journal of the Atmospheric Sciences*, 49 (17), 1629-1642, 1992.

the monthly mean reflectance. This indicator is not perfect, because the so-defined R_{high} is dependent on the grid size, as a larger grid size would smooth out the highly reflective clouds to a greater extent. It may, hence, have a latitudinal dependence, as the equal-angle TOMS grid corresponds to a smaller area at higher latitudes. These complications should be kept in mind in interpreting the results. We note, however, that the distribution of R_{high} in general agrees with the International Satellite Cloud Climatology Project (ISCCP) [Rossow and Schiffer, 1991] deep convective cloud plus nimbostratus cloud amount (defined as optical thickness greater than 23, and cloud top above 680 mb), which are based on very high spatial resolution measurements (like those in Figure 5.1, Figure 5.2).

The seasonal variations of the mean reflectance, however, are not dictated by the occurrence of high reflectance. For instance, while the N. Pacific has fewer occurrences of highly reflective points in the summer, its mean reflectance is in fact greater (Figure 5.4). The summer reflectance maximum is due to a higher frequency of intermediate reflectance values (~ 45 RU). The histograms constructed from the 14-year gridded 1.25° longitude by 1° latitude TOMS reflectance are shown in the Figure 5.5 for January (solid) and July (dashed). In constructing the histograms, each grid box is weighted by its area. Regions with sea ice are excluded from the analysis. The bin size is 1 RU, and the total number of grid boxes ranges from 3 to 8 millions. From Figure 5.5a, it is clear that while the summertime N. Pacific has fewer occurrences of reflectance higher than 75 RU, the most frequently occurring reflectance value is ~ 45 RU, typical of a stratus. The most frequent reflectance in winter is ~ 25 RU, characteristic of stratocumulus. The persistency

of summer time stratus over the N. Pacific is evident in daily satellite images like Figure 5.2 and Figure 5.3. In the ISCCP data, this seasonality is expressed in an increased cloudiness for middle to low cloud top (below 400mb) and intermediate optical depth (3.6-23) clouds in summer. The reflectance distribution of the Southern Ocean exhibits a similar seasonality: the winter reflectance (July) distribution has a maximum at ~25 RU, while the summer distribution (January) has a broader maximum from 20 to 45 RU. In comparison, the reflectance distribution over the N. Atlantic has a smaller seasonal variation. In particular, the most frequent reflectance value in January is greater than that of the other two oceans. While the specific distributions depend on the areas that were used to represent the three oceans, the observation that reflectance values of ~45 RU occur more often during seasons with higher lower tropospheric stability is robust.

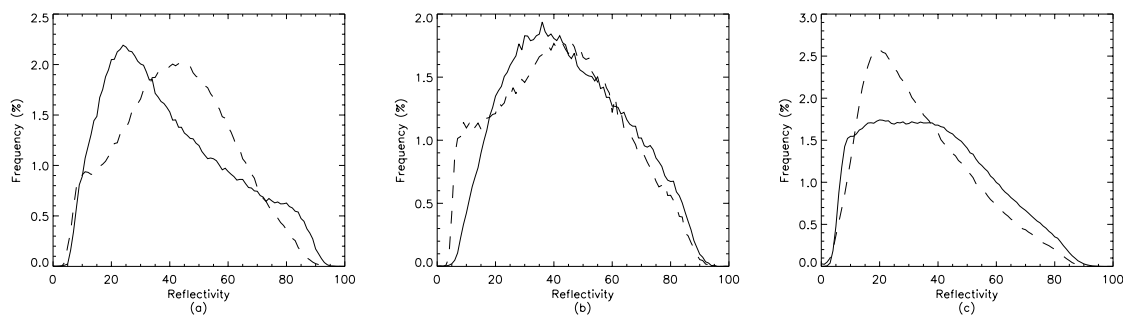


Figure 5.5 Occurrence frequencies for different reflectance values over the N. Pacific 160°E-140°W, 35°N-60°N (a), N. Atlantic 80°W-10°W, 35°N-60°N (b) and the Southern Oceans 180°W-180°E, 65°S-40°S (c) in January (solid) and July (dashed).

5.5 Data and Methods

The time period that we shall examine is 1979-1992. This time period is set by the availability of the TOMS data, which is described in Chapter 3. Various meteorological variables from the National Centers for Environmental Prediction / National Center for Atmospheric Research (NCAR/NCEP) reanalysis [*Kalnay et al.*, 1996] are also used. Parameters of interest include air temperature, humidity, geopotential height, and winds at various pressure levels, and the SST. The pressure level data are available on a 2.5° longitude \times 2.5° latitude grid, and the SST is available in a 192×94 Gaussian grid. Monthly means will be mostly used in this study, although the 4-times-daily data will also be used.

We use the Empirical Orthogonal Function (EOF) analysis to identify large-scale structures in the interannual reflectance variations. The EOF method has been used extensively in the field of meteorology. Readers are referred to, for instance, *Preisendorfer and Mobley* [1988] for more details. We use singular value decomposition (SVD) to further examine the relation between large-scale patterns of reflectance variations and various meteorological variables, including the lower tropospheric stability, the storm track, and the large-scale circulation. The SVD analysis expands two fields into paired patterns so that the explained squared covariance is maximized for any given number of pairs. This method is discussed in some detail in *Bretherton et al.* [1992]. A few useful SVD statistics are summarized below. One is the squared covariance fraction (SCF) of a pair of patterns, defined as the squared covariance

explained by this pair divided by the sum of the squared covariance explained by all pairs from the SVD expansion of two fields. As described in *Bretherton et al.* [1992], the SCF is a good indication of the relative importance of a pair of patterns in the expansion of two fields. Another useful statistics is the normalized covariance (NC), defined as the covariance explained by a pair normalized by the square root of the product of the total variances within each field [*Zhang et al.*, 1998]. NC provides a measure on the absolute strength of the coupling between the two fields as represented in a given pair of SVD patterns. The correlation coefficient r between the time series of a given pair will also be used as an indication of the strength of the coupling. The statistical significance of these statistics is tested by Monte-Carlo experiments that take into account the spatial coherence and the auto-correlation within each field [*Norris*, 2000].

We use $\theta(700\text{ mb})-\theta(1000\text{ mb})$ to represent the lower tropospheric stability, where θ is the potential temperature. Alternative choices of using moist potential temperature difference instead of θ difference or pressure levels such as 500 mb or 850 mb instead of 700 mb give similar results. We use the 3-30 day band pass filtered root-mean-square (rms) daily pressure vertical velocity (ω) at 500 mb (hereafter rms ω) to represent the strength of synoptic activity. Maxima in rms ω approximate the storm track. It needs to be noted, however, that many other band pass filtered variances or covariances can be used to diagnose synoptic activities. Different diagnoses may give slightly different descriptions of the storm track [*Trenberth*, 1991]. The effect on our results will be discussed. R_{high} will also be used as a diagnosis of the storm track. Derived from reflectance measurements, R_{high} is a more direct measure of the effect of frontal clouds on

the reflectance than the other diagnoses. The 500mb geopotential height will be used to diagnose variations in the large scale circulation.

The regions that we shall examine are the N. Pacific (150°E-110°W, 20°N-60°N) and the North Atlantic (70°W-0°W, 20°N-70°N). Although a smaller N. Pacific domain is used to reduce the influence from tropical western Pacific, the results presented in the following are unchanged when a broader domain (120°E-110°W instead of 150°E-110°W) is used. These domains are used for the reflectance, R_{high} , lower tropospheric stability, 500mb rms ω . For these variables, land areas and areas with climatological sea ice concentrations greater than 3% have been excluded from the analyses. For the 500mb geopotential height, we have used the sector of 100°E-30°W, 20°N-85°N to pair with the N. Pacific and the sector of 120°W-60°E, 20°N-85°N to pair with the N. Atlantic. The four seasons are examined separately, and the results for the December-February (DJF) and the June-August (JJA) seasons are presented. The results are in general not sensitive to the specific domain selection and the exclusion of land areas. The few exceptions will be noted. The percentage variance explained by the leading two EOFs for various fields are summarized in Table 5.1. Table 5.2 and Table 5.3 present the correlation coefficients between the time series of the leading EOFs for DJF and JJA, respectively. The SVD statistics between various fields and the reflectance field are summarized in Table 5.4.

5.6 Results

a. DJF North Pacific

Figure 5.6 displays the leading EOF patterns of the DJF season for the reflectance (a), stability (b), R_{high} (c), rms ω (d), 500mb height (e), together with their time series (f). The time series are normalized. Values in the EOF patterns represent the magnitude of the variations for a 1 standard deviation variation of the EOF time series. The units are RU, for reflectance and R_{high} , Kelvin for stability, mb/day for rms ω , and meters for 500mb height. As the patterns resulted from EOF/SVD analyses carry arbitrary signs, we have arranged the signs so that all patterns are of the same polarity. These apply to the rest of this Chapter as well. The first EOF of the reflectance field explains 21% of the total variance in the reflectance field (Table 5.1) and is well separated from the second mode, by the criterion proposed by *North* [1982]⁵. The time series of the leading EOFs of all variables are significantly correlated (Table 5.2). The statistical significance is calculated through Monte-Carlo experiments that take into account the auto-correlation within each time series. As these EOF time series emerge from completely separate analyses, the strong correlations among the different fields in the N. Pacific winter provide a strong indication that these aspects of the climate system are highly organized. The SVD analyses, designed to extract correlated patterns in two fields, not surprisingly, produce similar results (Table 5.3).

⁵ The criterion is that the separation between the variances (λ) explained by two successive EOFs, $\Delta\lambda$, needs to satisfy $\Delta\lambda > \lambda(2/N)^{1/2}$, where N is the number of realizations.

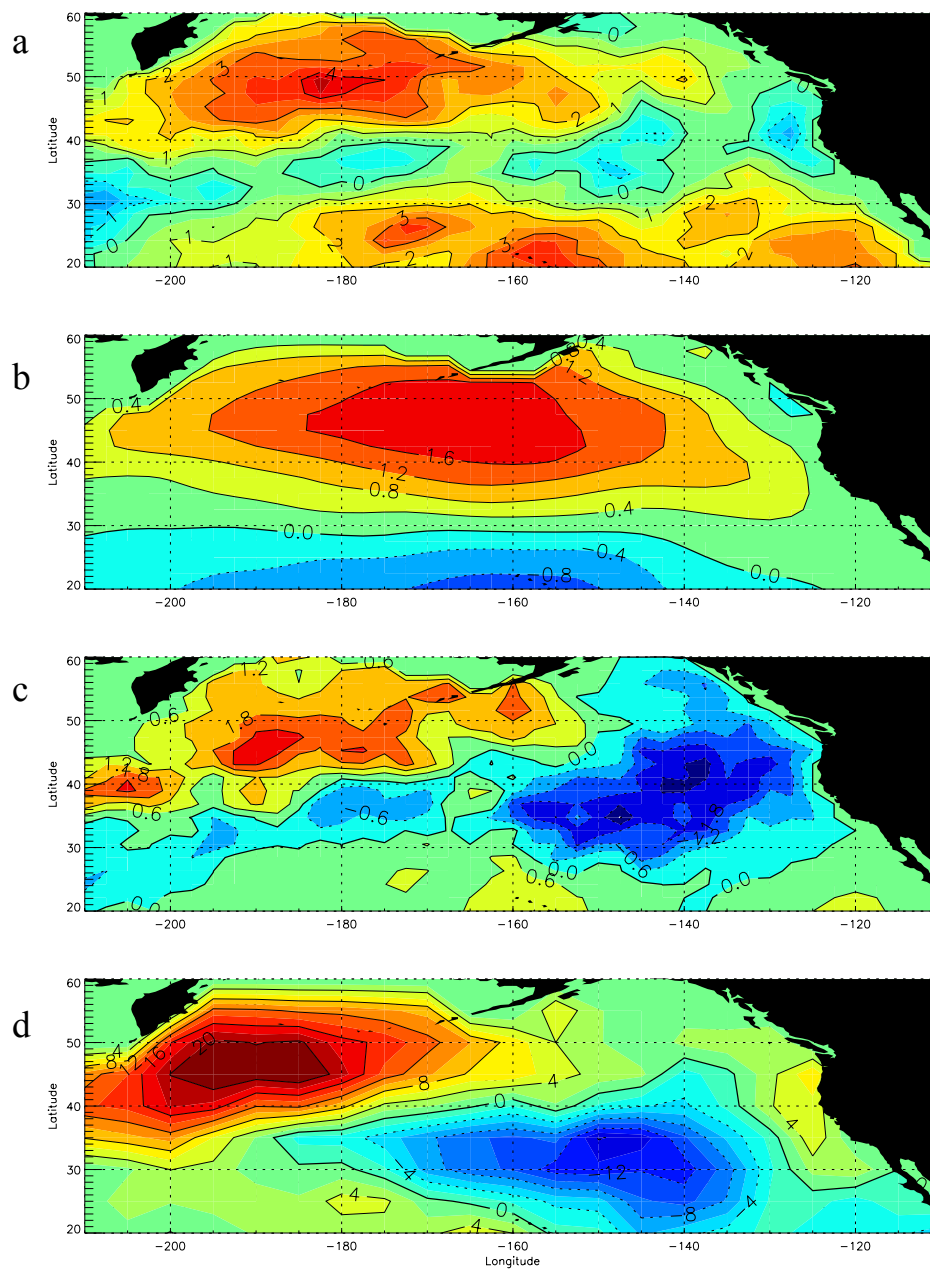


Figure 5.6 The leading EOF patterns of the following fields for the DJF N. Pacific: from top to bottom (a) reflectance, (b) lower tropospheric stability, (c) R_{high} , (d) 500mb rms ω (to be continued).

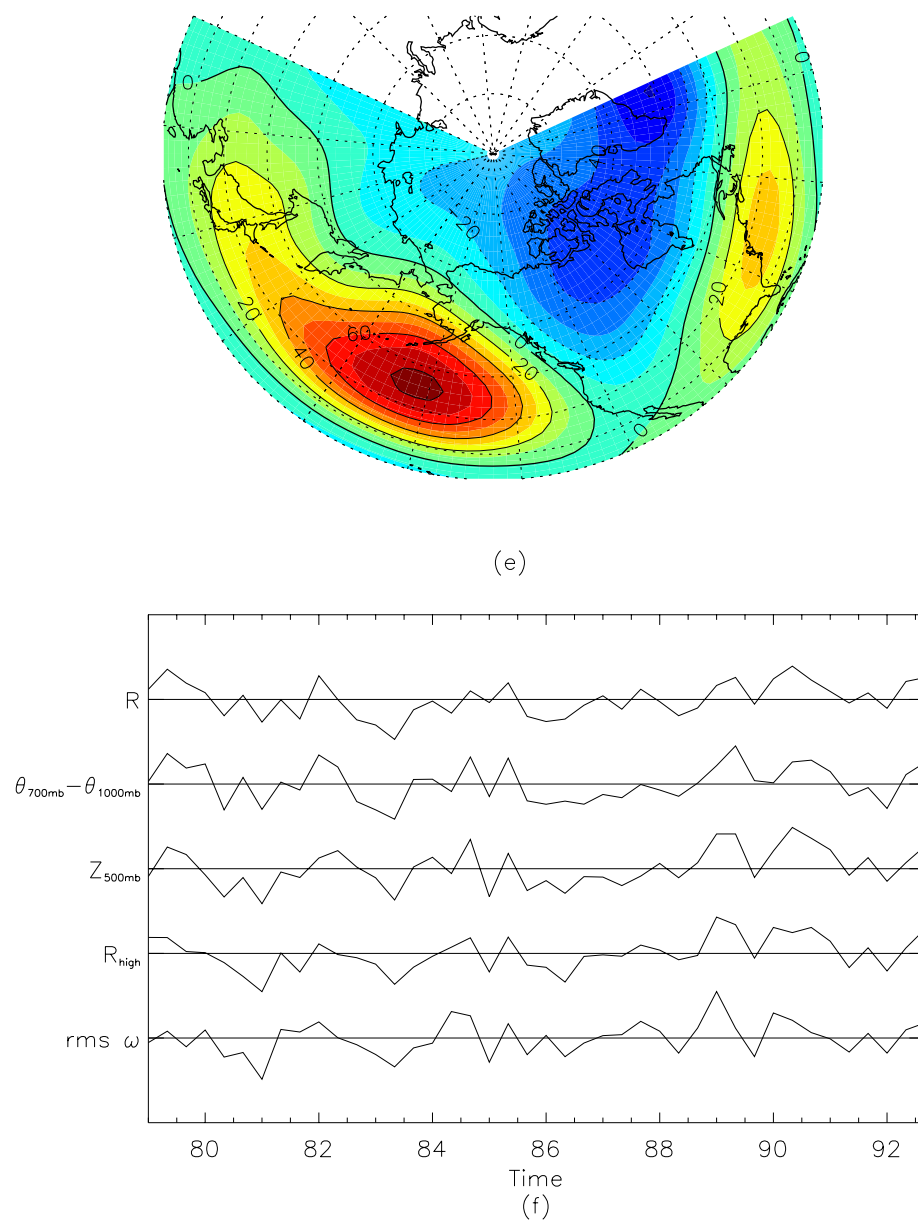


Figure 5.6 (continued) The leading EOF patterns of 500mb geopotential height (e) and the time series of the leading EOFs (f). Negative contours are dotted.

The physical interpretation of these patterns and their relationships is as follows. The leading EOF of the 500mb height (Figure 5.6e) resembles the Pacific-North Atlantic (PNA) pattern (negative phase) [Wallace and Gutzler, 1981]. The PNA pattern may be understood in terms of a Rossby-wave train originating from the subtropical upper troposphere, induced by outflows from tropical convection [Trenberth *et al.*, 1998]. Associated with the positive/negative phase of the PNA pattern, the subtropical jet stream shifts southward/northward. The mean flow steers the weather disturbances and causes a equatorward/poleward shift in the N. Pacific storm track, as seen in Figure 5.6 d [also see Lau, 1988]. The pattern of the rms ω is essentially unchanged when the land area is included or a wider domain or a longer time period is used. It is worth noting, however, that the specific position of the storm track and the pattern of its variation do depend on the particular statistics used to represent the storm track [Trenberth, 1991]. For instance, if the rms 200mb band pass filtered (2-8 days) meridional wind, or the rms 500mb height is used, the positive and negative anomalies are more east-west oriented so that the shift in storm track has a more meridional nature. The shift in the storm track is naturally reflected in the reflectance field. In particular, the leading EOF of R_{high} (Figure 5.6c) exhibits such a shift. However, a shift in the storm track does not explain the leading EOF pattern of the total reflectance field, which is characterized by an elongated band with slightly negative anomalies and strong positive anomalies to the north and south of this band. This pattern is in contrast to that of a shifting storm track where the positive and negative anomalies have similar magnitudes. We relate this difference to variations in the lower tropospheric stability field (Figure 5.6b). In the same manner as the Rossby-wave train induces the 500mb height pattern, it also induces corresponding patterns in the

lower tropospheric stability. As stronger lower tropospheric stability tends to increase the stratiform nature of the clouds associated with an unstable boundary layer [Norris, 1998b], it increases the fractional cloud cover and hence the reflectance. An increased stability is, therefore, expected to increase the reflectance north of the storm track where unstable boundary layers prevail due to the frequent cold advection. On the other hand, over the western and central subtropical Pacific, the cloud cover is dominated by cumulus. A weakened subtropical high, and a reduced stability thus favor the occurrence of more cumulus and increase the reflectance. Based on these discussions, the leading EOF pattern of the interannual reflectance variation over the DJF N. Pacific appears to be closely related to the PNA circulation pattern through variations in the position of storm track and the strength of the lower tropospheric stability.

Region	North Pacific		North Atlantic	
	DJF	JJA	DJF	JJA
R	21/9	16/12	16/12	13/11
$\Delta\theta$	35/21	17/15	32/24	26/14
$Z_{500\text{mb}}$	23/18	15/11	28/15	21/13
rms ω	20/12	23/10	22/15	27/9
R_{high}	14/9	10/8	14/11	10/7

Table 5.1 Fractional variances explained by the leading two EOFs in various fields. Units are percent. The data is presented in the form of a/b where a and b are the percentage variances explained by EOF1 and EOF2, respectively.

	Stability	R_{high}	rms ω	Z(500mb)
R	86/32	80/74	62/55	78/27
Stability		75/33	62/59	83/35
R_{high}			82/58	85/10
Rms ω				73/20

Table 5.2 Correlations between the time series of the first EOFs of various variables for the N. Pacific. Within each pair, the first value is for the DJF season, and the second value for JJA. Units are in %. Bold indicates 99% significance.

	$\Delta\theta$	R_{high}	rms ω	Z(500mb)
R	53/71	79/75	75/59	58/37
Stability		14/69	46/65	62/63
R_{high}			59/70	43/48
Rms ω				54/52

Table 5.3 The same as Table 5.2, except for the N. Atlantic.

	Stability	R_{high}	rms ω	$Z_{500\text{mb}}$
N. Pacific	75/25/92	46/15/94	51/15/82	66/20/90
	25/10/78	30/11/95	44/13/78	28/10/91
N. Atlantic	49/18/85	38/14/95	49/16/88	48/17/87
	49/16/87	26/10/94	50/14/86	42/13/84

Table 5.4 Statistics from paired SVD analyses between reflectance anomalies and those of various variables over N. Pacific and N. Atlantic. The values are presented as SCF/NC/r. Bold indicates 99% significance. Units are percent.

b. DJF N. Atlantic

The variables under consideration here are not as closely related to each other over the N. Atlantic compared to that seen over N. Pacific in DJF. This is evident in their correlation coefficients (Table 5.2). Therefore, in Figure 5.7, we present the leading EOF pattern of the reflectance field, together with leading SVD patterns of various fields when they are paired with the reflectance field. This distinction, however, appears unnecessary, as the SVD patterns closely resemble those from the EOF analyses.

The leading EOF pattern of the reflectance field is characterized by an elongated positive anomaly. A very similar pattern is seen in R_{high} and rms ω . However, when the ice covered areas and the land areas are included, the 500mb rms ω pattern exhibits both positive and negative anomalies, and suggests a shift in the storm track (Figure 5.7f). The lack of a strong negative anomaly in Figure 5.7 a, c, d is apparently because the area around Greenland is where the negative anomaly resides. The SVD pattern of the 500mb height is shown in (Figure 5.7 e). This pattern resembles that of the negative phase North Atlantic Oscillation (NAO) except that the negative anomaly is shifted towards the west. When a longer time period is used, the leading EOF of the 500mb height over the Atlantic section follows the NAO pattern more closely. Similarly, the negative anomaly in the lower troposphere stability field is also shifted towards the east when a longer period is used. The difference between Figure 5.7 and the canonical NAO pattern is, therefore, attributed to the non-stationary nature of the circulation. This cautions the interpretation of the EOF/SVD patterns from our rather short record: while the general

patterns, such as the shifts in the storm track, should hold, the detailed features may vary when longer records are available. The patterns in the storm track and the 500mb height are consistent with the findings of [Lau, 1988], which shows that the NAO pattern corresponds to a meridional shift in the storm track.

The time series of the leading EOFs of reflectance and stability are 99% significantly correlated, and the first SVD patterns have 99% statistical significance except for SCF, which is significant at a 95% level. However, the SVD pattern of stability bears little similarity to the pattern of reflectance variation. In fact, the expected reflectance variation from the pattern of stability is in general opposite of that in the pattern of the reflectance variation. This, together with the resemblance between the patterns of R and R_{high} , suggests that stability has little effect on the interannual reflectance variations over the DJF N. Atlantic and the latter is mostly due to the meridional shifting of the storm track. The correlation between reflectance and stability variations is likely because they both respond to large scale circulation variations. This difference from the DJF N. Pacific is explained in terms of the difference in the position and the strength of storm tracks over the two basins. The DJF Pacific storm track is weaker, and more importantly, there is a large area north of the Pacific storm track where the occurrence of frontal clouds is minimal, and variations in the boundary layer clouds can control the reflectance. Such a setting is absent in the N. Atlantic.

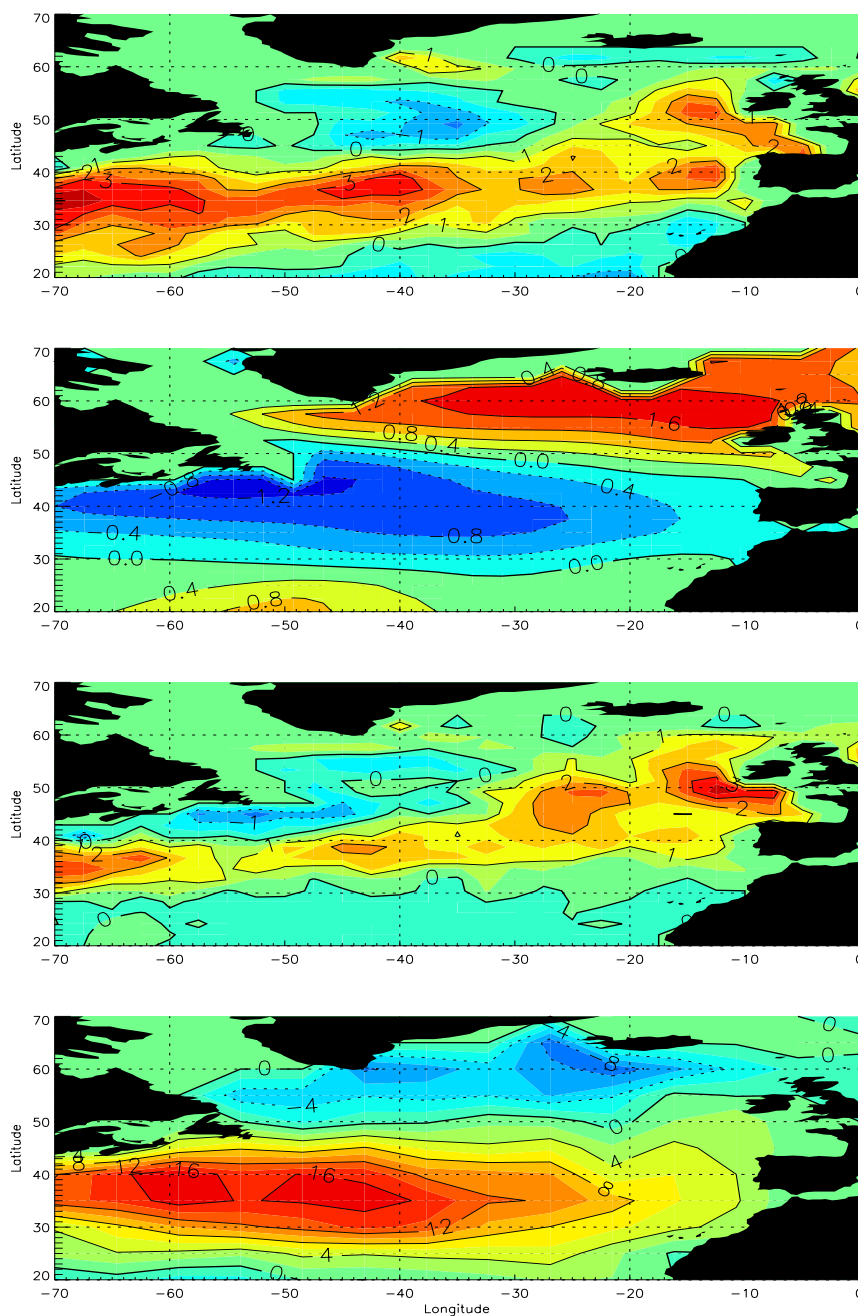
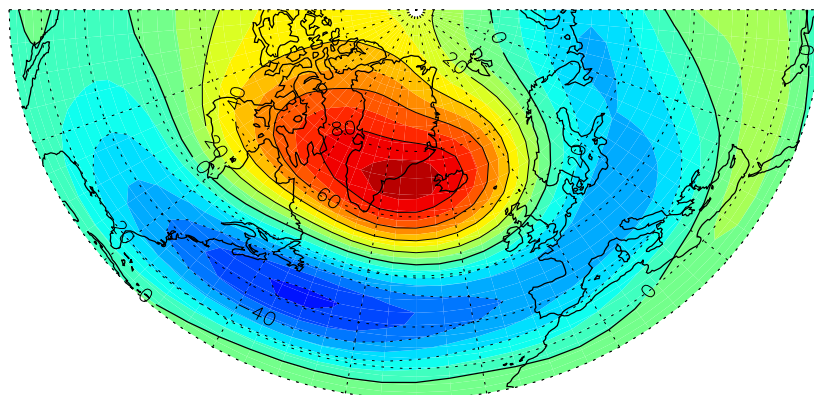
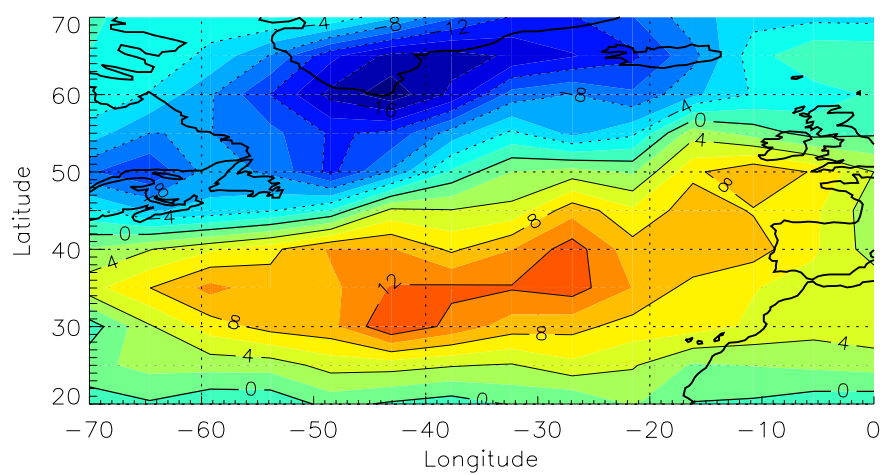


Figure 5.7 Leading EOF/SVD patterns over the DJF N. Atlantic. From top to bottom: (a) the leading EOF pattern of reflectance (a), the leading SVD patterns of the following quantities when paired with the reflectance: stability (b), R_{high} (c), 500mb rms ω (d), (and on the next page) 500mb height (e), and 500mb rms ω when the ice covered area and the land areas are included (f) (to be continued).



(e)



(f)

Figure 5.7 (continued)

c. JJA N. Atlantic

The various patterns are quite similar over the N. Atlantic in JJA as in DJF (Figure 5.8). In Fig 5.8 d, we display the leading EOF pattern of 500mb rms ω when land and ice covered area are not excluded. The leading pattern in reflectance is also associated with a shift in the storm track. The associated circulation pattern is weaker than the winter and resembles that of the negative phase NAO in summer (not shown). The positive anomaly around the Canary Islands is likely associated with a strengthened subtropical high and an increased stability (Fig 5.8 b), as stratocumulus tends to prevail in these regions during the summer season [*Klein and Hartmann, 1993*]. The negative anomaly to the north in the reflectance field may also be related to the large negative anomaly in the stability field.

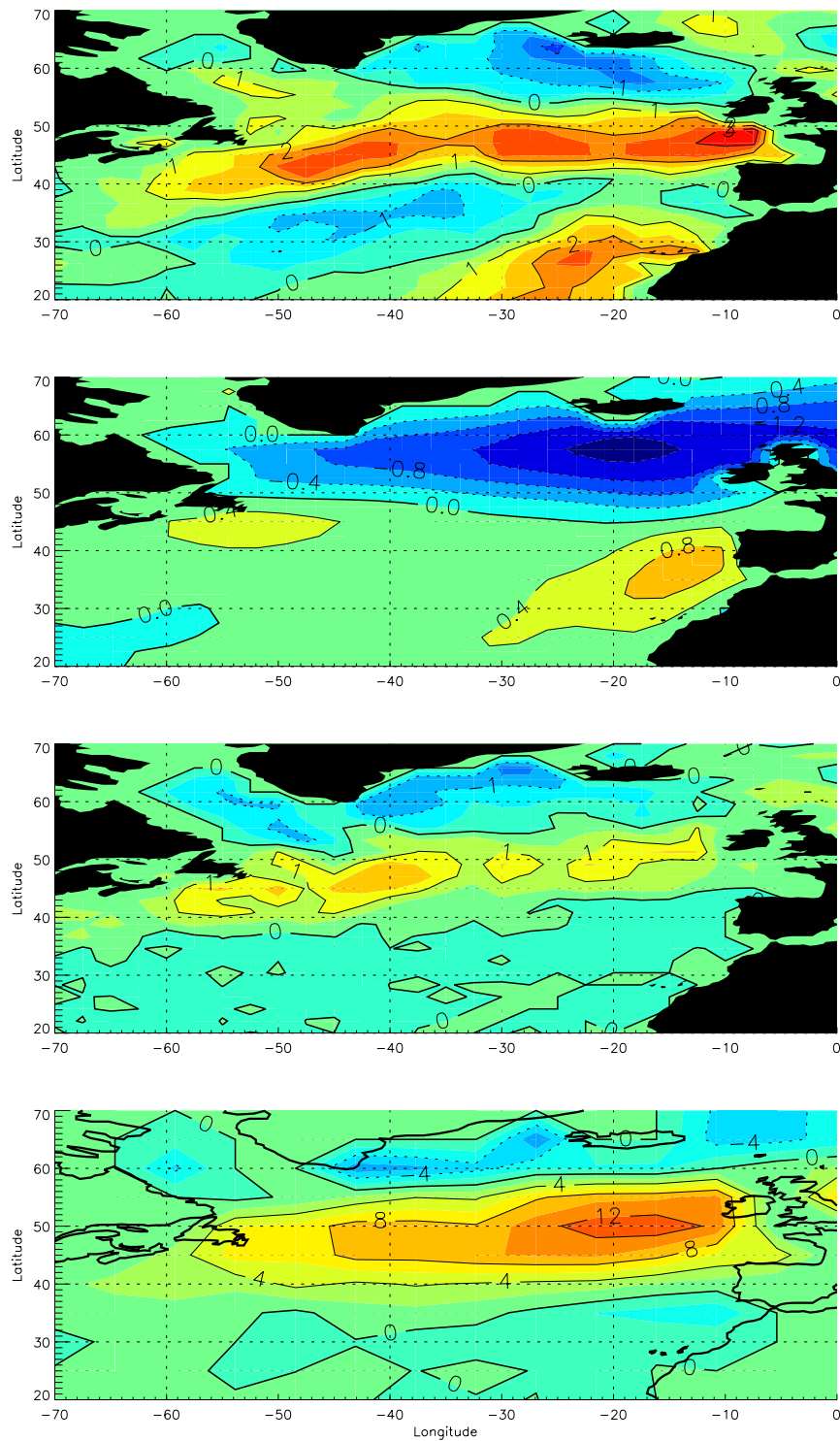


Figure 5.8 Top to bottom (a-d): the same as Figure 5.7 a,b,c,f, except for JJA N. Atlantic.

d. JJA N. Pacific

The leading EOF pattern of the reflectance variations over the JJA N. Pacific is characterized by an elongated positive anomaly on the west side of the basin and a weaker feature on the east side of the basin (Figure 5.9). The leading SVD pattern between reflectance and stability failed statistical significance tests on all measures (Table 5.4) and is not presented.

The reflectance anomaly on the west resembles the anomalies in the leading SVD patterns of R_{high} and $\text{rms } \omega$ (Figure 5.9). Because the center of the positive anomaly in these patterns lies to the south of the climatological summertime storm track maximum, this suggests an intensification and equator-ward shift in the storm track [Norris, 2000]. The negative reflectance anomaly has a more tropical origin and is more directly related to the El Niño Southern Oscillation (ENSO) [Fu *et al.*, 1996], although the midlatitude circulation in general is also influenced by the ENSO [Chang *et al.*, 2002]. The reflectance anomaly on the eastern side of the basin appears not directly related to frontal clouds. Klein *et al.* [1995] related the summertime boundary layer cloud variations over this part of the Pacific basin to the variations in the subtropical high. The pattern in Figure 5.9 over the east Pacific is consistent with the cloud variations associated with a weakened subtropical high, as identified in that study. A similar conclusion was reached by Norris *et al.* [1998]. Given the few frontal clouds in this region during summer (Figure 5.4d), it appears appropriate to attribute the reflectance variations in this region to those of the boundary layer clouds, and hence to variations in the subtropical high. A

weakened subtropical high reduces the incidence of cold advection over the stratocumulus region off the California coast. This results in the decreased reflectance. The weakened subtropical high also allows more intrusions of midlatitude synoptic activities. These activities increase the stratiform clouds in the midlatitude stratus regime and disrupt the boundary layer processes in the subtropical stratocumulus regime [Klein *et al.*, 1995]. The zero contour in Figure 5.9a over the eastern N. Pacific appears to separate the midlatitude and the subtropical regimes (compare with Figure 5.4a).

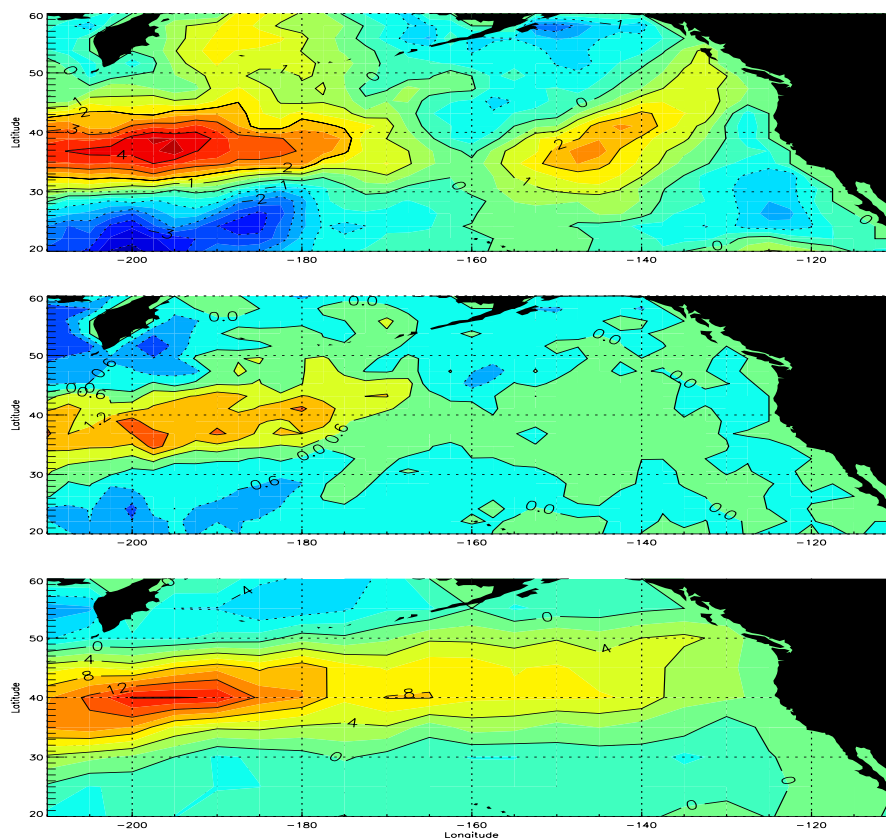


Figure 5.9 Leading EOF/SVD patterns over the JJA N. Pacific. From top to bottom: the leading EOF pattern of reflectance (a), and the leading SVD patterns of the following quantities when paired with the reflectance: R_{high} (b), 500mb rms ω (c).

e. Relation between Summertime Reflectance and SST

An outstanding question in the study of midlatitude climate variability is the ocean-atmosphere interaction. The atmospheric influence on the extratropical SST has been well established [Frankignoul, 1985]. The SST anomalies can be generated by anomalous sensible/latent heat flux across the air-sea interface or by anomalous wind driven turbulence mixing or Ekman pumping. Whether the midlatitude SST anomalies can effectively force a response in the atmospheric circulation to substantiate an ocean-atmosphere feedback has been actively studied but remains controversial [Kushnir *et al.*, 2002]. The study of midlatitude air-sea interaction has mainly focused on the winter season, when the air-sea coupling is the strongest. More recently, Zhang *et al.* [1998] examined the air-sea interaction during the summertime N. Pacific, and concluded that the leading summertime SST anomaly pattern is at least as persistent as that in winter, and it varies coherently with its winter counterpart. Since the ocean mixed layer is considerably shallower in the summer, a summertime low cloud-SST feedback was invoked to explain the persistency of the summer SST anomaly patterns [Norris *et al.*, 1998]. As this feedback is in essence a reflectance-SST feedback, an examination of the relation between reflectance and SST appears appropriate.

Figure 5.10 displays the SVD patterns between reflectance and SST over the summertime (JJA) N. Pacific (a) and N. Atlantic (b). The correspondence between positive reflectance anomalies and negative SST anomalies is quite remarkable. A similar correspondence between marine stratiform clouds (MSC) and the SST was interpreted as the response of MSC to the SST anomalies, and a feedback was inferred based on the effect of MSC on

reflecting sunlight [Norris *et al.*, 1998]. This view, however, is not supported by our analysis. As discussed in the previous sections, the reflectance anomalies over the JJA N. Atlantic and west N. Pacific are related to the storm track, and more specifically, to the highly reflective frontal clouds. While the R_{high} patterns in Figure 5.8c, Figure 5.9b have smaller amplitudes than their counterparts in total reflectance (Figure 5.8a, Figure 5.9a), this difference is mostly because we have only included contribution from grid boxes with reflectance greater than 75RU, which, while illustrates the pattern, necessarily underestimates the contribution from the frontal clouds. A lower threshold for R_{high} (65RU) produces patterns with amplitudes that approach those in the total reflectance field (not shown). While the choice of the threshold for R_{high} has some uncertainties, a reflectance of 65RU should be sufficiently higher than that of most MSCs. The majority of the reflectance variations, thus, appear unrelated to MSC variations. This argues against boundary processes between SST and MSC as being important for the reflectance-SST correspondence. Instead, it is more appropriate to view the correspondence between an increased reflectance and a decreased SST as a consequence of both responding to anomalous synoptic activities. In the JJA eastern N. Pacific, boundary layer clouds are more important contributors to the reflectance variations. However, as pointed out by [Klein *et al.*, 1995], the circulation variations associated with an anomalous subtropical high may also simultaneously drive anomalies in the SST and MSC. Based on our results, there appears little evidence for an MSC-SST feedback over midlatitude oceans during summer. We speculate that the effect of SST anomalies (or SST gradient anomalies) on the storm track may hold more promises for an explanation for the persistence of the summertime SST anomaly. For instance, it is possible that

changes in the SST can affect the storm track by modifying the low level baroclinicity. How the atmospheric circulation responds to extratropical SST anomalies remains an active research topic [*Kushnir et al.*, 2002].

While we believe that the reflectance anomalies and the SST anomalies are both responding to anomalous synoptic activities, reflectance variations over the summertime northern oceans can, nevertheless, be important for the energy budget in these regions. We have identified statistically significant SVD patterns between the reflectance field and the surface heat flux out of the ocean (sensible heat + latent heat), over the JJA northern oceans. The SVD patterns in the surface heat flux (Figure 5.11) bear many similarities to those in the reflectance field that were identified as due to storm track variations (Figure 5.8 and Figure 5.9). This is consistent with our interpretation, as increased synoptic activities increase both the reflectance and the surface heat flux. Simple estimates indicate that the shortwave forcing due to the reflectance variations is of a similar magnitude to the surface heat flux variations, reaching $\sim 20\text{W/m}^2$. We have assumed an incoming solar flux of $\sim 400\text{W/m}^2$, appropriate for the summertime northern oceans. Therefore, reflectance variations do appear to be a significant player in the heat budget over these regions. This is not true in the winter, where variations in the surface heat flux far exceed the contributions from the reflectance variations (not shown).

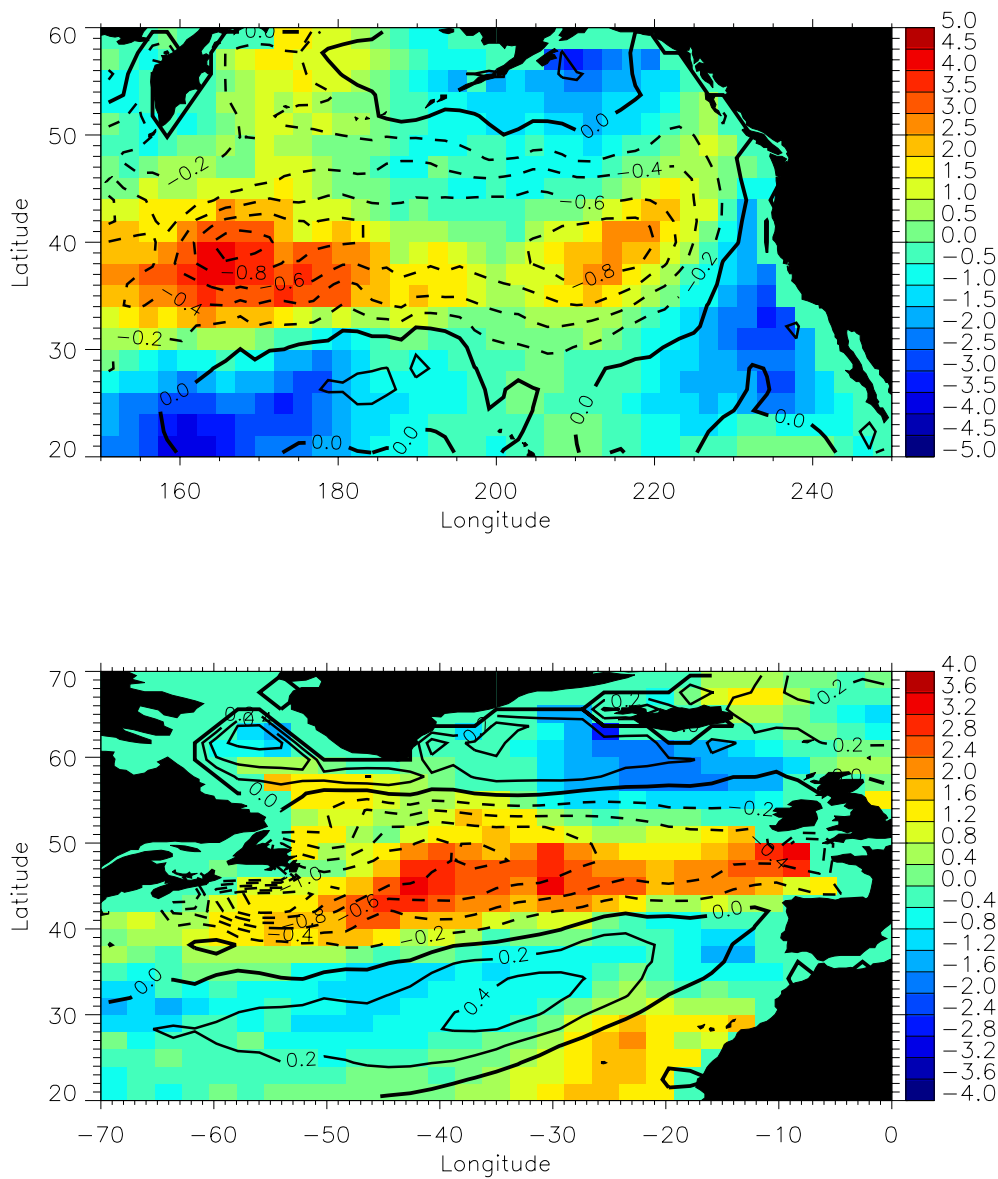


Figure 5.10 The leading SVD patterns between reflectance (color) and SST (contours) over the JJA N. Pacific (a) and N. Atlantic (b). The units are Kelvin and RU for SST and reflectance anomalies, respectively.

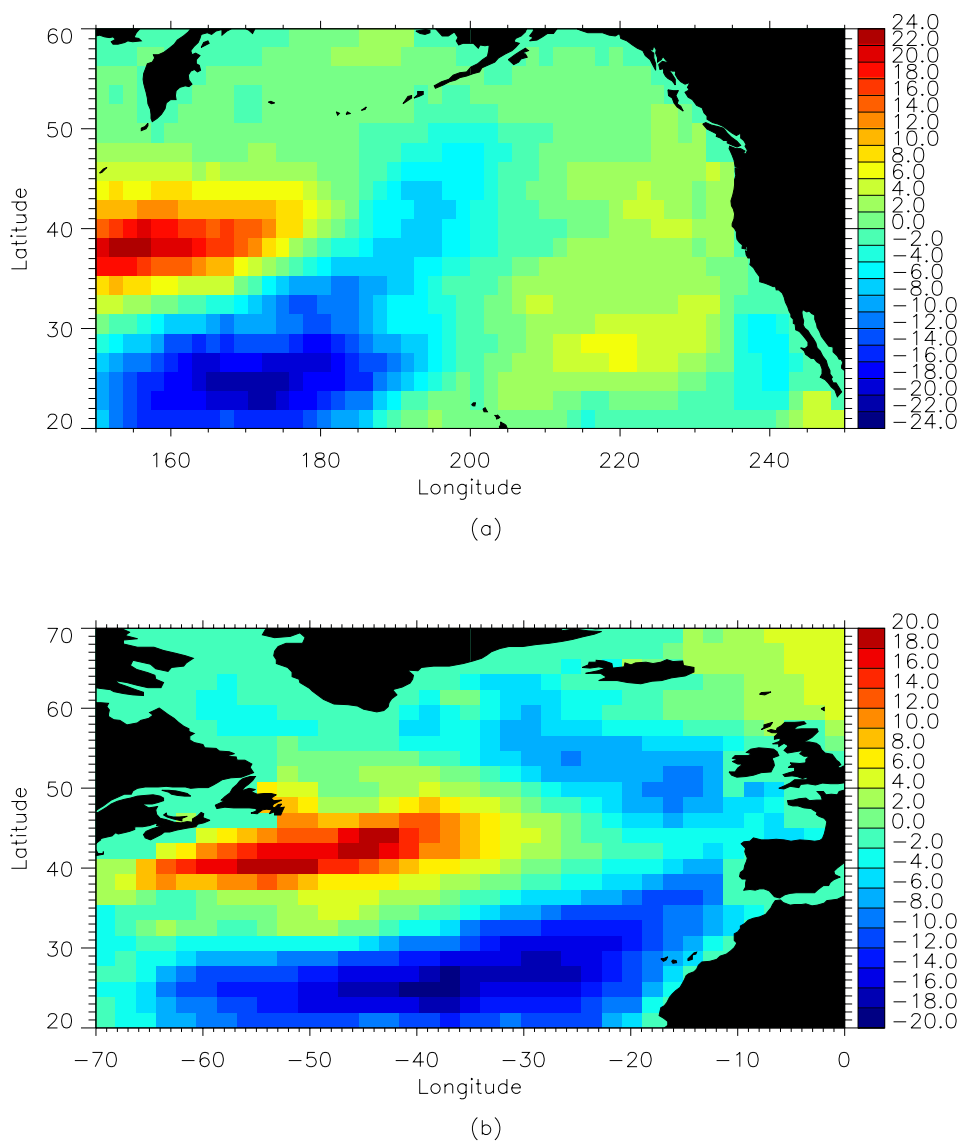


Figure 5.11 The SVD patterns of surface heat flux when it is paired with the reflectance for JJA N. Pacific (a) and JJA N. Atlantic (b). Units are W/m^2 .

5.7 Discussion

It is worth noting that except for the DJF N. Pacific, the first two EOFs of the reflectance field for the other three cases that we present are not considered as statistically well separated [North *et al.*, 1982]. In interpreting them as independent, physical patterns of variations, we have used their relation with the storm track variations and, of course, some physical intuition. The relation between the storm track and the reflectance in these cases is robust, not only in the sense that their covariability statistics for the leading SVD patterns are significant; a local correspondence between reflectance, R_{high} and rms ω in the following pairs of SVD patterns is observed as well.

The seasonal variation of the relation between stability and reflectance is particularly interesting and warrants more discussion. Figure 5.12 displays the local correlation between interannual variations of stability and the reflectance over the N. Pacific for the four seasons. For the calculation of local interannual correlations, we average the TOMS monthly reflectance onto a 2.5° longitude \times 2° latitude grid, with grid centers at 0° , 2.5° , 5°E , etc., and 89° , 87° , 85°S , etc. Meteorological variables from the NCEP reanalysis are interpolated onto this grid. Linear correlations were calculated between the monthly anomalies of the reflectance and stability for each grid.

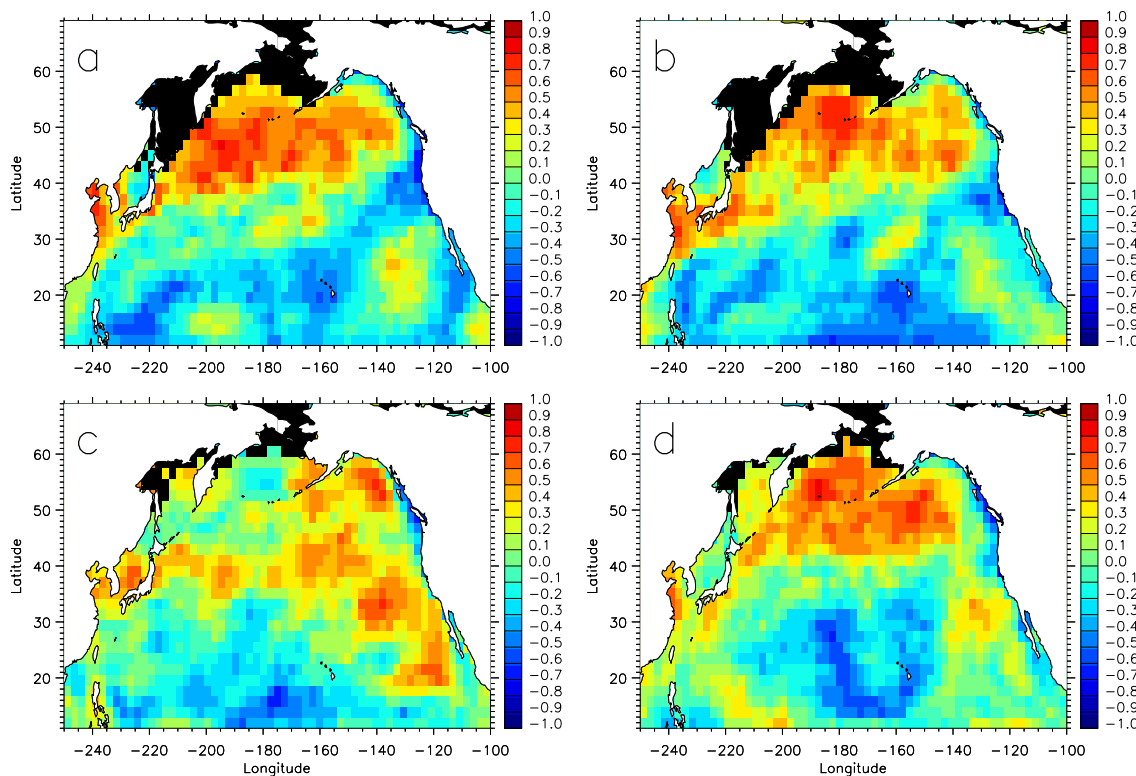


Figure 5.12 The interannual local correlation coefficients between reflectance and stability anomalies for DJF (a), MAM (b), JJA (c) and SON (d), over the N. Pacific Areas with sea ice are excluded.

The significant correlation (99% significance is ~ 0.4 as suggested by Monte-Carlo experiments) found over broad areas north of the N. Pacific storm track confirms the reflectance-stability relation depicted in the EOF/SVD analysis. Also consistent with the EOF/SVD analyses, there is no correlation over the western N. Pacific during JJA. This is particularly interesting as the summertime western N. Pacific is the region with the maximum lower tropospheric stability and low stratiform clouds. The in-phase seasonal cycles of the two have led to the proposition of a positive feedback between the summertime midlatitude stratus and the monsoon-like circulation between the midlatitude

continents and oceans [*Klein and Hartmann, 1993*]. Our analysis, however, suggests that the reflectance becomes independent of the lower tropospheric stability when the latter becomes sufficiently large. This behavior is also evident in the day-to-day reflectance variations.

We have averaged the daily 1.25° longitude by 1° latitude TOMS reflectance into static stability bins for the JJA N. Pacific⁶ (Figure 5.13). Cases with positive and negative 500mb ω are shown separately. The curve with negative 500mb ω (ascent) tends to be brighter because frontal clouds tend to be associated with mid-tropospheric ascents. As the TOMS measurements were made near local noontime, while the NCEP reanalysis is available on 4 fixed universal times (UT) per day, we have used the NCEP data at the most nearby time in constructing Figure 5.13. The NCEP data have also been interpolated on to the TOMS grid. Despite potential mismatch in temporal and spatial sampling, a general increase in the local noon reflectance with the static stability is evident. The existence of this relation is to a large extent due to the prevalent boundary layer clouds over the summertime N. Pacific. During other seasons, *e.g.*, DJF, the day-to-day reflectance variation is more strongly dominated by frontal clouds. This results in a strong relation between reflectance and 500 mb ω , but only a weak relation between reflectance and static stability (not shown). Interestingly, the JJA reflectance-stability curve starts to level off as the static stability becomes larger than 20 K. Note that the climatological mean static stability over the summertime west N. Pacific is above 20 K [*Klein and Hartmann, 1993*]. The lack of interannual correlation between reflectance and

⁶ This part of analysis was carried out in collaboration with X. Huang at Caltech.

static stability over the western N. Pacific is, therefore, consistent with the day-to-day relation between the two. What may have caused the reflectance to become independent of the stability when the latter is sufficiently large? One possible reason is that the reflectance of boundary layer clouds simply does not become much higher than 45RU, due to their limited vertical extent. This is supported by visual examination of the TOMS daily images and the GEOS visible images: only the frontal clouds appear to have reflectance of above 60-70RU. When the static stability is sufficiently high ($> 20\text{K}$), as over the JJA western N. Pacific, boundary clouds are almost always present, as seen in surface ship observations. The strong static stability, on the other hand, also keeps these clouds shallow, therefore limiting their brightness. The combined effect is to reduce the dependence of reflectance on the lower tropospheric static stability.

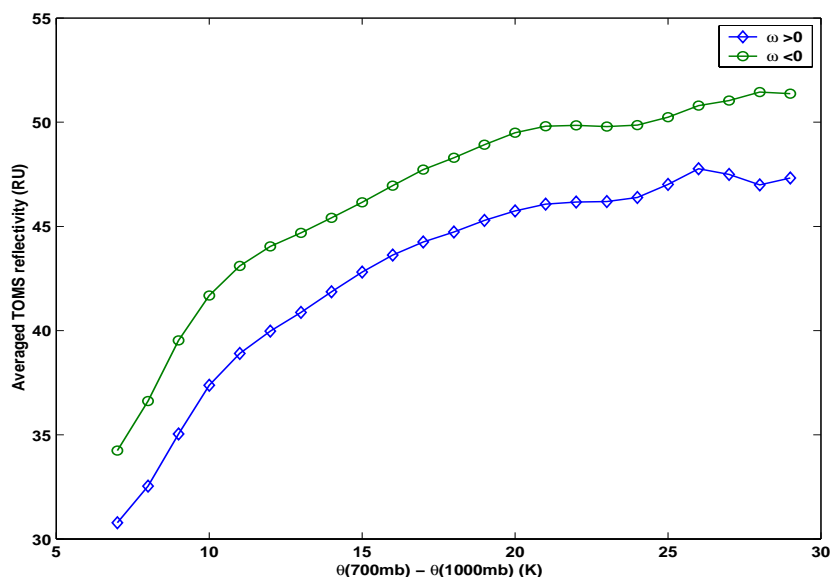


Figure 5.13 The averaged TOMS reflectance for stability bins over the JJA N. Pacific (160°E - 140°W , 45°N - 60°N). Within each bin, there are at least 1000 measurements.

5.8 Concluding Remarks

In this work, we have examined large-scale patterns in the interannual reflectance variations over the North Pacific and the North Atlantic. Interannual reflectance variations are found as an integral part of the midlatitude climate variations. The leading mode of the reflectance variation over the N. Atlantic is related to a meridional shift in the storm track in both winter and summer, and a corresponding NAO-like circulation pattern. A similar shift in the storm track exists in the non-summer seasons over the N. Pacific, and is related to the PNA pattern. The shift in the storm track is reflected in the occurrence frequency of the highly reflective frontal clouds. Variations in total reflectance, however, have a substantial component that can be linked to PNA related variations in the lower tropospheric stability, through the effect of stability on the boundary layer clouds. The leading pattern in the reflectance variations over the JJA western N. Pacific is associated with variations in the storm track intensity, while the pattern in the eastern N. Pacific is related to a varying subtropical high.

The interannual relationship between midlatitude reflectance and lower tropospheric stability is found to be more complex than the original proposal [*Klein and Hartmann, 1993*]. Our results over the N. Pacific during the non-summer seasons support the influence of stability variations on the reflectance over the midlatitude oceans through their effects on the boundary layer clouds. However, examination over the JJA western N. Pacific reveals that the effect of static stability on the reflectance may vanish when the stability is sufficiently large. This behavior is expected to limit the efficiency of the

proposed summertime stability-boundary layer cloud feedback [*Klein and Hartmann, 1993*]. Moreover, reflectance variations over the N. Atlantic and JJA western N. Pacific are more closely related to variations in the frontal clouds along the storm track instead of the boundary layer clouds. This suggests that previous analyses based on surface observations may have overemphasized the importance of the low clouds.

The relations between summertime reflectance and SST anomalies are largely local, and the patterns resemble those from earlier studies using MSC amount and SST [*Norris et al., 1998*]. However, the reflectance variations can be largely attributed to variations in the occurrence of highly reflective frontal clouds, instead of variations in the MSC amount. We suggest that the relations between reflectance, MSC, frontal clouds and SST may owe their existence to the effect of synoptic activities on all these quantities. The negative local correspondence between SST anomalies and reflectance/MSA anomalies, therefore, should not be taken as evidence for a cloud-SST feedback.

The results obtained from this analysis differ from those based on seasonal, spatial, and daily variations in some important ways [*Weaver and Ramanathan, 1997*]. For instance, based on spatial variations, reflectance was found independent of the static stability in January N. Pacific, and strongly dependent of the stability in July [*Weaver and Ramanathan, 1997*], exactly the opposite of the findings in this study. This highlights the importance of direct investigations of interannual variations; results obtained from seasonal, spatial and daily variations, while valuable, may not hold for the interannual variations.

Several previous studies related cloud properties to cloud temperature or the SST, in attempts to understand the response of clouds, and its feedback to climate change [Tselioudis *et al.*, 1993; Weare, 1994]. The findings in this study, however, suggest a more dynamically oriented view, other than a purely thermodynamic one. We argue that the question of cloud feedback maybe better answered in terms of how the large scale circulation would initially respond to a climatic forcing, and how clouds would respond to and reinforce these changes in the circulation. This work represents an effort in this direction. Finally, the TOMS record used here is still relatively short for interannual studies. A longer record would certainly enhance the statistical significance of the results. Unfortunately, such a record is yet to be made available.

5.9 Acknowledgements

We thank J. Norris for useful discussions and D. Noone and T. Schneider for helpful comments. The analysis presented in Figure 5.13 was carried out in collaboration with X. Huang.

5.10 References

- Alekseev, V., V. Dymnikov, V. Galin, E.M. Volodin, H.W. Barker, R.D. Cess, M.H. Zhang, E. CohenSolal, H. LeTreut, R.A. Colman, J.R. Fraser, B.J. McAvaney, D.A. Dazlich, L.D. Fowler, D.A. Randall, A.D. DelGenio, K.K.W. Lo, M.R. Dix, M. Esch, E. Roeckner, W.L. Gates, G.L. Potter, K.E. Taylor, J.J. Hack, W.J. Ingram, J.T. Kiehl, J.F. Royer, B. Timbal, V.P. Meleshko, P.V. Sporyshev, J.J. Morcrette, M.E. Schlesinger, W. Wang, and R.T. Wetherald, Cloud feedback in atmospheric general circulation models: An update, *Journal of Geophysical Research-Atmospheres*, 101 (D8), 12791-12794, 1996.
- Bjerknes, J. and H. Solberg, Life cycle of cyclone and the polar frontal theory of atmospheric circulation, *Geofys. Publ.*, 3, No. 1, 1-18, 1922.
- Bretherton, C.S., C. Smith, and J.M. Wallace, An intercomparison of methods for finding coupled patterns in climate data, *Journal of Climate*, 5 (6), 541-560, 1992.
- Carlson, T.N., Air-flow through mid-latitude cyclones and the comma cloud pattern, *Monthly Weather Review*, 108 (10), 1498-1509, 1980.
- Cess, R.D., G.L. Potter, J.P. Blanchet, G.J. Boer, S.J. Ghan, J.T. Kiehl, H. Letreut, Z.X. Li, X.Z. Liang, J.F.B. Mitchell, J.J. Morcrette, D.A. Randall, M.R. Riches, E. Roeckner, U. Schlese, A. Slingo, K.E. Taylor, W.M. Washington, R.T. Wetherald, and I. Yagai, Interpretation of cloud-climate feedback as produced by 14 atmospheric general-circulation models, *Science*, 245 (4917), 513-516, 1989.
- Chang, E.K.M., S.Y. Lee, and K.L. Swanson, Storm track dynamics, *Journal of Climate*, 15 (16), 2163-2183, 2002.
- Frankignoul, C., Sea-surface temperature anomalies, planetary-waves, and air-sea feedback in the middle latitudes, *Reviews of Geophysics*, 23 (4), 357-390, 1985.

-
- Fu, R., W.T. Liu, and R.E. Dickinson, Response of tropical clouds to the interannual variation of sea surface temperature, *Journal of Climate*, 9 (3), 616-634, 1996.
- Hanson, H.P., Marine stratocumulus climatologies, *International Journal of Climatology*, 11 (2), 147-164, 1991.
- Hartmann, D.L., M.E. Ockertbell, and M.L. Michelsen, The effect of cloud type on Earth's energy balance-global Analysis, *Journal of Climate*, 5 (11), 1281-1304, 1992.
- Houze, R.A., *Cloud dynamics*, xxix, 573 pp., Academic Press, San Diego, 1993.
- Kalnay, E., M. Kanamitsu, R. Kistler, W. Collins, D. Deaven, L. Gandin, M. Iredell, S. Saha, G. White, J. Woollen, Y. Zhu, M. Chelliah, W. Ebisuzaki, W. Higgins, J. Janowiak, K.C. Mo, C. Ropelewski, J. Wang, A. Leetmaa, R. Reynolds, R. Jenne, and D. Joseph, The NCEP/NCAR 40-year reanalysis project, *Bulletin of the American Meteorological Society*, 77 (3), 437-471, 1996.
- Klein, S.A., and D.L. Hartmann, The seasonal cycle of low stratiform clouds, *Journal of Climate*, 6 (8), 1587-1606, 1993.
- Klein, S.A., D.L. Hartmann, and J.R. Norris, On the relationships among low-cloud structure, sea-surface temperature, and atmospheric circulation in the summertime Northeast Pacific, *Journal of Climate*, 8 (5), 1140-1155, 1995.
- Kushnir, Y., W.A. Robinson, I. Blade, N.M.J. Hall, S. Peng, and R. Sutton, Atmospheric GCM response to extratropical SST anomalies: Synthesis and evaluation, *Journal of Climate*, 15 (16), 2233-2256, 2002.
- Lau, N.C., Variability of the Observed Midlatitude Storm tracks in relation to low-frequency changes in the circulation pattern, *Journal of the Atmospheric Sciences*, 45 (19), 2718-2743, 1988.

-
- Miller, R.L., Tropical thermostats and low cloud cover, *Journal of Climate*, 10 (3), 409-440, 1997.
- Nakamura, H., Midwinter suppression of baroclinic wave activity in the Pacific, *Journal of the Atmospheric Sciences*, 49 (17), 1629-1642, 1992.
- Norris, J.R., Low cloud type over the ocean from surface observations. Part I: Relationship to surface meteorology and the vertical distribution of temperature and moisture, *Journal of Climate*, 11 (3), 369-382, 1998a.
- Norris, J.R., Low cloud type over the ocean from surface observations. Part II: Geographical and seasonal variations, *Journal of Climate*, 11 (3), 383-403, 1998b.
- Norris, J.R., Interannual and interdecadal variability in the storm track, cloudiness, and sea surface temperature over the summertime North Pacific, *Journal of Climate*, 13 (2), 422-430, 2000.
- Norris, J.R., and C.B. Leovy, Interannual variability in stratiform cloudiness and sea-surface temperature, *Journal of Climate*, 7 (12), 1915-1925, 1994.
- Norris, J.R., Y. Zhang, and J.M. Wallace, Role of low clouds in summertime atmosphere-ocean interactions over the North Pacific, *Journal of Climate*, 11 (10), 2482-2490, 1998.
- North, G.R., T.L. Bell, R.F. Cahalan, and F.J. Moeng, Sampling Errors in the Estimation of Empirical Orthogonal Functions, *Monthly Weather Review*, 110 (7), 699-706, 1982.
- Oreopoulos, L., and R. Davies, Statistical dependence of albedo and cloud cover on sea-surface temperature for 2 tropical marine stratocumulus regions, *Journal of Climate*, 6 (12), 2434-2447, 1993.

-
- Philander, S.G.H., D. Gu, D. Halpern, G. Lambert, N.C. Lau, T. Li, and R.C. Pacanowski, Why the ITCZ is mostly north of the equator, *Journal of Climate*, 9 (12), 2958-2972, 1996.
- Preisendorfer, R.W., and C.D. Mobley, *Principal component analysis in meteorology and oceanography*, xviii, 425 pp., Elsevier, New York, NY, 1988.
- Reed, R. J. Advances in Knowledge and Understanding of Extratropical Cyclones During the Past Quarter Century: An Overview, in *Extratropical Cyclones: The Erik Palmén Memorial Volume*, Edited by C. Newton and E. O. Holopainen, American Meteorological Society, Boston, 1990.
- Rossow, W.B., and R.A. Schiffer, ISCCP Cloud Data Products, *Bulletin of the American Meteorological Society*, 72 (1), 2-20, 1991.
- Trenberth, K.E., Storm tracks in the Southern Hemisphere, *Journal of the Atmospheric Sciences*, 48 (19), 2159-2178, 1991.
- Trenberth, K.E., G.W. Branstator, D. Karoly, A. Kumar, N.C. Lau, and C. Ropelewski, Progress during TOGA in understanding and modeling global teleconnections associated with tropical sea surface temperatures, *Journal of Geophysical Research-Oceans*, 103 (C7), 14291-14324, 1998.
- Tselioudis, G., A.A. Lacis, D. Rind, and W.B. Rossow, Potential Effects of Cloud Optical-Thickness on Climate Warming, *Nature*, 366 (6456), 670-672, 1993.
- Wallace, J.M., and D.S. Gutzler, Teleconnections in the Geopotential Height Field During the Northern Hemisphere Winter, *Monthly Weather Review*, 109 (4), 784-812, 1981.
- Weare, B.C., Interrelationships between Cloud Properties and Sea-Surface Temperatures on Seasonal and Interannual Time Scales, *Journal of Climate*, 7 (2), 248-260, 1994.

- Weaver, C.P., The interactions among cyclone dynamics, vertical thermodynamic structure, and cloud radiative forcing in the North Atlantic summertime storm track, *Journal of Climate*, 12 (8), 2625-2642, 1999.
- Weaver, C.P., and V. Ramanathan, The link between summertime cloud radiative forcing and extratropical cyclones in the North Pacific, *Journal of Climate*, 9 (9), 2093-2109, 1996.
- Weaver, C.P., and V. Ramanathan, Relationships between large-scale vertical velocity, static stability, and cloud radiative forcing over northern hemisphere extratropical oceans, *Journal of Climate*, 10 (11), 2871-2887, 1997.
- Zhang, Y., J.R. Norris, and J.M. Wallace, Seasonality of large-scale atmosphere-ocean interaction over the North Pacific, *Journal of Climate*, 11 (10), 2473-2481, 1998.

VITA

Zhiming Kuang was born on April 18, 1975 in Jiangxi, China. He received his B.S. in Space Physics from Peking University at Beijing in 1996.